Gas Transport and Control in Thick-Liquid Inertial Fusion Power Plants

by

Christophe Sylvain Debonnel

M.S. (University of California at Berkeley) 2001

A dissertation submitted in partial satisfaction of the
requirements for the degree of
Doctor of Philosophy

in

Engineering—Nuclear Engineering

in the

GRADUATE DIVISION
of the
UNIVERSITY OF CALIFORNIA, BERKELEY

Committee in charge:
Professor Per F. Peterson, Co-Chair
Doctor Simon S. Yu, Co-Chair
Professor Jasmina Vujic
Professor Philip S. Marcus

Spring 2006

The dissertation of Christophe Sylvain Debonnel is approved:

Co-Chair Date

Co-Chair Date

Date

Date

University of California, Berkeley

Spring 2006

Gas Transport and Control in Thick-Liquid Inertial Fusion Power Plants

Copyright 2006

by

Christophe Sylvain Debonnel

Abstract

Gas Transport and Control in Thick-Liquid Inertial Fusion Power Plants

by

Christophe Sylvain Debonnel

Doctor of Philosophy in Engineering—Nuclear Engineering

University of California, Berkeley

Professor Per F. Peterson and Doctor Simon S. Yu, Co-Chairs

Among the numerous potential routes to a commercial fusion power plant, the inertial path with thick-liquid protection is explored in this doctoral dissertation. Gas dynamics phenomena in such fusion target chambers have been investigated since the early 1990s with the help of a series of simulation codes known as TSUNAMI. For this doctoral work, the code was redesigned and rewritten entirely to enable the use of modern programming techniques, languages and software; improve its user-friendliness; and refine its ability to model thick-liquid protected chambers. The new ablation and gas dynamics code is named “Visual Tsunami” to emphasize its graphics-based pre- and post-processors. It is aimed at providing a versatile and user-friendly design tool for complex systems for which transient gas dynamics phenomena play a key role. Simultaneously, some of these improvements were implemented in a previous version of the code; the resulting code constitutes the version 2.8 of the TSUNAMI series. Visual Tsunami was used to design and model the novel Condensation Debris Experiment (CDE), which presents many aspects of a typical Inertial Fusion Energy (IFE) system and has therefore been used to exercise the code. Numerical and experimental results are in good

agreement.

In a heavy-ion IFE target chamber, proper beam and target propagation set stringent requirements for the control of ablation debris transport in the target chamber and beam tubes. When the neutralized ballistic transport mode is employed, the background gas density should be adequately low and the beam tube metallic surfaces upstream of the neutralizing region should be free of contaminants. TSUNAMI 2.8 was used for the first simulation of gas transport through the complex geometry of the liquid blanket of a hybrid target chamber and beam lines. Concurrently, the feasibility of controlling the gas density was addressed with a novel beam tube design, which introduces magnetic shutters and a long low-temperature liquid vortex; this beam tube configuration was included in the first thick-liquid heavy-ion fusion point design, the so-called Robust Point Design 2002. Additionally, novel, alternative thick-liquid chambers that can accommodate the assisted-pinch, the solenoidal final-focusing, or a Z-pinch driver are discussed.

Prof. P.F. Peterson
Dissertation Committee Co-Chair

Dr. S.S. Yu
Dissertation Committee Co-Chair

To Audrey and Melody

Contents

List of Figures **vi**

List of Tables **viii**

1 Thick-Liquid Protection and Inertial Fusion Power Plants **1**
1.1 Introduction to Fusion Power 1
1.1.1 Fusion Basics 1
1.1.2 Possible Routes to Fusion Power 2
1.1.3 Inertial Confinement Fusion 3
1.2 Inertial Fusion Energy 5
1.2.1 Target Chamber Design 5
1.2.2 Thick-Liquid Protection 6
1.3 Goals and Scope of Dissertation 7
1.3.1 Simulation Code Development 7
1.3.2 Design and Modeling of the Condensation Debris Experiment 9
1.3.3 Gas Transport and Control in Thick-Liquid Target Chambers 9

I Visual Tsunami Numerical Models **11**

2 The Code "Visual Tsunami" **12**
2.1 Introduction to Visual Tsunami 12
2.2 Code History and Use 13
2.3 Pre- and Post-Processors 16
2.3.1 Input File Builder 16
2.3.2 Output File Processor 18
2.4 Physical and Numerical Models 18
2.5 Conclusion 20

3 Compressible Gas Dynamics **21**
3.1 Introduction to Eulerian Gas Dynamics 21
3.1.1 The Euler Equations in Conservative Eulerian Form 22
3.1.2 A Flavor of the Method of Characteristics 24
3.1.3 The Euler Equations in Characteristic Eulerian Form 27
3.2 Gas Dynamics Equations of State 30

3.2.1 Definitions and Relations 30
3.2.2 Ideal Gas Equations of State 32
3.2.3 Real Gas Equations of State 32
3.3 The Exact Riemann Problem: Exact Ideal Gas Case 33
3.3.1 Introduction and Physical Assumptions 33
3.3.2 Mathematical Considerations: Simple and Shock Waves 34
3.3.3 Implicit Analytical Solution to the Ideal Gas Riemann Problem . . . 42
3.3.4 Numerical Model and Choice of Root Solver 45
3.4 The Exact Riemann Problem: Exact Real Gas Case 48
3.4.1 Mathematical Tools: Simple and Shock Waves 48
3.4.2 New and State-Of-The-Art Analytical and Numerical Models 50
3.5 Exotic Riemann Cases 53
3.5.1 Uniform Initial Conditions 53
3.5.2 Left Vacuum 53
3.5.3 Right Vacuum 54
3.5.4 Center Vacuum 54
3.6 Reconstruction-Evolution Methods 56
3.6.1 First-Order Reconstruction: Piecewise Constant Interpolation 57
3.6.2 Evolution in the Case of a Piecewise Constant Reconstruction 58
3.6.3 Axially-Symmetric Cylindrical Coordinates 59
3.6.4 Boundary Conditions 61
3.7 Benchmarking 62
3.7.1 Riemann Solvers 62
3.7.2 Evolution-Reconstruction Schemes 63
3.8 Conclusions and Perspectives 67

4 Radiation Modeling 69
4.1 Introduction to Radiation Modeling 69
4.2 Physical Modeling: Flux-Limited Diffusion 71
4.2.1 Differential Equations 71
4.2.2 Initial and Boundary Conditions 74
4.3 Numerical Model 74
4.3.1 Three-Dimensional Cartesian Coordinates 74
4.3.2 Axially-Symmetric Cylindrical Coordinates 76
4.4 Conclusions and Perspectives 77

5 Gas-Liquid Interface 78
5.1 Introduction 78
5.2 Submillisecond Heat Transfer in Liquid Jets 79
5.2.1 Physical and Mathematical Models 79
5.2.2 Numerical Model 81
5.3 Benchmarking 82
5.4 A Novel Gas-Liquid Interface Model 83
5.4.1 Interface Mass Transfer 84
5.4.2 Interface Momentum Transfer 86
5.4.3 Interface Heat Transfer 88

5.4.4 Choking Considerations . . . 89
5.5 Conclusions and Perspectives . . . 90

6 Target and Ablation Modeling 91
6.1 Introduction . . . 91
6.2 Target Modeling . . . 92
6.2.1 Neutrons . . . 92
6.2.2 Target and Hohlraum Remnants . . . 93
6.2.3 X-Rays . . . 93
6.3 Initial Ablation Modeling . . . 94
6.3.1 Energy Deposition: An Improved TSUNAMI Model . . . 94
6.3.2 Numerical Model . . . 97
6.3.3 Energy Profiles and Ablation Depths: A Review . . . 98
6.3.4 Discussion . . . 102
6.4 Conclusions and Perspectives . . . 103

II Applications 105

7 The Condensation Debris Experiments 106
7.1 Overview of the Condensation Debris Experiments . . . 106
7.2 Dimensioning of the Condensation Chamber . . . 108
7.3 Visual Tsunami Simulations of CDE . . . 110
7.4 Experimental and Numerical Results . . . 111
7.5 Conclusions and Perspectives . . . 112

8 Gas Venting in Thick-Liquid Protected Fusion Chambers 114
8.1 Introduction . . . 114
8.2 Neutralized Ballistic Final-Focusing . . . 115
8.2.1 Gas Density Control . . . 115
8.2.2 TSUNAMI Ablation and Venting Simulations . . . 118
8.2.3 Possible Optimization . . . 125
8.3 Assisted-Pinch Final-Focusing . . . 126
8.3.1 A variant of the RPD Chamber with Assisted-Pinch Focusing . . . 126
8.3.2 TSUNAMI Ablation and Venting Simulations . . . 127
8.4 Solenoidal Final-Focusing . . . 129
8.4.1 A Novel “Vortex Chamber” for Solenoidal Focusing . . . 129
8.4.2 Vortex Response to Target Output . . . 131
8.5 Z-Pinch Inertial Fusion Energy . . . 132
8.5.1 Z-Pinch Target Chamber . . . 132
8.5.2 Visual Tsunami Ablation and Venting Modeling . . . 132
8.5.3 On-Going Optimization . . . 137
8.6 Conclusions and Perspectives . . . 139

9 Conclusion **140**
9.1 Simulation Code Development 140
9.2 Design and Modeling of the Condensation Debris Experiments 141
9.3 Gas Transport and Control in Thick-Liquid Inertial Fusion Target Chambers . 142

Bibliography **145**

A Flibe Properties **157**
A.1 Miscellaneous Properties 157
A.2 Hydrodynamics Equations of State 158
A.2.1 Chen's Equations of State 158
A.2.2 Jantzen's Equations of State 160
A.2.3 Zaghloul's Equations of State 160
A.2.4 The Chen-Zaghloul Equations of State 164
A.3 Opacities 164
A.3.1 Cold Opacities 164
A.3.2 Hot Opacities 164

List of Figures

2.1 Architecture of Visual Tsunami 2.0: pre-processor tools (left), MATLAB core (center), and MATLAB post-processor. The implementation of radiation and aerosol transport models is left for future work. 15
2.2 The AutoLISP GUI used to define material properties. 17

3.1 One-dimensional test case 1: density, velocity, pressure, specific energy. . . . 64
3.2 One-dimensional test case 2: density, velocity, pressure, specific energy. . . . 64
3.3 One-dimensional test case 3: density, velocity, pressure, specific energy. . . . 65
3.4 One-dimensional test case 4: density, velocity, pressure, specific energy. . . . 65
3.5 One-dimensional test case 5: density, velocity, pressure, specific energy. . . . 66
3.6 Two-dimensional test case 5: density. 67
3.7 Three-dimensional test case 1: density. 68

6.1 Comparison of energy deposition models for a typical Z-IFE case. 103
6.2 Comparison of temperature profiles. 104

7.1 Schematic of the Condensation Debris Experiment. 107
7.2 Visual Tsunami density contour plots. The density of the solid structures is arbitrarily low. 111
7.3 Visual Tsunami 2.0 time-integrated contour plot and CCD image. 112

8.1 Scaled cross-section of the RPD chamber and beam-lines [26, 27]. Lengths are in mm. 115
8.2 TSUNAMI density contour plots at various times. The density of the liquid and solid structures is arbitrarily low. 120
8.3 Peak gas pressure onto the liquid pocket in the RPD chamber. 121
8.4 Impulse load to the liquid pocket in the RPD chamber. 121
8.5 Density at the entrance of the RPD centerline tube. 122
8.6 Integrated mass flux at the entrance of the RPD centerline tube. 123
8.7 Density at the entrance of the magnetic shutters in the RPD centerline tube. . 123
8.8 Integrated mass flux at the entrance of the magnetic shutters in the RPD centerline tube. 124
8.9 Geometry of the assisted-pinch chamber. 127
8.10 TSUNAMI simulations of the assisted-pinch chamber. The density of the liquid and solid structures is arbitrarily low. 128

8.11 Impulse load to the liquid pocket in the assisted-pinch chamber. 128
8.12 Schematic of the vortex chamber [28]. The first wall is not depicted. 130
8.13 A combination of liquid blowing and sucking generates the vortex flow. The centrifugal force maintains the flow attached to the wall [28]. 130
8.14 Two-dimensional cutaway view of LLNL's 2004 "closed" configuration. . . . 133
8.15 Visual Tsunami geometrical model of LLNL's 2004 "closed" configuration. . 134
8.16 Density contour plots for the "closed" case. 134
8.17 Pressure contour plots for the "closed" case. 135
8.18 Two-dimensional cutaway view of LLNL's 2004 "open" configuration. 135
8.19 Visual Tsunami geometrical model of LLNL's 2004 "open" configuration. . . 136
8.20 Density contour plots for the "open" case. 136
8.21 Pressure contour plots for the "open" case. 137
8.22 Impulse load to the liquid curtain in the "closed" and "open" Z-IFE chambers. 138
8.23 Two-dimensional cutaway view of LLNL's 2005 configuration (courtesy of R.P. Abbott, LLNL). 138

A.1 Flibe pressure as a function of density and specific energy. 161
A.2 Flibe pressure as a function of density and temperature. 161
A.3 Flibe sound speed as a function of density and temperature. 162
A.4 Flibe adiabatic exponent as a function of density and temperature. 162
A.5 Flibe specific heat at constant pressure as a function of density and temperature. 163
A.6 Flibe ionization state as a function of density and temperature. 163

List of Tables

2.1 TSUNAMI code history. 13

3.1 A few of the Riemann problems used as test cases. 62

4.1 Radiation cells. 76

A.1 Various flibe properties. 158

Acknowledgments

This doctoral work draws on the experience and enthusiasm of my research advisors, Per F. Peterson and Simon S. Yu. I am grateful for their assistance and support. TSUNAMI 2.8 was born out of TSUNAMI 2.6, which was mainly developed by John Scott, a former doctoral student in the Thermal-Hydraulics Laboratory at the University of California at Berkeley. His influence, along with those of other doctoral students who developed the previous versions of TSUNAMI, can be felt in most aspects of TSUNAMI 2.8 and many features of Visual Tsunami, and are happily acknowledged. The work on the Condensation Debris Experiment was made possible through a fruitful and enjoyable collaboration with Mike Tobin, Theodore Vidnovic and Victor Karpenko from the Lawrence Livermore National Laboratory (LLNL).

Three undergraduates studying at the University of California at Berkeley (UCB)—Mio Suzuki, Trudie Wang, and Edith Garcia—chose to sacrifice their already scarce free time to work on various research projects related to the implementation of always evolving algorithms. The scope of their work, often particularly ambitious for undergraduates, helped shape and develop Visual Tsunami and I am deeply indebted to Mio, Edith, and, last but not least, Trudie, who contributed significantly to the coding and development of Visual Tsunami's graphical user interfaces. Two former students of mine, Lev Trubov and Ariel Zeballos, contributed to the implementation of the MATLAB core of Visual Tsunami.

Conversations with Philippe Bardet, Laura Chao, Jakob Christensen, Grant Fukuda, Steven Pemberton, and my other office mates from the UCB nuclear engineering thermal hydraulics laboratory influenced this work to an extent they may not suspect. This endeavor did benefit from feedback received from peers from the multi-institutional ARIES-IFE design team as well as from my colleagues with the heavy-ion fusion group at the Lawrence Berkeley Na-

tional Laboratory. I am also particularly thankful for comments and encouragements provided by Melody Aronson, Phil Marcus, and Jasmina Vujic.

Friends and family members, too numerous to be named here, were in charge of keeping me sane while I was debugging the version of the TSUNAMI code I inherited. I am thankful for their friendships and encouragements. I hope they succeeded.

This work was partially funded by the US Department of Energy under contracts DE-AC03-76SF00098, W-7405-ENG-48, DE-AC02-05CH11231, and DE-FG03-97ER5441.

Chapter 1

Thick-Liquid Protection and Inertial Fusion Power Plants

1.1 Introduction to Fusion Power

1.1.1 Fusion Basics

Fusion bears the promise of a clean and sustainable source of energy. The fusion reaction that is envisaged for the first generation of fusion power plants is:

$$\mathrm{D} + \mathrm{T} \rightarrow \alpha + \mathrm{n} + 17.6\ \mathrm{MeV} \tag{1.1}$$

where a deuteron (D or $^{2}H^{+}$) and a triton (T or $^{3}H^{+}$) fuse to create a helium nucleus (α or He^{2+}) and a neutron (n), while releasing 2.82×10^{-12} J or 17.6 MeV. The above D-T reaction is preferred to other fusion reactions because it has the highest probability (or cross-section) in the range of temperatures that allow fusion reactions to take place and that can be most easily obtained in a human-made device. In particular, the D-T reaction is preferred to p-B and other

neutron-free reactions, even if the high-energy neutrons produced by the D-T reaction are a potential threat to the chamber solid structures.

Deuterium can be found in water, but tritium is a short-lived radioactive isotope of hydrogen and has to be produced, usually from lithium, through one of the two following (n,α) reactions:

$$^{6}\text{Li} + \text{n (thermal)} \rightarrow \alpha + \text{T} + 4.78 \text{ MeV} \tag{1.2a}$$

$$^{7}\text{Li} + \text{n (fast)} \rightarrow \alpha + \text{T} + \text{n} - 2.47 \text{ MeV} \tag{1.2b}$$

A 1-GWe fusion power plant will consume around 0.6 kg of D-T fuel a day, to be compared with the typical 3.3 kg needed per day in a fission plant of the same power and the 7,300,000 kg of fuel consumed a day in a coal-fired power plant. Fossil fuel power plants release nitrogen, sulfur, and carbon oxides. Current nuclear plants generates short- and long-lived fission and activation products, with almost no release to the atmosphere. D-T reactions do not produce any long-lived elements and future fusion power plants will have essentially no long-lived by-products if adequate liquid protection is provided to prevent any significant activation of a low- to medium-Z vessel.

1.1.2 Possible Routes to Fusion Power

The Coulomb force repels protons apart from each other. To fuse, nuclei therefore need to achieve kinetic energies high enough to overcome this Coulomb barrier. This can be done using accelerators to impart high kinetic energy to fuel ions. For instance, in the Rotating Target Neutron Source (RTNS) at the University of California at Berkeley, deuterons are accelerated by a potential difference of 500,000 V to reach 4% of the speed of light and hit a tritiated target. Fusion does occur, but this approach consumes far more driving power than the fusion

reactions release. Similarly, net fusion power would not be produced with two colliding beams of fuel, because of the inherently low density of the beams.

Instead of accelerating ions in an organized manner, ions can be heated up, gaining random kinetic energy, as is done in the sun. Fusion is indeed the source of energy of the stars, in which the high pressure required for fusion to happen is counterbalanced by the gravitational force. The total quantity of fuel is so extraordinarily large and the average time the fuel spent confined by gravitation is so extraordinarily long that substantial fusion energy is generated, even though the chain of reactions that cause four protons to fuse ultimately into one alpha particle

$$4\,\mathrm{p} + 2\,\mathrm{e}^{-} \rightarrow \alpha + 2\,\nu \tag{1.3}$$

has a very low cross-section. An earth-bound engineering device based on gravitational confinement is out-of-reach, for obvious reasons. A human-made device has to deal with smaller masses and much shorter confinement times, necessitated by relatively larger heat losses.

Magnetic confinement fusion aims at containing high-temperature, low-density plasmas using strong electromagnetic fields to keep the fuel together and prevent it from cooling through contact with the plasma vessel. Plasma instabilities and heat losses provide the main challenges to overcome for net fusion power generation. Inertial Confinement Fusion (ICF) relies upon the ability to compress a D-T pellet using energy provided by a laser, a Z-pinch or an ion accelerator [4, 37].

1.1.3 Inertial Confinement Fusion

Inertial fusion targets can be driven directly or indirectly. In direct-drive, laser beams strike a D-T pellet, heating the outer layer that sublimates and expands outwards. As a reaction,

the inner fuel layer is driven inwards. The fuel is then compressed to high temperature and density—about a thousand times liquid density. A “hot spot” appears, where fusion takes place. The neutrons stream away, but the alpha particles are stopped in the layer of fuel next to the hot spot; this layer is heated up by the alphas and start to fuse, generating alpha particles that will stop in the next layer. Hence, a “fusion burn wave” propagates from the initial hot spot towards the outside surface of the pellet. “Inertial confinement” fusion is actually somewhat of a misnomer. The scheme relies on the inertia of the target to maintain the integrity of the fusing pellet for a significant fraction of the fuel to undergo fusion. In practice, there is hardly any confinement at all; the target disassembles within a few picoseconds—nonetheless enough time for a third of the fuel of a properly designed target to fuse.

In indirect drive, the pellet is held in a small container, which is usually called a hohlraum, after the German name for a cavity. The laser or heavy ion beams stop and deposit the driving energy onto the inside surface of the hohlraum, heating the walls to a few million kelvins. The walls emit x-rays, which are mainly absorbed in the outer layer of the D-T pellet. The outer layer is ablated and expands outwards. The remaining phenomena are similar to those in the direct-drive case. Descriptions of heavy-ion hohlraums can be found in References [69, 9, 10].

Direct-drive can, in principle, achieve higher energy conversion (from driver to implosion) than indirect-drive but the imploding capsule is subject to instabilities due to the lack of uniformities of the irradiation induced by a finite number of discrete laser beams. A better, more symmetric irradiation and implosion are expected via the indirect drive approach. Two laser facilities currently under construction—Laser Mega-Joule in the suburb of Bordeaux, France, and National Ignition Facility at the Lawrence Livermore National Laboratory—are designed to achieve breakeven and ignition. An inertial fusion power plant would be pulsed: D-T targets

would be repetitively ignited at a frequency high enough to release enough energy to produce significant power.

1.2 Inertial Fusion Energy

1.2.1 Target Chamber Design

Designing a fusion power plant demands facing several multi-decade scientific and engineering challenges. The scientific challenges require identifying and understanding the phenomena that will control the capability to ignite targets. The engineering challenges call for developing innovative methods and tools to build compact and inexpensive power plants that can achieve high repetition rates, while maintaining safety and reliability. The target chamber needs to extract the fusion energy for electricity production; breed enough tritium to be self sufficient; clear itself for the next shot to take place by restoring the chamber condition imposed by proper beam propagation or Z-pinch operation; and survive the hostile fusion environment, ideally for the full life of the plant.

The fusion energy is split between high-energy neutrons, x-rays, and debris. Simple kinematic considerations indicate that the D-T reaction gives 80% of the released energy to the neutron and the remaining 20% to the α particle. Detailed numerical simulations show that in direct-drive targets, the energy is indeed roughly split according to this simple estimate, with a small fraction of the yield given to highly energetic x-rays. Indirect-drive targets present a more complex energy partitioning. This comes from the interaction of the target debris with the hohlraum, which causes a significant fraction of the debris to slow down and convert part of its energy to x-rays. This is also true for neutrons, but to a lesser extent. Typically, for

indirect-drive targets, neutrons carry 68% of the yield, x-rays 25%, and target and hohlraum debris 7%.

Over the last thirty years or so, several target chamber concepts have been envisioned. Dry wall chambers rely on the standoff distance between the target and the metallic or ceramic first wall to attenuate the x-ray and neutron fluences. A buffer gas stops most debris and a significant fraction of the x-rays. A fireball is then formed and radiates its energy over time scales potentially long enough for the heat to be accommodated by the first wall through heat conduction. Thin liquid wall chambers interpose a liquid layer between the target and the structural first wall. The thin liquid layer is meant to shield the structural first wall from x-rays and ions. Thick liquid wall chambers, to be discussed at length in this study, make use of thick liquid jets and vortexes to protect the first wall.

1.2.2 Thick-Liquid Protection

Thick-liquid protection offers several advantages over those offered by thin-liquid walls. The liquid structures are “neutronically-thick” and will therefore protect the solid walls by absorbing and slowing down target neutrons, reducing the neutron fluence. An efficient thick-liquid protection scheme will reduce neutron energy to a fast fission-like spectrum: Materials developed for fission power plants can then be used, eliminating the need for a costly material development program. Ideally, the first structural walls would be fabricated from relatively inexpensive nuclear-grade material such as stainless steel and would last the typical lifetime of a reactor. The vessel activation would be very low, permitting disposal as low-level waste.

The liquid structures will play the role of the coolant fluid in a fission power plant, absorbing most of the fusion energy, which will then be easily extracted from the target chamber,

so that it can be used to produce electricity. The binary molten salt flibe (LiF-BeF_2) and the ternary mixture flinabe (LiF-NaF-BeF_2) are primary candidates. The choice of flibe or flinabe for the liquid pocket was motivated by the possibility of breeding tritium via the (n,α) reaction undergone by lithium and by the properties of beryllium, which compensates for the neutron absorption of the fluorine, so that tritium breeding ratios greater than one can still be achieved. These salts are good neutron multipliers and have good slowing-down properties, which favor the exothermic tritium breeding reaction over the endothermic one.

The liquid structures help restore chamber conditions required for either Z-pinch operation or proper target injection and heavy-ion beam propagation. In particular, in some heavy-ion fusion plants, jets can sweep the target chamber free of droplets that may otherwise prevent correct target and beam propagation. Thick-liquid protection would help reduce the size of the target chamber, maximizing power density. In the case of a neutralized ballistic heavy-ion fusion plant, the beams travel inside the target chamber without being refocused by magnets. Thick-liquid protection contributes to reducing this focusing distance.

1.3 Goals and Scope of Dissertation

1.3.1 Simulation Code Development

The exploding target emits x-rays that will deposit their energy in thin layers of the target-facing surfaces of the liquid structures, causing a rise in temperature that will oftenly cause parts of the layers to evaporate and then expand away from the liquid surfaces. This evaporation phenomenon is usually referred to as ablation. The ablated layers interact with the expanding target and ultimately vent through the liquid structures inside the target chamber.

The modeling of the gas dynamics inside a fusion chamber is complex and presents unique challenges [47, 58] that prompted in the early 1990s the development of an academic computer code tailored to simulate these phenomena. (Existing codes that might have been used as a starting point were not widely available.) A brief history of the code, TSUNAMI, is given in Chapter 2. TSUNAMI numerically solves the time-dependent, compressible Euler equation for ideal or real gas. Efforts have been focused on the ability to model shock waves in complex geometries. A comparison between several inertial fusion codes can be found in Ref. [58].

As described in Chapter 2, various versions of TSUNAMI are available, with different capabilities. A major—and somewhat quixotic—goal of this doctoral work is to provide a user-friendly, object-oriented "backbone" for TSUNAMI in order to stop, ultimately, the proliferation of TSUNAMI codes that has taken place since the early 1990s. (Typically, rewriting the code was quicker than modifying an existing version.) Chapter 2 outlines how the new modular architecture of the code developed over the course of this PhD can be used to add new capabilities. This modular nature is meant to be used to test new numerical schemes, as expected from an academic code. A somewhat related goal is the development of a set of benchmarking tools that can be used to compare various algorithms and validate the code.

Chapter 3 details the physical, mathematical and numerical gas dynamics models implemented in the code, named "Visual Tsunami." The choice of these models stems from the expected robustness of the algorithms; they are meant to provide the basic tools that can be used to implement higher-order and/or more approximate and faster schemes, and compare them to their robust first order counterparts. Emphasis has been put on developing an exact yet fast real gas Riemann solver. Radiation transport is touched upon in Chapter 4 where a multidimensional two-temperature flux-limited model is presented. Chapter 5 deals with a

novel gas/liquid interface. Chapter 6 provides a review of ablation models and an improved TSUNAMI model for the interaction of target x-rays with liquid structures.

1.3.2 Design and Modeling of the Condensation Debris Experiment

Concurrently to the development of Visual Tsunami, the code TSUNAMI, version 2.6 [12], was modified to ameliorate the code performance and incorporate a few of the improvements implemented in Visual Tsunami. The resulting code constitutes the version 2.8 of the TSUNAMI series and was employed to design and model a variety of heavy-ion fusion target chambers along with the Lawrence Livermore National Laboratory's novel Condensation Debris Experiment. TSUNAMI had not been exercised against an actual integral experiment in recent years. An important goal of this doctoral work was to employ TSUNAMI 2.8 and Visual Tsunami to help design and model the Condensation Debris Experiments. TSUNAMI 2.8 was more particularly used to help design the various experimental campaigns. Chapter 7 reports on the latest numerical modeling done with Visual Tsunami. As a first cut to the problem, a qualitative agreement with experimental results is sought after.

1.3.3 Gas Transport and Control in Thick-Liquid Target Chambers

In a heavy-ion inertial fusion chamber protected by an array of liquid jets, modeling the venting of the target and ablation debris through the venting paths of the thick-liquid pocket is of primary importance to determine the impulse load transmitted to the liquid and metallic structures and the amount of debris that escapes up the heavy-ion beam lines. Chapter 8 illustrates the state of the art in gas dynamics modeling in a thick-liquid chamber compatible with the main heavy-ion transport mode, the so-called neutralized ballistic scheme. Besides

the extension of the modeling capability of gas venting phenomena in IFE chambers, a goal of this doctoral work was to coordinate the design of a beam line that can accommodate the debris jetting out of the target chamber. The resulting design is presented in Chapter 8 together with the supporting simulations performed with TSUNAMI 2.8. Chapter 8 also presents two target chamber configurations compatible with alternate heavy ion beam propagation schemes and deals with the Z-IFE thick-liquid protected target chamber and its modeling with the Visual Tsunami code. Overall conclusions are drawn in Chapter 9.

Part I

Visual Tsunami Numerical Models

Chapter 2

The Code “Visual Tsunami”

2.1 Introduction to Visual Tsunami

“TSUNAMI” refers to a series of radiation hydrodynamics codes developed and maintained since the early 1990s at the University of California at Berkeley (UCB) in collaboration with the Lawrence Berkeley National Laboratory, Lawrence Livermore National Laboratory and the University of California at Los Angeles. The different versions of the code offered various capabilities and were employed to model a variety of inertial fusion energy (IFE) and inertial confinement fusion (ICF) systems; the history of the code is summarized in the second section of this chapter.

TSUNAMI stands for TranSient Upwind Numerical Analysis Method for Inertial confinement fusion; early versions of the code were in FORTRAN 77. “Visual Tsunami” 1.0 and 2.0, the latest versions of TSUNAMI, makes use of the conveniences offered by modern computing languages and software. Visual Tsunami 1.0 was first presented by Debonnel *et al.* in Ref. [25]. Visual Tsunami 2.0 is presented shortly in the third and fourth sections of this

chapter. Algorithms are presented in detail in Chapters 3 to 6.

The core of Visual Tsunami 1.0 was written in Fortran 95. FORTRAN used to stand for (mathematical) FORmula TRANslation. The names of its most recent versions, starting from Fortran 90, are not portmanteaux anymore; even if Fortran remains a language of choice for scientific computing, its name does not officially reflect it anymore through an acronym that would otherwise reduce the actual breadth of possibilities offered by a rich, modern language. Similarly, Tsunami should be read and written as a name, with only the first letter capitalized. The applicability of the code goes beyond the traditional ICF/IFE use of TSUNAMI. The adjective "Visual" stems from the input and output graphical user interfaces (GUIs) that have been developed recently and improved the user-friendliness of the code significantly.

2.2 Code History and Use

version	characteristics	references
TSUNAMI RG	1-D radiation gas dynamics real gas EOS (Chen's EOS for flibe)	Chen's thesis [11] and references therein
TSUNAMI 1.0	2-D gas dynamics ideal gas EOS	Liu's thesis [38] and references therein
TSUNAMI 2.6	2-D multi-species hydrodynamics real gas EOS (SESAME [42]) coupling to ABLATOR code [2]	Scott's thesis [63] and references therein
TSUNAMI 2.7	2-D gas dynamics radiation real gas EOS (Jantzen's EOS)	Jantzen's thesis [34] and references therein
TSUNAMI 2.8	user-friendly version of version 2.6 real gas EOS (Chen's EOS for flibe) FORTRAN 77/95 and MATLAB	
Visual Tsunami 1.0	new code in Fortran 95 and MATLAB	[25]
Visual Tsunami 2.0	new code in MATLAB	this doctoral dissertation

Table 2.1: TSUNAMI code history.

Table 2.1 presents an outline of the history of the TSUNAMI code. The first two versions of TSUNAMI were developed to model the gas dynamics inside the inertial fusion target chamber HYLIFE-II [45]. Chen [11, 18, 16] developed the first one-dimensional (1-D) version to assess x-ray ablation and radiation hydrodynamics expansion of target and ablated debris in the interior of a thick-liquid pocket. Real gas effects were taken into account through an approximate model. Concurrently, Liu [40, 38, 39] wrote the first two-dimensional (2-D) version of TSUNAMI to model ideal gas dynamics venting through the array of slab jets of the HYLIFE-II chamber. In addition, Liu developed a 1-D version that included a condensation model [38].

TSUNAMI was later employed to model ablation and gas dynamics phenomena in the National Ignition Facility (NIF) target chamber [13]. Scott [63] added multi-species capability and coupled TSUNAMI with the ABLATOR code [2, 3] and the SESAME database [42]. He employed his two-dimensional version of TSUNAMI to model gas dynamics in the NIF chamber [65] and mini-chamber [54, 64]. Scott's version was then expanded to include some radiation transport and a new real gas equation of state for flibe [34]. Simulations encompassing both the inside of the target chamber and the array of jets were first presented by Jantzen [32]. TSUNAMI was also used by Jantzen to design and model UCB's jet disruption experiment [33, 49]. Two groups used TSUNAMI to model gas dynamics phenomena inside dry-wall chambers [70, 36].

The author upgraded Scott's version, mainly with a real gas equation of state for flibe and a user-friendly input file builder and output file processor. The new code, TSUNAMI 2.8, was then used to predict the mass and energy fluxes at the beam ports of a HYLIFE-II-like chamber [24] and model the gas dynamics inside a beam tube for the first time [26]. In the

framework of the neutralized-ballistic Robust Point Design study [79, 77], the author [27] presented the first "integrated" simulation of a HYLIFE-II-like chamber, encompassing the whole domain of early-time gas dynamics, namely from the target implosion location to the site of the magnetic shutters introduced in Ref. [26]. Calderoni used and modified an early version of TSUNAMI 2.8 to model the UCLA flibe condensation experiment [8]. Recently, as part of the effort towards a heavy-ion fusion Modular Point Design [77, 78], the author [28] employed TSUNAMI 2.8 to model a variant of the Robust Point Design chamber suitable for the assisted-pinch transport scheme.

As already mentioned, Visual Tsunami 1.0 was first presented in Ref. [25]. The latest version, Visual Tsunami 2.0, is introduced in the next two sections. Fig. 2.1 shows an overview of the code.

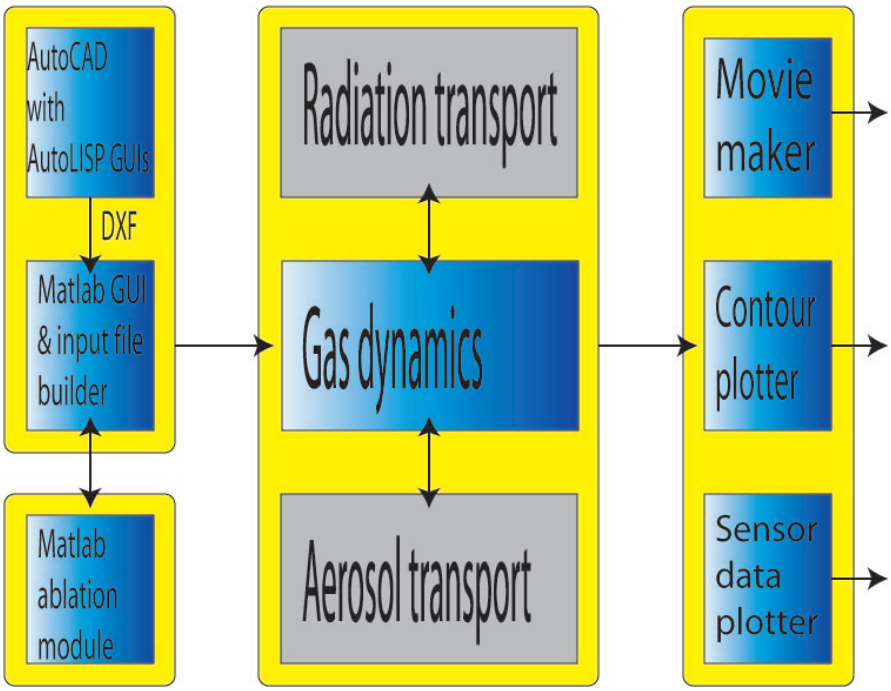

Figure 2.1: Architecture of Visual Tsunami 2.0: pre-processor tools (left), MATLAB core (center), and MATLAB post-processor. The implementation of radiation and aerosol transport models is left for future work.

2.3 Pre- and Post-Processors

2.3.1 Input File Builder

TSUNAMI has typically been used to model gas dynamics phenomena in complex geometries. In order to ease the setting up of the initial and boundary conditions, the author developed, in 2001, a modular 2-D mesher and template input file program in Fortran 95 [6]. The mesher was conveniently reusable from one simulation to the other and the formatting of the input files was taken care of by the builder entirely and automatically. Such a builder limited the amount of time and programming required to set up a new simulation, reduced the likelihood of making an input error, and represented a significant advance in user-friendliness.

Visual Tsunami makes use of current CAD software. Autodesk's AutoCAD was chosen for its wide use and its ability to be tailored. A set of graphical user interfaces (GUIs) was written for Visual Tsunami 1.0 in AutoLISP, AutoCAD's historical programming language, and is used to define most material properties, initial and boundary conditions in two dimensions. The AutoLISP GUIs could easily be expanded to incorporate more parameters. All the information is exported as a DXF file, the de-facto CAD file interchange standard. Fig. 2.2 shows one of the AutoLISP GUIs along with an AutoCAD 2004 window. Additionally, a GUI was developed in MATLAB for the mesher, the core of the input file builder.

The core of Visual Tsunami 2.0 is designed to handle 1-D, 2-D, and 3-D gas dynamics simulations, but only 2-D geometries can be specified through the pre-processor straightforwardly. The 3-D DXF file format is proprietary and has not been used. The object-oriented nature of the parser and mesher translates into "building blocks" that will allow an easy expansion to a different 3-D CAD format, similar to DXF but open source. Identifying the best

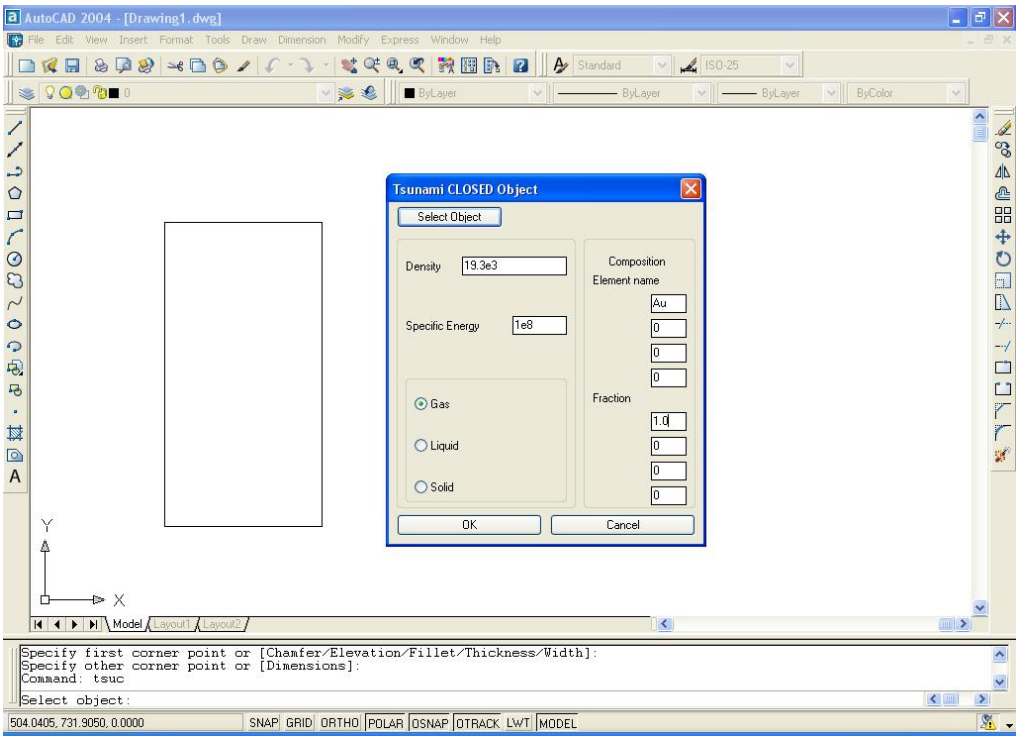

Figure 2.2: The AutoLISP GUI used to define material properties.

format, writing a new parser, and fine-tuning the GUI is left for future work. Alternatively, two-dimensional cutaway views can be expanded to 3-D through a set of MATLAB GUIs recently developed, but not yet fully tested.

X-rays interact with liquid or solid surfaces over time scales that are normally very short compared to the resulting gas dynamics phenomena. Ablation may therefore be considered instantaneous and treated as an initial condition to the gas dynamics simulations. Visual Tsunami can call an ablation program to define such initial conditions, whenever relevant. Visual Tsunami 1.0 was meant to make use of a Fortran 95 code written by the author; Visual Tsunami 2.0 could use this program, but was more particularly designed to make use of a MATLAB program based on the algorithm described in Chapter 6. Other ablation programs could be coupled in, such as the already mentioned ABLATOR code [2]. The user does not

have to flag the ablation surfaces. The ablation code performs ray-tracing automatically, a first in the history of the code.

2.3.2 Output File Processor

In Spring 2001, the author developed an extensive set of MATLAB output processing tools for two-dimensional TSUNAMI simulations. These consisted of a movie maker, contour and sensor data plotters. The output processor was recently revised for inclusion into Visual Tsunami, and, for instance, the speed of the movie maker was improved by more than an order of magnitude [6]. A set of MATLAB GUIs has been developed to streamline data reduction, make the code more versatile, and reduce the user's programming effort and likelihood of error input. Visual Tsunami 2.0 makes use of a variant of this fast and user-friendly post-processor.

2.4 Physical and Numerical Models

Visual Tsunami 1.0 and 2.0 solve the Euler equations for compressible flow in one, two or three dimensions in Cartesian coordinates. Visual Tsunami 2.0 can solve the Euler equations in two-dimensional axisymmetric cylindrical coordinates as well. The equations are solved using Godunov's approach: The flow field is determined by a succession of calls to a Riemann solver, at each time step and at each cell interface. Godunov's second method was implemented along with an exact solver to the exact Riemann problem. Visual Tsunami 1.0 solves the ideal gas Riemann problem while Visual Tsunami 2.0 can solve both ideal and real gas exact Riemann problems exactly. The ideal gas Riemann problem is reduced to a single equation in one unknown, the pressure in the middle region between the left and right waves. This equation is solved iteratively through the Newton-Raphson method. An elaborated initial

guess for the unknown pressure allows for a quick convergence in just a few iterations. The real gas case is treated in a similar manner. Details are presented in Chapter 3. Open outflow as well as immobile reflective and gas/liquid boundaries can be specified. Reflective boundaries are used on symmetry axes and at immobile gas/solid interfaces—the solid is then assumed to be perfectly rigid. Exact solutions to the Riemann problem are used for reflective and open boundaries. Gas/liquid boundaries can be modeled with a reflective boundary or through a novel condensation/evaporation model based on kinetics theory. This model is presented in Chapter 5 and still needs to be tested against more accurate models. As mentioned, ablation is treated along the lines described in Chapter 6. The ablation model takes into account a time-dependent x-ray pulse, hot opacities, reradiation, and heat diffusion.

The first two versions of Visual Tsunami are meant to be the basis on which future expansions of the code will be implemented easily. (Previous major upgrades to the code required a complete rewriting of the core.) For instance, implementation of high-order Godunov schemes would be fairly straight-forward, thanks to the modular and object-oriented nature of the code. Other boundary conditions could be implemented as well, such as Liu's condensation model [38]. Radiation transport could be added, for instance, through the method of fractional steps [68] and a flux-limited diffusion model, as described in Chapter 4. Visual Tsunami 1.0, being in Fortran 95, was meant to be fast and portable to supercomputers. Visual Tsunami 2.0, being in MATLAB, is meant to be a tool to explore new algorithms. A future version of Visual Tsunami could combine the MATLAB architecture of Visual Tsunami 2.0 and the Fortran performance of some of Visual Tsunami 1.0 subroutines for optimal performance, user-friendliness and portability. The core is highly vectorized and was designed to be easily parallelizable.

2.5 Conclusion

Visual Tsunami constitutes the latest version of the UCB code TSUNAMI. The gas dynamics core model—Euler's equations for compressible flows—has been retained from previous versions of TSUNAMI, as well as Godunov's approach. (However the implementations are significantly different.) Efficient schemes for ideal and real gas-dynamics have been researched, developed and implemented. A set of graphical user interfaces makes pre- and post-processing fast, intuitive, and straightforward. In particular, the input file builder is nowadays graphics-based. The geometry, the initial and boundary conditions can be specified in 2-D through AutoCAD, tailored with a set of AutoLISP GUIs. Details of the models and benchmarking of the code are presented in the following chapters.

Chapter 3

Compressible Gas Dynamics

3.1 Introduction to Eulerian Gas Dynamics

As previously stated, the gas dynamics models constitute a substantial part of the core of the simulation code Visual Tsunami. In this chapter, the equations of motion for a compressible non-diffusive (non-conducting and inviscid) multi-species gas are explored in the so-called “Eulerian” frame, which is fixed in the laboratory. Alternative formulations, such as the “Lagrangian” and “arbitrary Lagrangian Eulerian” frames, are deemed not practical for multi-dimensional gas dynamics. The Lagrangian formulation, in a reference frame that moves at the flow velocity, usually leads to highly distorted multi-dimensional meshes and is essentially only practical for our one-dimensional simulations for which its natural enforcement of mass conservation can lead to particularly attractive implementations. Arbitrary Lagrangian Eulerian frames move at velocities between zero and the fluid element velocity. Various multidimensional techniques that remap distorted meshes unto undistorted ones do exist, but they are not always satisfactory from a practical point of view since they may introduce numerical

diffusion [63].

3.1.1 The Euler Equations in Conservative Eulerian Form

When viscous and diffusive effects can be neglected, the dynamics of a compressible gas (or a liquid for that matter) is prescribed by a set of equations attributed to Euler. By "conservative," it is meant that these equations reflect how conserved quantities (mass, linear momentum, energy) change with respect to time. The equations of gas dynamics in Eulerian conservative form can be expressed as:[1]

$$\frac{\partial}{\partial t}\iiint_V \mathbf{U}(\mathbf{r},t)\,dV = -\iint_{\delta V} \mathbf{F}(\mathbf{U})(\mathbf{r},t)\cdot \mathbf{dS} \tag{3.1}$$

where V is the control volume, δV its surface. $\mathbf{dS}(\mathbf{r})$ is the elementary surface vector pointing along the outward normal to δV at the position $\mathbf{r}$. $\mathbf{U}$ is the vector of conserved quantities:

$$\mathbf{U} = \begin{pmatrix} \rho \\ \rho\omega_k \\ \rho u \\ \rho v \\ \rho w \\ \rho e_t \end{pmatrix} \tag{3.2}$$

[1] No derivation of these equations is given here.

and $\mathbf{F}(\mathbf{U})$ is the flux of conserved quantities:

$$\mathbf{F(U)} = \begin{pmatrix} \mathbf{F}_x(\mathbf{U}) & \mathbf{F}_y(\mathbf{U}) & \mathbf{F}_z(\mathbf{U}) \end{pmatrix} = \begin{pmatrix} \rho u & \rho v & \rho w \\ \rho \omega_k u & \rho \omega_k v & \rho \omega_k w \\ \rho u^2 + p & \rho uv & \rho uw \\ \rho uv & \rho v^2 + p & \rho vw \\ \rho uw & \rho vw & \rho w^2 + p \\ \rho u e_t + up & \rho v e_t + vp & \rho w e_t + wp \end{pmatrix} \tag{3.3}$$

where ρ is the gas density, u, v, and w are the three components of the velocity vector, ω_k is the mass fraction of the kth species, and e_t is the gas specific total energy, which is the sum of the specific kinetic and internal energies:

$$e_t = \frac{1}{2}(u^2 + v^2 + w^2) + e \tag{3.4}$$

Eq. 3.1 states that the values of the conserved quantities can change in the control volume V if and only if a non-zero net flux of these conserved quantities exists on the boundary δV of the control volume V. This assumes that there is no nuclear nor chemical reaction and that body forces such as gravity and electromagnetic forces can be neglected.

It is further assumed that the fluid is in Local Chemical Equilibrium (LCE) and in Local Thermodynamics Equilibrium (LTE). The former means that chemical phenomena happen on time scales much smaller than those of the gas dynamics phenomena of interest; the latter implies that the different species have the same temperature. Closure is then obtained through an equation of state relating the pressure p to the mass fractions and the canonical variables, the density ρ and the specific internal energy e.

Assuming that the flow is smooth, the divergence theorem can be applied to the integral

form of Euler's equations, Eq. 3.1, to obtain the following system of differential equations:

$$\frac{\partial \mathbf{U}}{\partial t} + \nabla \cdot \mathbf{F} = 0 \tag{3.5}$$

3.1.2 A Flavor of the Method of Characteristics

The canonical hyperbolic equation is given by a special form of the wave equation:

$$\frac{\partial c}{\partial t} + c\frac{\partial c}{\partial x} = 0 \tag{3.6}$$

where c is a function of x and t. The initial conditions are given most generally by

$$c = c(x, t_0) \tag{3.7}$$

and the boundary conditions are

$$\lim_{x \to \pm\infty} c(x,t) = \lim_{x \to \pm\infty} c(x, t_0) \tag{3.8}$$

The partial differential equation can be reduced to an ordinary differential equation by making use of the total derivative of c with respect to t:

$$\frac{dc}{dt} = \frac{\partial c}{\partial t} + \frac{\partial c}{\partial x}\frac{dx}{dt} \tag{3.9}$$

and identifying terms. Along the so-called "characteristic" path given by

$$\frac{dx}{dt} = c \tag{3.10}$$

Eq. 3.6 simplifies to

$$0 = \frac{\partial c}{\partial t} + c\frac{\partial c}{\partial x} = \frac{\partial c}{\partial t} + \frac{dx}{dt}\frac{\partial c}{\partial x} = \frac{dc}{dt} \tag{3.11}$$

Hence, the value of $c(x,t)$ remains the same along the characteristic tracing through (x,t). Since c is a constant along the characteristic given by Eq. 3.10, the same equation shows that

all the characteristics are straight lines. Mathematically, the implicit solution to Eq. 3.6 with initial conditions given by Eq. 3.7 and boundary conditions by Eq. 3.8 is therefore:

$$c(x,t) = c(x_0,t_0) \text{ along } x - x_0 = c(x_0,t_0)(t - t_0) \tag{3.12}$$

(By definition of x_0, the characteristic passing through (x,t) crosses the axis $t = t_0$ at $x = x_0$.) The value of $c(x,t)$ can be determined by choosing iteratively a value of x_0 until the characteristic equation $x - x_0 = c(x_0,t_0)(t - t_0)$ is satisfied.

The following seemingly simple discontinuous initial conditions are now considered:

$$c(x,0) = \begin{cases} c_l & \text{if } x < 0 \\ c_r & \text{if } x > 0 \end{cases} \tag{3.13}$$

where $c_l \neq c_r$. If c_r is greater than c_l, a given point in the plane (x,t) can be crossed by zero or one characteristic. The solution to Eq 3.6 given by Eq. 3.12 is valid in the two regions of the plane where any point lies on one and only one characteristic. In the middle region where there is no characteristic, one can build a continuous solution that matches the solutions in the two regions uniquely defined by the characteristics. The complete solution then reads:

$$c(x,t) = \begin{cases} c_l & \text{if } \frac{x}{t} \leq c_l \\ \frac{x}{t} & \text{if } c_l < \frac{x}{t} < c_r \\ c_r & \text{if } c_r \leq \frac{x}{t} \end{cases} \tag{3.14}$$

If c_l is greater than c_r, a given point in the plane (x,t) can be crossed by one or two characteristics. Where there are two characteristics, the solution is multivalued and the equation fails to describe the physical phenomenon of interest (except, possibly, in a few rare cases for which a multivalued solution is not physically impossible.) One has to resort to a better

modeling of the phenomenon or to modifying the solution and resigning oneself to obtaining a weak solution to the wave equation.

In the former case, a diffusive term would typically be added to the canonical hyperbolic equation given by Eq. 3.6 to yield the so-called Burgers equation:

$$\frac{\partial c}{\partial t} + c\frac{\partial c}{\partial x} = \alpha \frac{\partial^2 c}{\partial t^2} \tag{3.15}$$

Further discussion requires a knowledge of the physics of the system originally modeled with Eq. 3.6. (For gas dynamics applications, adding an appropriate viscous term to Euler's equations would yield the Navier-Stokes equations.)

Alternatively Eq 3.6 can be retained for the sake of simplicity and its solution modified in order to connect the left and right domains where the characteristic solution is valid. The left domain is prolonged to the right while the right domain is prolonged to the left. The two domains are patched by allowing for a discontinuity of the solution, which is called a shock. The location of the shock is not uniquely defined by the differential equation and the integral form of Eq. 3.6 needs to be evoked:

$$\int \left(\frac{\partial c}{\partial t} + \frac{\partial (\frac{1}{2}c^2)}{\partial x} \right) dx = 0 \tag{3.16}$$

The shock location is determined by the necessity of conserving the flux of c through the shock. This discussion was meant to introduce characteristics and their relationships to rarefaction and shock waves in a simple framework. These topics will be tackled in much further detail in the following sections, which focus on the resolution of the compressible Euler equations.

3.1.3 The Euler Equations in Characteristic Eulerian Form

Only the one-dimensional Euler equations resulting from a "split" three-dimensional formulation will be considered in this section for reasons that will become clear in Section 3.6, which deals with finite volume numerical schemes. The split formulation only considers the 3-D flux along one dimension. Equations 3.2 and 3.3 now read:

$$\mathbf{U} = \begin{pmatrix} \rho \\ \rho\omega_k \\ \rho u \\ \rho v \\ \rho w \\ \rho e_t \end{pmatrix} \tag{3.17}$$

and

$$\mathbf{F(U)} = \mathbf{F}_x(\mathbf{U}) = \begin{pmatrix} \rho u \\ \rho\omega_k u \\ \rho u^2 + p \\ \rho uv \\ \rho uw \\ \rho u e_t + up \end{pmatrix} \tag{3.18}$$

The following analysis is simpler if the energy conservation equation is replaced by the

entropy equation:

$$\frac{\partial}{\partial t}\begin{pmatrix}\rho\\ \rho\omega_k\\ \rho u\\ \rho v\\ \rho w\\ S\end{pmatrix}+\begin{pmatrix}\frac{\partial(\rho u)}{\partial x}\\ \frac{\partial(\rho\omega_k u)}{\partial x}\\ \frac{\partial(\rho u^2)}{\partial x}+\frac{\partial p}{\partial x}\\ \frac{\partial(\rho uv)}{\partial x}\\ \frac{\partial(\rho uw)}{\partial x}\\ u\frac{\partial S}{\partial x}\end{pmatrix}=0 \tag{3.19}$$

where S (J K^{-1} m^{-3}) is the entropy of the fluid per unit volume. (Entropy is conserved since there are neither viscous nor conductive nor radiative effects.) Hence,

$$\begin{pmatrix}\frac{\partial\rho}{\partial t}\\ \rho\frac{\partial\omega_k}{\partial t}+\omega_k\frac{\partial\rho}{\partial t}\\ \rho\frac{\partial u}{\partial t}+u\frac{\partial\rho}{\partial t}\\ \rho\frac{\partial v}{\partial t}+v\frac{\partial\rho}{\partial t}\\ \rho\frac{\partial w}{\partial t}+w\frac{\partial\rho}{\partial t}\\ \frac{\partial S}{\partial t}\end{pmatrix}+\begin{pmatrix}\rho\frac{\partial u}{\partial x}+u\frac{\partial\rho}{\partial x}\\ \omega_k\frac{\partial(\rho u)}{\partial x}+\rho u\frac{\partial\omega_k}{\partial x}\\ u\frac{\partial(\rho u)}{\partial x}+\rho u\frac{\partial u}{\partial x}+\frac{\partial p}{\partial x}\\ v\frac{\partial(\rho u)}{\partial x}+\rho u\frac{\partial v}{\partial x}\\ w\frac{\partial(\rho u)}{\partial x}+\rho u\frac{\partial w}{\partial x}\\ u\frac{\partial S}{\partial x}\end{pmatrix}=0 \tag{3.20}$$

which can be simplified using the mass conservation equation:

$$\begin{pmatrix}\frac{\partial\rho}{\partial t}\\ \frac{\partial\omega_k}{\partial t}\\ \rho\frac{\partial u}{\partial t}\\ \frac{\partial v}{\partial t}\\ \frac{\partial w}{\partial t}\\ \frac{\partial S}{\partial t}\end{pmatrix}+\begin{pmatrix}\rho\frac{\partial u}{\partial x}+u\frac{\partial\rho}{\partial x}\\ u\frac{\partial\omega_k}{\partial x}\\ \rho u\frac{\partial u}{\partial x}+\frac{\partial p}{\partial x}\\ u\frac{\partial v}{\partial x}\\ u\frac{\partial w}{\partial x}\\ u\frac{\partial S}{\partial x}\end{pmatrix}=0 \tag{3.21}$$

Methods to write systems of partial differential equations into characteristics form do exist. Here a less generic but more concise way is presented. By definition, the isentropic sound

speed a is given by:

$$a = \sqrt{\left.\frac{\partial p}{\partial \rho}\right|_S} \tag{3.22}$$

Multiplying part of the mass continuity equation by $\frac{1}{a^2}\left.\frac{\partial p}{\partial \rho}\right|_S = 1$ and adding the entropy equation multiplied by $\frac{1}{a^2}\left.\frac{\partial p}{\partial S}\right|_\rho$ yield:

$$\frac{1}{a^2}\left.\frac{\partial p}{\partial \rho}\right|_S \left(\frac{\partial \rho}{\partial t} + u\frac{\partial \rho}{\partial x}\right) + \rho\frac{\partial u}{\partial x} + \frac{1}{a^2}\left.\frac{\partial p}{\partial S}\right|_\rho \left(\frac{\partial S}{\partial t} + u\frac{\partial S}{\partial x}\right) = 0 \tag{3.23}$$

or

$$\frac{1}{a^2}\left(\left.\frac{\partial p}{\partial \rho}\right|_S \frac{\partial \rho}{\partial t} + \left.\frac{\partial p}{\partial S}\right|_\rho \frac{\partial S}{\partial t}\right) + \frac{u}{a^2}\left(\left.\frac{\partial p}{\partial \rho}\right|_S \frac{\partial \rho}{\partial x} + \left.\frac{\partial p}{\partial S}\right|_\rho \frac{\partial S}{\partial x}\right) + \rho\frac{\partial u}{\partial x} = 0 \tag{3.24}$$

which can be written as:

$$\frac{\partial p}{\partial t} + u\frac{\partial p}{\partial x} + \rho a^2\frac{\partial u}{\partial x} = 0 \tag{3.25}$$

Multiplying the x-momentum equation by the sound speed trivially gives:

$$a\frac{\partial p}{\partial x} + a\rho\frac{\partial u}{\partial t} + a\rho u\frac{\partial u}{\partial x} = 0 \tag{3.26}$$

Subtracting Eq. 3.26 from Eq. 3.25 yields:

$$\left(\frac{\partial}{\partial t} + (u-a)\frac{\partial}{\partial x}\right)p - a\rho\left(\frac{\partial}{\partial t} + (u-a)\frac{\partial}{\partial x}\right)u = 0 \tag{3.27}$$

Adding Eq. 3.26 to Eq. 3.25 gives:

$$\left(\frac{\partial}{\partial t} + (u+a)\frac{\partial}{\partial x}\right)p + a\rho\left(\frac{\partial}{\partial t} + (u+a)\frac{\partial}{\partial x}\right)u = 0 \tag{3.28}$$

The entropy equation was already in characteristic form:

$$\left(\frac{\partial}{\partial t} + u\frac{\partial}{\partial x}\right)S = 0 \tag{3.29}$$

as well as the transverse momentum equations:

$$\left(\frac{\partial}{\partial t} + u\frac{\partial}{\partial x}\right)v = 0 \tag{3.30}$$

$$\left(\frac{\partial}{\partial t}+u\frac{\partial}{\partial x}\right)w=0 \tag{3.31}$$

and the mass fraction equations:

$$\left(\frac{\partial}{\partial t}+u\frac{\partial}{\partial x}\right)\omega_k=0 \tag{3.32}$$

Hence,

$$\frac{dp}{dt}-a\rho\frac{du}{dt}=0 \text{ along } \frac{dx}{dt}=u-a \tag{3.33}$$

$$\frac{dS}{dt}=\frac{dv}{dt}=\frac{dw}{dt}=\frac{d\omega_k}{dt}=0 \text{ along } \frac{dx}{dt}=u \tag{3.34}$$

$$\frac{dp}{dt}+a\rho\frac{du}{dt}=0 \text{ along } \frac{dx}{dt}=u+a \tag{3.35}$$

Velocity and pressure are coupled together and move along characteristics at speeds equal to u plus or minus the sound speed a. The entropy, transverse components of linear momentum, and the mass fractions move along characteristics at the gas velocity. The quantities $dp\mp a\rho du$ are known as Riemann invariants. In integral forms, the Riemann invariants read:

$$u+\int\frac{1}{a\rho}dp=C_1 \text{ along } \frac{dx}{dt}=u-a \tag{3.36}$$

$$S=C_2\ \ v=C_3\ \ w=C_4\ \ \omega_k=C_{k+5} \text{ along } \frac{dx}{dt}=u \tag{3.37}$$

$$u-\int\frac{1}{a\rho}dp=C_5 \text{ along } \frac{dx}{dt}=u+a \tag{3.38}$$

where the various Cs are constant.

3.2 Gas Dynamics Equations of State

3.2.1 Definitions and Relations

As mentioned, the isentropic sound speed a (m s^{-1}) is defined by:

$$a=\sqrt{\left.\frac{\partial p}{\partial \rho}\right|_S} \tag{3.39}$$

This definition can be cumbersome to use and a handy expression as a function of readily available quantities is desired. The expansion rule gives:

$$a^2 = \left.\frac{\partial p}{\partial \rho}\right|_e + \left.\frac{\partial e}{\partial \rho}\right|_S \left.\frac{\partial p}{\partial e}\right|_\rho \tag{3.40}$$

The well-known relation from thermodynamics

$$dE = TdS + \frac{p}{\rho^2} d\rho \tag{3.41}$$

can be used to simplify the expression for a to:

$$a^2 = \left(\frac{\partial p}{\partial \rho}\right)_e + \frac{p}{\rho^2}\left(\frac{\partial p}{\partial e}\right)_\rho \tag{3.42}$$

The dimensionless "isentropic" (adiabatic) exponent, γ_i, is by definition:

$$\gamma_i = \left.\frac{\partial \ln(p)}{\partial \ln(\rho)}\right|_S = \frac{\rho}{p}\left.\frac{\partial p}{\partial \rho}\right|_S \tag{3.43}$$

Hence, by definition of the isentropic exponent and sound speed,

$$a = \sqrt{\frac{\gamma_i p}{\rho}} \tag{3.44}$$

Equivalently,

$$\gamma_i = \frac{\rho a^2}{p} \tag{3.45}$$

An "isothermal" γ is sometimes defined by:

$$\gamma_t = \frac{a^2}{\left.\frac{\partial p}{\partial \rho}\right|_T} \tag{3.46}$$

γ_i and γ_t are obviously related by:

$$\gamma_i = \gamma_t \frac{\rho}{p}\left(\frac{\partial p}{\partial \rho}\right)_T \tag{3.47}$$

A dimensionless "volumetric" γ can be defined as the ratio of enthalpy to internal energy:

$$\gamma_v(\rho, e) = \frac{\rho e + p}{\rho e} = 1 + \frac{p}{\rho e} \tag{3.48}$$

Equivalently:

$$p = (\gamma_v(\rho, e) - 1)\rho e \tag{3.49}$$

3.2.2 Ideal Gas Equations of State

The simplest equation of state is the ideal gas law according to which:

$$\gamma = \gamma_t = \gamma_v = \gamma_i = \frac{c_p}{c_v} \tag{3.50}$$

where c_p (J K^{-1} kg^{-1}) and c_v (J K^{-1} kg^{-1}) are the heat capacities at constant pressure and volume, respectively. The volumetric equation of state is then:

$$p = (\gamma - 1)\rho e \tag{3.51}$$

The well-known caloric equation of state is:

$$T = \frac{p}{\rho r} \tag{3.52}$$

where the gas constant r is given by

$$r = \frac{R}{M} \tag{3.53}$$

R is the universal gas constant[2] and M (kg mol^{-1}) is the molar mass of the gas. Trivially, the sound speed is then given by:

$$a = \sqrt{\frac{\gamma p}{\rho}} = \sqrt{\gamma r T} \tag{3.54}$$

An ideal gas with a constant γ is said to be polytropic.

3.2.3 Real Gas Equations of State

Countless equations of state for real gases are available in the scientific literature. A detailed accounting of the various physical models used to derive these equations of state is

[2] R=8.31 J mol^{-1} K^{-1}

outside of the scope of this doctoral dissertation; a quick overview of those equations of state that are relevant to the modeling of gaseous flibe is given in Appendix A.2. Information on the EOS of high temperature flinabe can be found in Ref. [83].

3.3 The Exact Riemann Problem: Exact Ideal Gas Case

3.3.1 Introduction and Physical Assumptions

The Riemann problem refers to an infinite one-dimensional multi-species gas tube with the following initial conditions:

$$\mathbf{U}(x,0) = \begin{cases} \mathbf{U}_l & \text{if } x < 0 \\ \\ \mathbf{U}_r & \text{if } x > 0 \end{cases} \tag{3.55}$$

where, as usual, $\mathbf{U}$ is the vector of conserved physical quantities given by Eq. 3.2. The Riemann problem is an extension of the typical experimental shock tube apparatus, in which two still gases fill in two compartments and are separated by a diaphragm [74]. At $t = 0$, the diaphragm is burst and the gases are free to interact.

Neglecting viscosity and heat conduction, a solution to the Riemann problem is sought using the compressible Euler equations for a polytropic ideal gas. The Riemann problem is purely one-dimensional, but a “split” Riemann problem is considered in this section in anticipation of the finite volume numerical schemes to be developed in Section 3.6. The vector of conserved quantities therefore does include the term with the transverse momenta.

3.3.2 Mathematical Considerations: Simple and Shock Waves

When $\mathbf{U}_l \neq \mathbf{U}_r$, the solution to the Riemann problem is made of a combination of simple and shock waves. (The simple waves can either be contact discontinuities or rarefaction fans.) In this section, some properties of these simple and shock waves are explored and employed for the "standard" Riemann problem without initial nor generated vacuum. (The vacuum cases will be treated in Section 3.5.) Only those properties that are particularly useful to determine the analytical solution to the Riemann problem are discussed in depth.

Contact Discontinuity Waves

In the standard case, the middle wave is always a contact discontinuity. Across such a contact wave, velocity and pressure do not change:

$$u_l^* = u_r^* = u^* \tag{3.56}$$

$$p_l^* = p_r^* = p^* \tag{3.57}$$

(The "left" and "right" subscripts will be omitted hereafter for convenience.) Note that there is a change in density, sound speed, and specific energy across the contact. (It is a *discontinuity* wave after all!) The assumption of constant velocity and discontinuous density may sound like conservation of mass is not satisfied. Since the wave travels at the speed u^*, the gases ahead and behind the wave are immobile in the reference frame attached to the wave; in other words, there is no mass flux across the wave and mass conservation is indeed enforced.

Rarefaction Fan

A rarefaction fan appears when $p^* < p_{l,r}$. ($p_{l,r}$ refers to p_l or p_r, as appropriate.) It is assumed that rarefaction fans exhibit three major properties:

1. The *Riemann invariant* $dp = \pm a\rho du$ (defined in Section 3.1.3) holds across the finite width of a rarefaction. (The upper plus sign will be used throughout for a left rarefaction fan, the lower minus sign for a right rarefaction fan.)

2. The following *characteristic equation* holds inside a centered rarefaction fan:

$$u = \frac{x - x_0}{t} \pm a = \frac{x}{t} \pm a \tag{3.58}$$

3. Entropy is a constant throughout a rarefaction fan.

The flow being isentropic, the definition of the sounds speeds yields $dp = a^2 d\rho$ and the Riemann invariants now read:

$$du = \pm \frac{a}{\rho} d\rho \tag{3.59}$$

The adiabatic law applies and $\frac{p}{\rho^\gamma}$ is a constant in the rarefaction fan. This relation can be used to express the sound speed as a function of density. Starting from Eq. 3.54, the expression for the sound speed reads:

$$a = \sqrt{\frac{\gamma p}{\rho}} = \sqrt{\gamma \alpha_1 \rho^{\gamma - 1}} = \alpha_2 \rho^{\frac{\gamma-1}{2}} \tag{3.60}$$

where α_1 and α_2 are two constants. The integral in the Riemann invariant becomes:

$$\int \frac{a}{\rho} d\rho = \alpha_2 \int \rho^{\frac{\gamma-3}{2}} d\rho = \frac{2\alpha_2}{\gamma - 1} \rho^{\frac{\gamma-1}{2}} = \frac{2a}{\gamma - 1} \tag{3.61}$$

Hence, for an ideal gas, the Riemann invariant $u \pm \frac{2a}{\gamma-1}$ is constant across the width of a rarefaction fan:

$$u \pm \frac{2a}{\gamma_{l,r} - 1} = u_{l,r} \pm \frac{2a_{l,r}}{\gamma_{l,r} - 1} \tag{3.62}$$

where u and a are the speed and sound speed inside the fan at a location x and a time t. Substituting u from Eq. 3.58 into Eq. 3.62 yields:

$$\pm a \left(1 + \frac{2}{\gamma_{l,r} - 1}\right) = u_{l,r} - \frac{x}{t} \pm \frac{2a_{l,r}}{\gamma_{l,r} - 1} \tag{3.63}$$

or

$$\left(\frac{\gamma_{l,r}+1}{\gamma_{l,r}-1}\right)a = \pm\left(u_{l,r}-\frac{x}{t}\right)+\frac{2a_{l,r}}{\gamma_{l,r}-1} \tag{3.64}$$

Equivalently,

$$a(x,t) = \frac{2}{\gamma_{l,r}+1}a_{l,r} \pm \frac{\gamma_{l,r}-1}{\gamma_{l,r}+1}\left(u_{l,r}-\frac{x}{t}\right) \tag{3.65}$$

u is then given by the characteristic equation:

$$u(x,t) = \frac{x}{t} \pm a = \frac{2}{\gamma_{l,r}+1}\left(\frac{x}{t}+\frac{\gamma_{l,r}-1}{2}u_{l,r} \pm a_{l,r}\right) \tag{3.66}$$

Using Eq. 3.44 yields:

$$\frac{a}{a_{l,r}} = \left(\frac{p}{\rho}\frac{\rho_{l,r}}{p_{l,r}}\right)^{\frac{1}{2}} \tag{3.67}$$

The adiabatic law applies inside the rarefaction fan:

$$\frac{p_{l,r}}{\rho_{l,r}^{\gamma_{l,r}}} = \frac{p}{\rho^{\gamma_{l,r}}} \tag{3.68}$$

or

$$\rho = \rho_{l,r}\left(\frac{p}{p_{l,r}}\right)^{\frac{1}{\gamma_{l,r}}} \tag{3.69}$$

Combining Eq. 3.67 and the previous equation yields,

$$\frac{a}{a_{l,r}} = \left(\frac{p}{p_{l,r}}\right)^{\frac{\gamma_{l,r}-1}{2\gamma_{l,r}}} \tag{3.70}$$

which leads to the following pressure and density formulae:

$$p(x,t) = p_{l,r}\left(\frac{a}{a_{l,r}}\right)^{\frac{2\gamma_{l,r}}{\gamma_{l,r}-1}} \tag{3.71}$$

and

$$\rho(x,t) = \rho_{l,r}\left(\frac{p}{p_{l,r}}\right)^{\frac{1}{\gamma_{l,r}}} = \rho_{l,r}\left(\frac{a}{a_{l,r}}\right)^{\frac{2}{\gamma_{l,r}-1}} \tag{3.72}$$

Eq. 3.62 can be used at the two edges of the fan—its so-called “tail” and “head”—to give:

$$u^* \pm \frac{2a^*_{l,r}}{\gamma_{l,r}-1} = u_{l,r} \pm \frac{2a_{l,r}}{\gamma_{l,r}-1} \tag{3.73}$$

Thus, u^* is given by:

$$u^* = u_{l,r} \pm \frac{2}{\gamma_{l,r}-1}\left(a_{l,r} - a^*_{l,r}\right) = u_{l,r} \pm \frac{2a_{l,r}}{\gamma_{l,r}-1}\left(1 - \frac{a^*_{l,r}}{a_{l,r}}\right) \tag{3.74}$$

The sound speed in the middle region is given by Eq. 3.70:

$$a^*_{l,r} = a_{l,r}\left(\frac{p^*}{p_{l,r}}\right)^{\frac{\gamma_{l,r}-1}{2\gamma_{l,r}}} \tag{3.75}$$

and the density in the middle region follows from Eq. 3.72:

$$\rho^*_{l,r} = \rho_{l,r}\left(\frac{p^*}{p_{l,r}}\right)^{\frac{1}{\gamma_{l,r}}} = \rho_{l,r}\left(\frac{a^*_{l,r}}{a_{l,r}}\right)^{\frac{2}{\gamma_{l,r}-1}} \tag{3.76}$$

Using Eq. 3.74 and Eq. 3.75, the velocity in the middle region can be expressed as a function of the pressure in the same zone and the state of the gas on the other side of the left or right wave:

$$u_* = u_{l,r} \pm \frac{2a_{l,r}}{\gamma_{l,r}-1}\left(1 - \left(\frac{p^*}{p_{l,r}}\right)^{\frac{\gamma_{l,r}-1}{2\gamma_{l,r}}}\right) \tag{3.77}$$

Eulerian Rankine-Hugoniot Shock Relations

Let's consider a left shock wave ($p^* > p_l$). In the reference frame of the shock, conservation of mass, linear momentum, and total energy can be intuitively formulated as:

$$\rho_l \hat{u}_l = \rho^*_l \hat{u}^* \tag{3.78}$$

$$\rho_l (\hat{u}_l)^2 + p_l = \rho^*_l (\hat{u}^*)^2 + p^* \tag{3.79}$$

$$\hat{u}_l\left(\frac{1}{2}\rho_l(\hat{u}_l)^2 + \rho_l e_l + p_l\right) = \hat{u}^*\left(\frac{1}{2}\rho^*_l(\hat{u}^*)^2 + \rho^*_l e^*_l + p^*\right) \tag{3.80}$$

The relative speeds on the left and right of the shock are given by:

$$\hat{u}_l = u_l - s \tag{3.81}$$

$$\hat{u}^* = u^* - s \tag{3.82}$$

where s is the shock speed. These Rankine-Hugoniot jump relations can be formerly derived from the integral form of the Euler equations.

Hugoniot Relation The momentum jump relation, Eq. 3.79, can be rewritten as:

$$\rho_l^*(\hat{u}^*)^2 - (\rho_l \hat{u}_l)\frac{\rho_l \hat{u}_l}{\rho_l} = p_l - p^* \tag{3.83}$$

Using the mass jump relation, Eq. 3.78, yields:

$$\rho_l^*(\hat{u}^*)^2 \left(1 - \frac{\rho_l^*}{\rho_l}\right) = p_l - p^* \tag{3.84}$$

Hence,

$$(\hat{u}^*)^2 = \frac{\rho_l}{\rho_l^*}\frac{p_l - p^*}{\rho_l - \rho_l^*} = \frac{\rho_l}{\rho_l^*}\frac{p^* - p_l}{\rho_l^* - \rho_l} \tag{3.85}$$

Similarly, one obtains by permuting the role of the left and right sides of the shock wave:

$$(\hat{u}_l)^2 = \frac{\rho_l^*}{\rho_l}\frac{p^* - p_l}{\rho_l^* - \rho_l} \tag{3.86}$$

The total energy jump relation, Eq. 3.80, can be written as:

$$\rho_l \hat{u}_l \left(\frac{1}{2}(\hat{u}_l)^2 + e_l + \frac{p_l}{\rho_l}\right) = \rho_l^* \hat{u}^* \left(\frac{1}{2}(\hat{u}^*)^2 + e_l^* + \frac{p^*}{\rho_l^*}\right) \tag{3.87}$$

Simplifying with the mass jump relation and rearranging give:

$$e_l^* - e_l = \frac{1}{2}\left((\hat{u}_l)^2 - (\hat{u}^*)^2\right) + \frac{p_l}{\rho_l} - \frac{p^*}{\rho_l^*} \tag{3.88}$$

$(\hat{u}^*)^2$ and $(\hat{u}_l)^2$ are given by Eq. 3.85 and Eq. 3.86:

$$e_l^* - e_l = \frac{1}{2}\frac{p^* - p_l}{\rho_l^* - \rho_l}\left(\frac{\rho_l^*}{\rho_l} - \frac{\rho_l}{\rho_l^*}\right) + \frac{p_l}{\rho_l} - \frac{p^*}{\rho_l^*} \tag{3.89}$$

$$= \frac{1}{2}\frac{p^* - p_l}{\rho_l^* - \rho_l}\frac{(\rho_l^*)^2 - (\rho_l)^2}{\rho_l\rho_l^*} + \frac{\rho_l^* p_l - \rho_l p^*}{\rho_l\rho_l^*} \tag{3.90}$$

$$= \frac{1}{\rho_l\rho_l^*}\left(\frac{1}{2}(p^* - p_l)(\rho_l^* + \rho_l) + \rho_l^* p_l - \rho_l p^*\right) \tag{3.91}$$

$$= \frac{1}{\rho_l\rho_l^*}\left(\frac{1}{2}(\rho_l^* p^* + \rho_l p^* - \rho_l^* p_l - \rho_l p_l) + \rho_l^* p_l - \rho_l p^*\right) \tag{3.92}$$

$$= \frac{1}{\rho_l\rho_l^*}\left(\frac{1}{2}p^*(\rho_l^* - \rho_l) + \frac{1}{2}p_l(\rho_l^* - \rho_l)\right) \tag{3.93}$$

$$= \frac{\rho_l^* - \rho_l}{\rho_l\rho_l^*}\frac{p_l + p^*}{2} \tag{3.94}$$

Finally, the Hugoniot relation is obtained:

$$e_l^* - e_l = \frac{p_l + p^*}{2}\left(\frac{1}{\rho_l} - \frac{1}{\rho_l^*}\right) \tag{3.95}$$

A Few Other Useful Relations Introducing the ideal gas volumetric equation of state $p = (\gamma - 1)\rho e$ into Eq. 3.95 yields:

$$\frac{p^*}{(\gamma_l - 1)\rho_l^*} - \frac{p_l}{(\gamma_l - 1)\rho_l} = \frac{p_l + p^*}{2}\left(\frac{1}{\rho_l} - \frac{1}{\rho_l^*}\right) \tag{3.96}$$

Multiplying by ρ_l^* gives:

$$\frac{p^*}{\gamma_l - 1} - \frac{p_l}{(\gamma_l - 1)}\frac{\rho_l^*}{\rho_l} = \frac{p_l + p^*}{2}\left(\frac{\rho_l^*}{\rho_l} - 1\right) \tag{3.97}$$

or

$$\frac{\rho_l^*}{\rho_l}\left(\frac{1}{2}(p_l + p^*) + \frac{p_l}{\gamma_l - 1}\right) = \frac{p^*}{\gamma_l - 1} + \frac{1}{2}(p_l + p^*) \tag{3.98}$$

Dividing by p_l and manipulating the equation yield:

$$\frac{\rho_l^*}{\rho_l}\left(\frac{1}{2}\frac{p^*}{p_l} + \frac{1}{2} + \frac{1}{\gamma_l - 1}\right) = \frac{p^*}{p_l}\left(\frac{1}{\gamma_l - 1} + \frac{1}{2}\right) + \frac{1}{2} \tag{3.99}$$

Multiplying by two and rearranging give:

$$\frac{\rho_l^*}{\rho_l}\left(\frac{p^*}{p_l}+\frac{\gamma_l+1}{\gamma_l-1}\right)=\left(\frac{\gamma_l+1}{\gamma_l-1}\right)\frac{p^*}{p_l}+1 \tag{3.100}$$

Finally, the formula for ρ_l^* as a function of p^* and the known left state is:

$$\rho_l^*=\rho_l\frac{\frac{p^*}{p_l}+\frac{\gamma_l-1}{\gamma_l+1}}{\frac{\gamma_l-1}{\gamma_l+1}\frac{p^*}{p_l}+1} \tag{3.101}$$

The same formula can be derived for right shock waves:

$$\rho_r^*=\rho_r\frac{\frac{p^*}{p_r}+\frac{\gamma_r-1}{\gamma_r+1}}{\frac{\gamma_r-1}{\gamma_r+1}\frac{p^*}{p_r}+1} \tag{3.102}$$

The momentum jump relation can be rewritten as:

$$(\rho_l\hat{u}_l)\hat{u}_l+p_l=(\rho_l^*\hat{u}^*)\hat{u}^*+p^* \tag{3.103}$$

Using the mass jump relation yields:

$$\hat{u}_l-\hat{u}^*=\frac{p^*-p_l}{\rho_l\hat{u}_l} \tag{3.104}$$

Using the definition of the relative speeds (Equations 3.81 and 3.82) gives:

$$u_l-u^*=\frac{p^*-p_l}{\rho_l\hat{u}_l} \tag{3.105}$$

Equivalently,

$$\rho_l\hat{u}_l=\frac{p^*-p_l}{u_l-u^*}=\frac{p^*-p_l}{\hat{u}_l-\hat{u}^*}=\frac{p^*-p_l}{\frac{\rho_l\hat{u}_l}{\rho_l}-\frac{\rho_l^*\hat{u}_*}{\rho_l^*}} \tag{3.106}$$

Using the mass flux jump relation yields,

$$(\rho_l\hat{u}_l)^2=\frac{p^*-p_l}{\frac{1}{\rho_l}-\frac{1}{\rho_l^*}}=\rho_l\frac{p^*-p_l}{1-\frac{\rho_l}{\rho_l^*}} \tag{3.107}$$

The ratio of densities across the shock follows from Eq. 3.101. Hence,

$$(\rho_l\hat{u}_l)^2=\rho_l\frac{p^*-p_l}{1-\frac{\frac{\gamma_l-1}{\gamma_l+1}\frac{p^*}{p_l}+1}{\frac{p^*}{p_l}+\frac{\gamma_l-1}{\gamma_l+1}}} \tag{3.108}$$

This relates the mass flux to the left state and p^* and can be simplified somewhat:

$$(\rho_l \hat{u}_l)^2 = \rho_l (p^* - p_l) \frac{\frac{\gamma_l - 1}{\gamma_l + 1} + \frac{p^*}{p_l}}{\frac{p^*}{p_l} + \frac{\gamma_l - 1}{\gamma_l + 1} - \frac{\gamma_l - 1}{\gamma_l + 1}\frac{p^*}{p_l} - 1} \tag{3.109}$$

$$= \rho_l (p^* - p_l) \frac{\frac{\gamma_l - 1}{\gamma_l + 1} + \frac{p^*}{p_l}}{\frac{\gamma_l - 1}{\gamma_l + 1}\left(1 - \frac{p^*}{p_l}\right) + \frac{p^*}{p_l} - 1} \tag{3.110}$$

$$= \rho_l (p^* - p_l) \frac{\frac{\gamma_l - 1}{\gamma_l + 1} p_l + p^*}{\frac{\gamma_l - 1}{\gamma_l + 1}(p_l - p^*) + (p^* - p_l)} \tag{3.111}$$

$$= \rho_l \frac{\frac{\gamma_l - 1}{\gamma_l + 1} p_l + p^*}{1 - \frac{\gamma_l - 1}{\gamma_l + 1}} \tag{3.112}$$

Hence,

$$(\rho_l \hat{u}_l)^2 = \frac{\frac{\gamma_l - 1}{\gamma_l + 1} p_l + p^*}{\frac{2}{(\gamma_l + 1)\rho_l}} \tag{3.113}$$

and

$$(\rho_l \hat{u}_l)^2 = \frac{\gamma_l - 1}{2} \rho_l p_l + \frac{\gamma_l + 1}{2} \rho_l p^* \tag{3.114}$$

Using Eq. 3.105 and Eq. 3.113 gives u^* as a function of p^* and the left state:

$$u^* = u_l - (p^* - p_l) \left(\frac{\frac{2}{(\gamma_l + 1)\rho_l}}{\frac{\gamma_l - 1}{\gamma_l + 1} p_l + p^*} \right)^{\frac{1}{2}} \tag{3.115}$$

The formula for a right shock wave is:

$$u^* = u_r + (p^* - p_r) \left(\frac{\frac{2}{(\gamma_r + 1)\rho_r}}{\frac{\gamma_r - 1}{\gamma_r + 1} p_r + p^*} \right)^{\frac{1}{2}} \tag{3.116}$$

The left shock speed is then given by Equations 3.81 and 3.114:

$$s_l = u_l - \hat{u}_l = u_l - \frac{1}{\rho_l} \left(\frac{\gamma_l - 1}{2} \rho_l p_l + \frac{\gamma_l + 1}{2} \rho_l p^* \right)^{\frac{1}{2}} \tag{3.117}$$

$$= u_l - \left(\frac{\gamma_l p_l}{\rho_l} \right)^{\frac{1}{2}} \left(\frac{\gamma_l - 1}{2\gamma_l} + \frac{\gamma_l + 1}{2\gamma_l} \frac{p^*}{p_l} \right)^{\frac{1}{2}} \tag{3.118}$$

Hence,

$$s_l = u_l - a_l \left(\frac{\gamma_l + 1}{2\gamma_l} \frac{p^*}{p_l} + \frac{\gamma_l - 1}{2\gamma_l} \right)^{\frac{1}{2}} \tag{3.119}$$

Similarly, the right shock speed is given by:

$$s_r = u_r + a_r \left(\frac{\gamma_r + 1}{2\gamma_r} \frac{p^*}{p_r} + \frac{\gamma_r - 1}{2\gamma_r} \right)^{\frac{1}{2}} \tag{3.120}$$

3.3.3 Implicit Analytical Solution to the Ideal Gas Riemann Problem

According to the theory of characteristics for hyperbolic equations, the solution to the Riemann problem is made of two, three or four waves. In the three-wave case, the middle wave is always a contact discontinuity; the left and right waves can be any combination of rarefaction and shock waves: a left shock and a right rarefaction, a left rarefaction and a right shock, left and right shock waves, or left and right rarefaction fans. The two-wave cases arise when the initial conditions include a vacuum side and are discussed in Section 3.5 along the four-wave case, which arises for an ideal gas when

$$\frac{2a_l}{\gamma_l - 1} + \frac{2a_r}{\gamma_r - 1} \leq u_r - u_l \tag{3.121}$$

The remainder of this section is devoted to the standard case, with the typical three-wave pattern, which will be illustrated in Section 3.7.

Determination of p^* and u^*

Let's define:

$$f(p^*, \rho, \omega, u, v, w, p) = \begin{cases} (p^* - p) \left(\frac{\frac{2}{(\gamma+1)\rho}}{p^* + \frac{\gamma-1}{\gamma+1} p} \right)^{\frac{1}{2}} & \text{if } p^* > p \\ \frac{2a}{\gamma-1} \left(\left(\frac{p^*}{p} \right)^{\frac{\gamma-1}{2\gamma}} - 1 \right) & \text{if } 0 < p^* < p \end{cases} \tag{3.122}$$

where $a = \sqrt{\frac{\gamma p}{\rho}}$. Eq. 3.77 and Eq. 3.115 show that for $p^* \in]0, \infty[\setminus \{p\}$, u^* is given as a function of p^* and the original left state by:

$$u^* = u_l - f(p^*, \rho_l, \omega_l, u_l, v_l, w_l, p_l) \tag{3.123}$$

The case $p^* = 0$ leads to a vacuum solution and is excluded in this section. $p^* = p$ only happens when $U_l = U_r$. Similarly, u^* can be expressed as a function of p^* and the right state:

$$u^* = u_r + f(p^*, \rho_r, \omega_\mathbf{r}, u_r, v_r, w_r, p_r) \tag{3.124}$$

p^* is then the solution to the following equation, obtained by subtracting Eq. 3.123 from Eq. 3.124:

$$f(p^*, \rho_l, \omega_\mathbf{l}, u_l, v_l, w_l, p_l) + f(p^*, \rho_r, \omega_\mathbf{r}, u_r, v_r, w_r, p_r) + u_r - u_l = 0 \tag{3.125}$$

Once p^* is known, it is trivial to obtain u^*. Adding Eq. 3.123 to Eq. 3.124 gives:

$$u^* = \frac{u_r + u_l + f(p^*, \rho_r, \omega_\mathbf{r}, u_r, v_r, w_r, p_r) - f(p^*, \rho_l, \omega_\mathbf{l}, u_l, v_l, w_l, p_l)}{2} \tag{3.126}$$

Solution sampler

The state of the gas at any location x and at any time t can then readily be obtained by determining the wave pattern and in what region of the plan the point (x, t) lies. If the point is left of the contact, one checks first if the left wave is a shock or a rarefaction fan. If the left wave is a shock, the point (x, t) can be on the left side of the shock (where the gas is still at the initial left state) or on the right of the shock in the left star region. If the left wave is a rarefaction, three cases need to be considered: if the point is on the left of the rarefaction "head," inside the rarefaction fan, or in the left star region on the right of the rarefaction "tail." A point on the right of the contact can be treated in a similar manner.

Mathematically, if $\frac{x}{t} \leq u^*$ (left-hand side of the contact wave)

$$\begin{bmatrix} \omega & v & w \end{bmatrix} = \begin{bmatrix} \omega_{\mathbf{l}} & v_l & w_l \end{bmatrix} \tag{3.127}$$

$$\begin{bmatrix} \rho & u & p \end{bmatrix} = \begin{cases} \text{if } p^* > p_l \begin{cases} \begin{bmatrix} \rho_l & u_l & p_l \end{bmatrix} \text{ if } \frac{x}{t} < s_l \\ \begin{bmatrix} (3.101) & u^* & p^* \end{bmatrix} \text{ if } s_l < \frac{x}{t} < u^* \end{cases} \\ \text{if } p^* < p_l \begin{cases} \begin{bmatrix} \rho_l & u_l & p_l \end{bmatrix} \text{ if } \frac{x}{t} \leq u_l - a_l \\ \begin{bmatrix} (3.72) & (3.66) & (3.71) \end{bmatrix} \text{ if } u_l - a_l \leq \frac{x}{t} \leq u^* - a_l^* \\ \begin{bmatrix} (3.76) & u^* & p^* \end{bmatrix} \text{ if } u^* - a_l^* \leq \frac{x}{t} < u^* \end{cases} \end{cases} \tag{3.128}$$

and if $\frac{x}{t} \geq u^*$ (right-hand side of the contact wave)

$$\begin{bmatrix} \omega & v & w \end{bmatrix} = \begin{bmatrix} \omega_{\mathbf{r}} & v_r & w_r \end{bmatrix} \tag{3.129}$$

$$\begin{bmatrix} \rho & u & p \end{bmatrix} = \begin{cases} \text{if } p^* > p_r \begin{cases} \begin{bmatrix} (3.102) & u^* & p^* \end{bmatrix} \text{ if } u^* < \frac{x}{t} < s_r \\ \begin{bmatrix} \rho_r & u_r & p_r \end{bmatrix} \text{ if } \frac{x}{t} > s_r \end{cases} \\ \text{if } p^* < p_r \begin{cases} \begin{bmatrix} (3.76) & u^* & p^* \end{bmatrix} \text{ if } u^* < \frac{x}{t} \leq u^* + a_r^* \\ \begin{bmatrix} (3.72) & (3.66) & (3.71) \end{bmatrix} \text{ if } u^* + a_r^* \leq \frac{x}{t} \leq u_r + a_r \\ \begin{bmatrix} \rho_r & u_r & p_r \end{bmatrix} \text{ if } \frac{x}{t} \geq u_r + a_r \end{cases} \end{cases} \tag{3.130}$$

where s_l, $a_{l,r}^*$, and s_r are given by Equations 3.119, 3.75, and 3.120, respectively.

3.3.4 Numerical Model and Choice of Root Solver

The state of the gas is undefined at the location of the contact and, if applicable, at the position of any shock. In practice, one can arbitrarily define the state of the gas at these discontinuities by making all the inequalities on $\frac{x}{t}$ non strict in Equations 3.128 and 3.130. Let's define a function $g(p^*, \rho_l, \boldsymbol{\omega_l}, u_l, v_l, w_l, p_l, \rho_r, \boldsymbol{\omega_r}, u_r, v_r, w_r, p_r)$ by:

$$g = f(p^*, \rho_l, \boldsymbol{\omega_l}, u_l, v_l, w_l, p_l) + f(p^*, \rho_r, \boldsymbol{\omega_r}, u_r, v_r, w_r, p_r) + u_r - u_l \tag{3.131}$$

where f is given by Eq. 3.122. Solving Eq. 3.125 comes down to finding the value of p^* that satisfies:

$$g(p^*, \rho_l, \boldsymbol{\omega_l}, u_l, v_l, w_l, p_l, \rho_r, \boldsymbol{\omega_r}, u_r, v_r, w_r, p_r) = 0 \tag{3.132}$$

While g is a function of thirteen variables, twelve of its arguments are known parameters. Hence, Eq. 3.132 can be solved using a variety of root solvers for functions of *one* variable. The root solver could iterate to a value of p^* such as $p^* = p_l$ or $p^* = p_r$. The case $p = p_{l,r}$ can be handled by extending the definition of f using, say, the rarefaction branch:

$$f(p^*, \rho, \omega, u, v, w, p) = \begin{cases} (p^* - p)\left(\frac{\frac{2}{(\gamma+1)\rho}}{p^* + \frac{\gamma-1}{\gamma+1}p}\right)^{\frac{1}{2}} & \text{if } p^* > p \\ \frac{2a}{\gamma-1}\left(\left(\frac{p^*}{p}\right)^{\frac{\gamma-1}{2\gamma}} - 1\right) & \text{if } 0 < p^* \leq p \end{cases} \tag{3.133}$$

When the root is close to zero and the initial guess is poor, the root solvers may iterate to negative value of p^* for which g is undefined. The root solvers can be modified to reset p^* to some small positive number ε whenever needed. Equivalently, the definition of g and all its derivatives can be modified so that:

$$(\forall p^* < \varepsilon) \;\; g(p^*) = g(\varepsilon) \;\; g'(p^*) = g'(\varepsilon) \tag{3.134}$$

and similarly for the higher derivatives. (The known parameters of the function g are not shown hereafter.) The latter method is numerically equivalent and slightly easier to implement.

The secant and Newton-Raphson schemes are among the most frequently used root solvers. The secant iteration is given by:

$$p_{n+1}^* = p_n^* - \frac{(p_n^* - p_{n-1}^*)g(p_n^*)}{g(p_n^*) - g(p_{n-1}^*)} \tag{3.135}$$

for $n \in \mathbb{N}^*$. The two most natural guesses for p^* are the initial values of pressure; for instance, the iteration can be started with:

$$(p_0^*, p_1^*) = (p_l, p_r) \tag{3.136}$$

(Obviously, the initial guesses need to be adjusted when $p_l = p_r$.) The secant method is robust and each of its iterations requires relatively few operations. However, the convergence of the modified secant method is rather slow, being only supralinear. Since the Riemann solver is the core of the reconstruction-evolution methods described in Section 3.6, implementing a method with at least a quadratic convergence may save a substantial amount of computing time. The Newton-Raphson iteration is based on:

$$p_{n+1}^* = p_n^* - \frac{g(p_n^*)}{g^{'}(p_n^*)} \tag{3.137}$$

for $n \in \mathbb{N}$. Actually, the secant method is the Newton-Raphson scheme with the following additional approximation:

$$g^{'}(p_n^*) \approx \frac{g(p_n^*) - g(p_{n-1}^*)}{p_n^* - p_{n-1}^*} \tag{3.138}$$

The Newton-Raphson scheme is robust and converges quadratically. Compared to the secant method, its iteration step is more computationally intensive due to the evaluation of the derivative, but its higher convergence rate means fewer iterations for a sufficiently small tolerance. Experience shows that a properly implemented Newton-Raphson scheme is indeed faster than the secant method. The Visual Tsunami secant and Newton-Raphson schemes turned out to be faster than MATLAB's root solver, which implements Brent's algorithm [46].

Higher-order methods can be used as well, but, because of their increase in computing time per iteration, they are only worth it for very small tolerances. A Householder cubic method

$$p^*_{n+1} = p^*_n - \frac{g(p^*_n)}{g^{'}(p^*_n)}\left(1 + \frac{g(p^*_n)g^{''}(p^*_n)}{2(g^{'}(p^*_n))^2}\right) \tag{3.139}$$

and a Householder quartic scheme

$$p^*_{n+1} = p^*_n - \frac{g(p^*_n)}{g^{'}(p^*_n)}\left(1 + \frac{g(p^*_n)g^{''}(p^*_n)}{2(g^{'}(p^*_n))^2} + \frac{(g(p^*_n))^2(3(g^{''}(p^*_n))^2 - g^{'}(p^*_n)g^{'''}(p^*_n))}{6(g^{'}(p^*_n))^4}\right) \tag{3.140}$$

were implemented in Visual Tsunami. The high-order schemes can be started with the simple guess:

$$p^*_0 = \frac{p_l + p_r}{2} \tag{3.141}$$

Experience indicates that one of the best initial guesses is given by the analytic solution to the Riemann problem assuming that $\gamma = \frac{\gamma_l + \gamma_r}{2}$ and that two rarefaction waves are present. From Eq. 3.125, p^*_0 is then given by:

$$\frac{2a_l}{\gamma - 1}\left(\left(\frac{p^*_0}{p_l}\right)^{\frac{\gamma-1}{2\gamma}} - 1\right) + \frac{2a_r}{\gamma - 1}\left(\left(\frac{p^*_0}{p_r}\right)^{\frac{\gamma-1}{2\gamma}} - 1\right) + u_r - u_l = 0 \tag{3.142}$$

Hence,

$$(p^*_0)^{\frac{\gamma-1}{2\gamma}}\left(\frac{a_l}{p_l^{\frac{\gamma-1}{2\gamma}}} + \frac{a_r}{p_r^{\frac{\gamma-1}{2\gamma}}}\right) = a_l + a_r - \frac{1}{2}(\gamma - 1)(u_r - u_l) \tag{3.143}$$

Finally,

$$p^*_0 = \left(\frac{a_l + a_r - \frac{1}{2}(\gamma - 1)(u_r - u_l)}{\left(\frac{a_l}{p_l^{\frac{\gamma-1}{2\gamma}}} + \frac{a_r}{p_r^{\frac{\gamma-1}{2\gamma}}}\right)}\right)^{\frac{2\gamma}{\gamma-1}} \tag{3.144}$$

This guess is obviously the exact answer if $\gamma_l = \gamma_r$ and the solution consists of two rarefaction waves. Numerical experiments show that this approximation is still good in the case of weak shocks and hence provides an excellent first guess to initiate the iteration.

3.4 The Exact Riemann Problem: Exact Real Gas Case

The ideal gas Riemann solver essentially follows Godunov's original approach as refined by several decades of CFD practices [72, 30]. A solution to the Riemann problem described in the previous section is now developed for a gas obeying a real gas equation of state. No satisfying scheme was found in the literature and an exact, yet simple approach was developed for this doctoral dissertation. (Colella and Glaz's solver [19] was used in previous versions of TSUNAMI. Other solvers were proposed by Saurel and co-workers [60].)

3.4.1 Mathematical Tools: Simple and Shock Waves

Contact Discontinuity Wave

As for the ideal gas case, the velocity and pressure do not change across the contact:

$$u_l^* = u_r^* = u^* \tag{3.145}$$

$$p_l^* = p_r^* = p^* \tag{3.146}$$

while density, sound speed, specific energy, and volumetric exponent will change.

Shock Wave

The Rankine-Hugoniot shock relations—Equations 3.78, 3.79, and 3.80—are the same and lead to the same Eq. 3.95; hence the same Hugoniot formula relates the jump in specific internal energy to the pressures and densities on both sides of the shock:

$$e_{l,r}^* - e_{l,r} = \frac{p_{l,r} + p^*}{2}\left(\frac{1}{\rho_{l,r}} - \frac{1}{\rho_{l,r}^*}\right) \tag{3.147}$$

Making use of the definition of the volumetric exponent given in Eq. 3.48 and following the same mathematical steps performed in the ideal gas case leads from the Hugoniot relation

to the formula for the densities on both sides of a shock wave:

$$\rho^*_{l,r} = \rho_{l,r} \frac{\frac{\gamma^*_{l,r}+1}{\gamma^*_{l,r}-1}\frac{p^*}{p_{l,r}} + 1}{\frac{p^*}{p_{l,r}} + \frac{\gamma_{l,r}+1}{\gamma_{l,r}-1}} \tag{3.148}$$

As for the ideal gas case, the jump in speed can be related to the ratio of pressure difference to mass flux:

$$u^* = u_{l,r} \mp \frac{p^* - p_{l,r}}{\rho_{l,r}\hat{u}_{l,r}} \tag{3.149}$$

where

$$(\rho_{l,r}\hat{u}_{l,r})^2 = \frac{p^* - p_{l,r}}{\frac{1}{\rho_{l,r}} - \frac{1}{\rho^*_{l,r}}} \tag{3.150}$$

(The minus is for a left shock; the plus sign for a right shock.) Hence,

$$u^* = u_{l,r} \mp \sqrt{(p^* - p_{l,r})\left(\frac{1}{\rho_{l,r}} - \frac{1}{\rho^*_{l,r}}\right)} \tag{3.151}$$

Using Eq. 3.148 yields:

$$u^* = u_{l,r} - \sqrt{\frac{p^* - p_{l,r}}{\rho_{l,r}}\left(1 - \frac{\frac{p^*}{p_{l,r}} + \frac{\gamma_{l,r}+1}{\gamma_{l,r}-1}}{\frac{\gamma^*_{l,r}+1}{\gamma^*_{l,r}-1}\frac{p^*}{p_{l,r}} + 1}\right)} \tag{3.152}$$

No significant further simplification is readily possible for the real gas case. As usual, the shock speed is given by:

$$s_{l,r} = u_{l,r} \mp \hat{u}_{l,r} \tag{3.153}$$

$$s_{l,r} = u_{l,r} \mp \frac{\sqrt{\frac{p^* - p_{l,r}}{\frac{1}{\rho_{l,r}} - \frac{1}{\rho^*_{l,r}}}}}{\rho_{l,r}} \tag{3.154}$$

Rarefaction Fan

Rarefaction waves are significantly more complicated in the real gas case than in its ideal counterpart. The integral form of the Riemann invariant still reads:

$$u^* = u_l - \int_{\rho_l}^{\rho_l^*} \frac{a}{\rho}\, d\rho \tag{3.155}$$

In the ideal gas case, the integrand $\frac{a}{\rho}$ can be expressed as a function of ρ and the constant exponent γ. The integration is then straight-forward. In the real gas rarefaction fan, no simple relationship between the gas state in the middle region and the known state on the other side of the rarefaction can be derived, except for a few sufficiently simple analytical real gas equations of state [71, 57].

3.4.2 New and State-Of-The-Art Analytical and Numerical Models

Closely following the ideal gas case, the exact solution to the real gas Riemann problem is obtained by enforcing the continuity of u^* through the contact:

$$f(p^*, \rho_l, \omega_\mathbf{l}, u_l, v_l, w_l, p_l) + f(p^*, \rho_r, \omega_\mathbf{r}, u_r, v_r, w_r, p_r) + u_r - u_l = 0 \tag{3.156}$$

The real gas function f is given by:

$$f(p^*, \rho, \omega, u, v, w, p) = \begin{cases} \sqrt{\frac{p^*-p}{\rho}\left(1 - \frac{\frac{p^*}{p}+\frac{\gamma+1}{\gamma-1}}{\frac{\gamma^*+1}{\gamma^*-1}\frac{p^*}{p}+1}\right)} & \text{if } p^* > p \\ \int_\rho^{\rho^*} \frac{a}{\rho}\, d\rho & \text{if } 0 < p^* \leq p \end{cases} \tag{3.157}$$

where $\gamma = 1 + \frac{p}{\rho e}$ is known and γ^* is the solution to the following trivial equation:

$$p^* - (\gamma^* - 1)\rho^* e^* = 0 \tag{3.158}$$

ρ^* is given by Eq. 3.148, e^* by the Hugoniot relation, and $p^*(\rho^*, e^*)$ by the volumetric equation of state. The equation for γ^* hence reads:

$$p^* - (\gamma^* - 1)\rho \frac{\frac{\gamma^*+1}{\gamma^*-1}\frac{p^*}{p}+1}{\frac{p^*}{p}+\frac{\gamma+1}{\gamma-1}} \left(e + \frac{p+p^*}{2\rho}\left(1 - \frac{\frac{p^*}{p}+\frac{\gamma+1}{\gamma-1}}{\frac{\gamma^*+1}{\gamma^*-1}\frac{p^*}{p}+1}\right)\right) = 0 \tag{3.159}$$

Both Equations 3.156 and 3.159 can be solved through the secant method, or alternatively, Brent's algorithm [46]. This algorithm trivially reduces to its ideal gas law counterpart if γ is a constant.

For the rarefaction branch, the integral of the Riemann invariant can be evaluated numerically:

$$\int_{\rho}^{\rho^*} \frac{a}{\rho} d\rho = -\sum_i \frac{a(\rho_i, e_i)}{\rho_i} \Delta\rho \tag{3.160}$$

where ρ_i and e_i are defined recursively for $i \in \mathbb{N}^*$ by

$$\rho_i = \rho_{i-1} - \Delta\rho \tag{3.161}$$

and

$$e_i = e_{i-1} - \Delta e_i = e_{i-1} - \frac{p_{i-1}(\rho_{i-1}, e_{i-1})}{\rho_{i-1}^2} \Delta\rho \tag{3.162}$$

The first values are given by

$$(\rho_0, e_0) = (\rho_l, e_l) \tag{3.163}$$

The specific energy increment comes from the already encountered thermodynamics relationship:

$$de = T ds + \frac{p}{\rho^2} d\rho \tag{3.164}$$

which simplifies to

$$de = \frac{p}{\rho^2} d\rho \tag{3.165}$$

for an isentropic flow. The discrete integration is performed until ρ_i satisfies

$$|p(\rho_i, e_i) - p^*| < \text{relative tolerance} \times \max(p^*, 1) \tag{3.166}$$

The density increment can be defined as:

$$\Delta\rho = \text{relative tolerance} \times \max(\rho_l, 1) \tag{3.167}$$

The sampling procedure is similar to the ideal gas case. All the formulae needed have been discussed, except for those giving the state of the gas inside a rarefaction fan. For a left

rarefaction,

$$u = u_l - \int_{\rho_l}^{\rho} \frac{a}{\rho} d\rho = u_l + \sum_i \frac{a(\rho_i, e_i)}{\rho_i} \Delta\rho \tag{3.168}$$

where the sum is performed as before along the isentrope, this time until the characteristic equation is satisfied:

$$u = \frac{x}{t} + a \tag{3.169}$$

Eq. 3.168 returns $\rho(x,t)$, $u(x,t)$, $e(x,t)$, and $a(x,t)$. The remaining physical quantities are easily obtained through the equations of state.

Finally, the sampling procedure can be explicitly given by the following. On the left-hand side of the contact, namely if $\frac{x}{t} \leq u^*$

$$\begin{bmatrix} \omega & v & w \end{bmatrix} = \begin{bmatrix} \omega_l & v_l & w_l \end{bmatrix} \tag{3.170}$$

$$\begin{bmatrix} \rho & u & p & e \end{bmatrix} = \begin{cases} \text{if } p^* > p_l \begin{cases} \begin{bmatrix} \rho_l & u_l & p_l & e_l \end{bmatrix} \text{ if } \frac{x}{t} < s_l \\ \begin{bmatrix} \rho_l^* & u^* & p^* & e_l^* \end{bmatrix} \text{ if } s_l < \frac{x}{t} < u^* \end{cases} \\ \text{if } p^* < p_l \begin{cases} \begin{bmatrix} \rho_l & u_l & p_l & e_l \end{bmatrix} \text{ if } \frac{x}{t} \leq u_l - a_l \\ \begin{bmatrix} \text{(3.168) and EOS} \end{bmatrix} \text{ if } u_l - a_l \leq \frac{x}{t} \leq u^* - a_l^* \\ \begin{bmatrix} \rho_l^* & u^* & p^* & e_l^* \end{bmatrix} \text{ if } u^* - a_l^* \leq \frac{x}{t} < u^* \end{cases} \end{cases} \tag{3.171}$$

where s_l is given by Eq. 3.154. ρ_l^* and e_l^* were obtained through the root solver, as well as a_l^*, if the left wave is a rarefaction. Physically, both p and e cannot be chosen as independent variables; both are specified here in the sampling procedure since both will be used by the reconstruction-evolution methods of Section 3.6.

The right-hand side of the contact is treated in a similar manner. If the integral form of the Riemann invariant is tabulated as a function of ρ, e, and p^* for use in Eq. 3.157 and as a

function of ρ, e, u, and $\frac{x}{t}$ for use in the sampling procedure, a significant gain in run time can be achieved. If both the shock and rarefaction branches of Eq. 3.157 are tabulated, the real gas scheme approaches that of the ideal gas one, for a minor, if not trivial, loss of accuracy.

3.5 Exotic Riemann Cases

3.5.1 Uniform Initial Conditions

The case $\mathbf{U}_l = \mathbf{U}_r$ is trivial.

3.5.2 Left Vacuum

When $\rho_l = p_l = 0$, an explicit solution is available for an ideal gas:

$$[\rho, \omega, u, v, w, p, e] = \begin{cases} [0,0,0,0,0,0,0] & \text{if } \frac{x}{t} \leq u_r - \frac{2a_r}{\gamma_r - 1} \\ \text{right fan solution} & \text{if } u_r - \frac{2a_r}{\gamma_r - 1} \leq \frac{x}{t} \leq u_r + a_r \\ [\rho_r, \omega_r, u_r, v_r, w_r, p_r, e_r] & \text{if } \frac{x}{t} \geq u_r + a_r \end{cases} \tag{3.172}$$

For a real gas, the solution is assumed to read:

$$[\rho, \omega, u, v, w, p, e] = \begin{cases} [0,0,0,0,0,0,0] & \text{if } \frac{x}{t} \leq u_r + \int_{\rho_r}^{0} \frac{a}{\rho}\, d\rho \\ \text{right fan solution} & \text{if } u_r + \int_{\rho_r}^{0} \frac{a}{\rho}\, d\rho \leq \frac{x}{t} \leq u_r + a_r \\ [\rho_r, \omega_r, u_r, v_r, w_r, p_r, e_r] & \text{if } \frac{x}{t} \geq u_r + a_r \end{cases} \tag{3.173}$$

where the integration of the Riemann invariant is done as usual along the isentrope. The issue of the actual value and physical meaning of the vacuum speed is not addressed since it does not play any role when it comes to evaluating the flux vector required by the reconstruction-evolution methods to be tackled in Section 3.6.

3.5.3 Right Vacuum

When $\rho_r = p_r = 0$, an explicit solution is also available for an ideal gas:

$$[\rho, \omega, u, v, w, p, e] = \begin{cases} [\rho_l, \omega_l, u_l, v_l, w_l, p_l, e_l] & \text{if } \frac{x}{t} \leq u_l - a_l \\ \text{left fan solution} & \text{if } u_l - a_l \leq \frac{x}{t} \leq u_l + \frac{2a_l}{\gamma_l - 1} \\ [0, 0, 0, 0, 0, 0, 0] & \text{if } \frac{x}{t} \geq u_l + \frac{2a_l}{\gamma_l - 1} \end{cases} \tag{3.174}$$

For a real gas, the ideal gas solution is extended to:

$$[\rho, \omega, u, v, w, p, e] = \begin{cases} [\rho_l, \omega_l, u_l, v_l, w_l, p_l, e_l] & \text{if } \frac{x}{t} \leq u_l - a_l \\ \text{left fan solution} & \text{if } u_l - a_l \leq \frac{x}{t} \leq u_l - \int_{\rho_l}^{0} \frac{a}{\rho}\, d\rho \\ [0, 0, 0, 0, 0, 0, 0] & \text{if } \frac{x}{t} \geq u_l - \int_{\rho_l}^{0} \frac{a}{\rho}\, d\rho \end{cases} \tag{3.175}$$

As for the left vacuum case, the question of the actual value and physical meaning of the vacuum speed is not addressed.

3.5.4 Center Vacuum

Non-vacuum initial conditions can lead to appearance of vacuum. This arises when the inequality 3.121 holds true for an ideal gas:

$$\frac{2a_l}{\gamma_l - 1} + \frac{2a_r}{\gamma_r - 1} \leq u_r - u_l \tag{3.176}$$

The explicit solution to the center vacuum can been seen as a combination of the previous left and right vacuum solutions:

$$[\rho,\omega,u,v,w,p,e] = \begin{cases} [\rho_l,\omega_l,u_l,v_l,w_l,p_l,e_l] & \text{if } \frac{x}{t} \leq u_l - a_l \\ \text{left fan solution} & \text{if } u_l - a_l \leq \frac{x}{t} \leq u_l + \frac{2a_l}{\gamma_l - 1} \\ [0,0,0,0,0,0,0] & \text{if } u_l + \frac{2a_l}{\gamma_l - 1} \leq \frac{x}{t} \leq u_r - \frac{2a_r}{\gamma_r - 1} \\ \text{right fan solution} & \text{if } u_r - \frac{2a_r}{\gamma_r - 1} \leq \frac{x}{t} \leq u_r + a_r \\ [\rho_r,\omega_r,u_r,v_r,w_r,p_r,e_r] & \text{if } \frac{x}{t} \geq u_r + a_r \end{cases} \tag{3.177}$$

For a real gas, the escape velocities need to be evaluated with the appropriate form of the Riemann invariants:

$$-\int_{\rho_l}^{0} \frac{a}{\rho}\, d\rho - \int_{\rho_r}^{0} \frac{a}{\rho}\, d\rho \leq u_r - u_l \tag{3.178}$$

The solution reads:

$$[\rho,\omega,u,v,w,p,e] = \begin{cases} [\rho_l,\omega_l,u_l,v_l,w_l,p_l,e_l] & \text{if } \frac{x}{t} \leq u_l - a_l \\ \text{left fan solution} & \text{if } u_l - a_l \leq \frac{x}{t} \leq u_l - \int_{\rho_l}^{0} \frac{a}{\rho}\, d\rho \\ [0,0,0,0,0,0,0] & \text{if } u_l - \int_{\rho_l}^{0} \frac{a}{\rho}\, d\rho \leq \frac{x}{t} \leq u_r + \int_{\rho_r}^{0} \frac{a}{\rho}\, d\rho \\ \text{right fan solution} & \text{if } u_r + \int_{\rho_r}^{0} \frac{a}{\rho}\, d\rho \leq \frac{x}{t} \leq u_r + a_r \\ [\rho_r,\omega_r,u_r,v_r,w_r,p_r,e_r] & \text{if } \frac{x}{t} \geq u_r + a_r \end{cases} \tag{3.179}$$

The three vacuum cases are treated for completeness and robustness. Problems that rely on those are not best treated by reconstruction-evolution methods, or any algorithm based on the Euler equations for that matter—vacuum cases violate the continuum assumption, an essential hypothesis used to derive the Euler equations.

3.6 Reconstruction-Evolution Methods

Reconstuction-evolution methods constitute a large class of numerical schemes that can be applied to solve a variety of equations. They tend to be particularly powerful to solve hyperbolic equations. In most of this section, the physical domain is assumed to be discretized as a Cartesian grid. For the sake of generality, a non-uniform grid is described. In practice, non-uniform grids may be cumbersome to use and nested uniform grids or unstructured meshes are preferred.

By definition,

$$\Delta V_{i,j,k} = \Delta x_i \Delta y_j \Delta z_k \tag{3.180}$$

is the volume of the cell centered at $x = x_i$, $y = y_j$, and $z = z_k$. Trivially, $\bar{\mathbf{U}}^n_{i,j,k}$, the average at time $t = t^n$ of the vector of conserved quantities over the volume of the cell (i, j, k) is given by:

$$\bar{\mathbf{U}}^n_{i,j,k} = \frac{1}{\Delta V_{i,j,k}} \iiint_{\Delta V_{i,j,k}} \mathbf{U}(x,y,z,t^n)\, dxdydz \tag{3.181}$$

The integral form of the Euler equations applied to the cell (i, j, k) and integrated between t^n and t^{n+1} reads:

$$\begin{aligned}
&\iiint_{\Delta V_{i,j,k}} \left(\mathbf{U}(x,y,z,t^{n+1}) - \mathbf{U}(x,y,z,t^n)\right) dxdydz = \\
&+ \int_{t^n}^{t^{n+1}} dt \left(\iint_{S_{i-\frac{1}{2},j,k}} \mathbf{F}_x(x_{i-\frac{1}{2}},y,z,t)\, dydz - \iint_{S_{i+\frac{1}{2},j,k}} \mathbf{F}_x(x_{i+\frac{1}{2}},y,z,t)\, dydz \right) \\
&+ \int_{t^n}^{t^{n+1}} dt \left(\iint_{S_{i,j-\frac{1}{2},k}} \mathbf{F}_y(x,y_{j-\frac{1}{2}},z,t)\, dxdz - \iint_{S_{i,j+\frac{1}{2},k}} \mathbf{F}_y(x,y_{j+\frac{1}{2}},z,t)\, dxdz \right) \\
&+ \int_{t^n}^{t^{n+1}} dt \left(\iint_{S_{i,j,k-\frac{1}{2}}} \mathbf{F}_z(x,y,z_{k-\frac{1}{2}},t)\, dxdy - \iint_{S_{i,j,k+\frac{1}{2}}} \mathbf{F}_z(x,y,z_{k+\frac{1}{2}},t)\, dxdy \right)
\end{aligned} \tag{3.182}$$

The left-hand side of Eq. 3.182 can be trivially expressed as:

$$\iiint_{\Delta V_{i,j,k}} \left(\mathbf{U}(x,y,z,t^{n+1}) - \mathbf{U}(x,y,z,t^{n})\right) dxdydz = \Delta V_{i,j,k} \left(\bar{\mathbf{U}}^{n+1}_{i,j,k} - \bar{\mathbf{U}}^{n}_{i,j,k}\right) \tag{3.183}$$

An approximation to $\bar{\mathbf{U}}^{n}_{i,j,k}$ is supposed to be known to the required order in space and time. An approximation to $\bar{\mathbf{U}}^{n+1}_{i,j,k}$ is then sought to the same order. (Somewhat abusively, the exact solution and its approximation to first order in space and time will be denoted with the same symbol, as will the exact and approximate averaged quantities.)

3.6.1 First-Order Reconstruction: Piecewise Constant Interpolation

To first order in space, the approximated solution is assumed to be constant over the volume of the cell:

$$\mathbf{U}(x,y,z,t^{n}) = \bar{\mathbf{U}}^{n}_{i,j,k} \text{for } (x,y,z) \in [x_{i-\frac{1}{2}}, x_{i+\frac{1}{2}}] \times [y_{i-\frac{1}{2}}, y_{i+\frac{1}{2}}] \times [z_{i-\frac{1}{2}}, z_{i+\frac{1}{2}}] \tag{3.184}$$

A midpoint integration may be invoked to simplify the right-hand side of Eq. 3.182 to second order in space, yielding:

$$\begin{aligned} \Delta V_{i,j,k} \left(\bar{\mathbf{U}}^{n+1}_{i,j,k} - \bar{\mathbf{U}}^{n}_{i,j,k}\right) = \\ + \int_{t^n}^{t^{n+1}} \Delta y_j \Delta z_k \left(\mathbf{F}_x(\mathbf{U}(x_{i-\frac{1}{2}}, y_j, z_k, t)) - \mathbf{F}_x(\mathbf{U}(x_{i+\frac{1}{2}}, y_j, z_k, t))\right) dt \\ + \int_{t^n}^{t^{n+1}} \Delta x_i \Delta z_k \left(\mathbf{F}_y(\mathbf{U}(x_i, y_{j-\frac{1}{2}}, z_k, t)) - \mathbf{F}_y(\mathbf{U}(x_i, y_{j+\frac{1}{2}}, z_k, t))\right) dt \\ + \int_{t^n}^{t^{n+1}} \Delta x_i \Delta y_j \left(\mathbf{F}_z(\mathbf{U}(x_i, y_j, z_{k-\frac{1}{2}}, t)) - \mathbf{F}_z(\mathbf{U}(x_i, y_j, z_{k+\frac{1}{2}}, t))\right) dt \end{aligned} \tag{3.185}$$

The piecewise constant reconstruction leads to four split fluxes that are piecewise constant over their respective surfaces; the integration over the surface of the edges is therefore exact in the case of a piecewise constant reconstruction.

3.6.2 Evolution in the Case of a Piecewise Constant Reconstruction

The four fluxes at the cell edges can be *evaluated* by using the solutions to the four 1-D split Riemann problems between the two sides of the relevant cell edge. The integral Euler equations then read:

$$\begin{aligned}
&\Delta V_{i,j,k}\left(\overline{\mathbf{U}}^{n+1}_{i,j,k}-\overline{\mathbf{U}}^{n}_{i,j,k}\right)= \\
&+\int_{t^n}^{t^{n+1}}\Delta y_j\Delta z_k\left(\mathbf{F}_x(\mathbf{U}^{RP}_{i-\frac{1}{2},j,k}(0,t-t^n))-\mathbf{F}_x(\mathbf{U}^{RP}_{i+\frac{1}{2},j,k}(0,t-t^n))\right)dt \\
&+\int_{t^n}^{t^{n+1}}\Delta x_i\Delta z_k\left(\mathbf{F}_y(\mathbf{U}^{RP}_{i,j-\frac{1}{2},k}(0,t-t^n))-\mathbf{F}_y(\mathbf{U}^{RP}_{i,j+\frac{1}{2},k}(0,t-t^n))\right)dt \\
&+\int_{t^n}^{t^{n+1}}\Delta x_i\Delta y_j\left(\mathbf{F}_z(\mathbf{U}^{RP}_{i,j,k-\frac{1}{2}}(0,t-t^n))-\mathbf{F}_z(\mathbf{U}^{RP}_{i,j,k+\frac{1}{2}}(0,t-t^n))\right)dt
\end{aligned} \tag{3.186}$$

where, for instance, $\mathbf{U}^{RP}_{i-\frac{1}{2},j,k}(0,t-t^n)$ is the solution to the 1-D split Riemann problem given by:

$$U(x-x_{i-\frac{1}{2}},y_j,z_k,t^n)=\begin{cases} U(x^-_{i-\frac{1}{2}},y_j,z_k,t^n) & \text{if } x<x_{i-\frac{1}{2}} \\ U(x^+_{i-\frac{1}{2}},y_j,z_k,t^n) & \text{if } x>x_{i-\frac{1}{2}} \end{cases} \tag{3.187}$$

when evaluated at $x=x_{i-\frac{1}{2}}$. The solution to the Riemann problem is detailed in the last three Sections 3.3, 3.4 and 3.5. It is self-similar and only depends on the variable $\frac{x}{t}$. The time-integration in Eq. 3.186 can then be performed exactly and leads to:

$$\begin{aligned}
&\Delta V_{i,j,k}\left(\overline{\mathbf{U}}^{n+1}_{i,j,k}-\overline{\mathbf{U}}^{n}_{i,j,k}\right)= \\
&+\Delta t^n\Delta y_j\Delta z_k\left(\mathbf{F}_x(\mathbf{U}^{RP}_{i-\frac{1}{2},j,k}(0))-\mathbf{F}_x(\mathbf{U}^{RP}_{i+\frac{1}{2},j,k}(0))\right) \\
&+\Delta t^n\Delta x_i\Delta z_k\left(\mathbf{F}_y(\mathbf{U}^{RP}_{i,j-\frac{1}{2},k}(0))-\mathbf{F}_y(\mathbf{U}^{RP}_{i,j+\frac{1}{2},k}(0))\right) \\
&+\Delta t^n\Delta x_i\Delta y_j\left(\mathbf{F}_z(\mathbf{U}^{RP}_{i,j,k-\frac{1}{2}}(0))-\mathbf{F}_z(\mathbf{U}^{RP}_{i,j,k+\frac{1}{2}}(0))\right)
\end{aligned} \tag{3.188}$$

Hence,

$$\begin{aligned}\bar{\mathbf{U}}^{n+1}_{i,j,k} &= \bar{\mathbf{U}}^{n}_{i,j,k} \\ &+\frac{\Delta t^n}{\Delta x_i}\left(\mathbf{F}_x(\mathbf{U}^{RP}_{i-\frac{1}{2},j,k}(0)) - \mathbf{F}_x(\mathbf{U}^{RP}_{i+\frac{1}{2},j,k}(0))\right) \\ &+\frac{\Delta t^n}{\Delta y_j}\left(\mathbf{F}_y(\mathbf{U}^{RP}_{i,j-\frac{1}{2},k}(0)) - \mathbf{F}_y(\mathbf{U}^{RP}_{i,j+\frac{1}{2},k}(0))\right) \\ &+\frac{\Delta t^n}{\Delta z_k}\left(\mathbf{F}_z(\mathbf{U}^{RP}_{i,j,k-\frac{1}{2}}(0)) - \mathbf{F}_z(\mathbf{U}^{RP}_{i,j,k+\frac{1}{2}}(0))\right)\end{aligned} \tag{3.189}$$

This solution is exact as long as Δt^n is sufficiently small enough that the waves generated by the Riemann problems at t^n cannot travel more than half a cell during Δt^n. This is known as the Courant-Friedrichs-Levy (CFL) condition:

$$\Delta t^n < \frac{\min(\Delta x_i, \Delta y_j, \Delta z_k)}{\max(\text{wave speeds})} \tag{3.190}$$

where the minimum and maximum are taken over the whole computational domain so that the whole solution is advanced to the same time step. The reconstruction method based on a piecewise constant reconstruction and the exact evolution of a piecewise constant flow is known as the Godunov scheme. The scheme is considered first order accurate when waves are allowed to travel more than half the cell width and less than the full width. The scheme may fail if a wave travels more than a cell width during Δt^n.

3.6.3 Axially-Symmetric Cylindrical Coordinates

In cylindrical coordinates, with axial symmetry, the Euler equations read:

$$\frac{\partial \mathbf{U}}{\partial t} + \nabla \cdot \mathbf{F} + \mathbf{G} = 0 \tag{3.191}$$

where **U**, **F** and **G** are given by:

$$\mathbf{U} = \begin{pmatrix} \rho \\ \rho\omega_k \\ \rho u \\ \rho w \\ \rho e_t \end{pmatrix} \tag{3.192}$$

$$\mathbf{F(U)} = \begin{pmatrix} \mathbf{F}_r(\mathbf{U}) & \mathbf{F}_z(\mathbf{U}) \end{pmatrix} = \begin{pmatrix} \rho u & \rho w \\ \rho\omega_k u & \rho\omega_k w \\ \rho u^2 + p & \rho uw \\ \rho uw & \rho w^2 + p \\ \rho u e_t + up & \rho w e_t + wp \end{pmatrix} \tag{3.193}$$

$$\mathbf{G} = \begin{pmatrix} \frac{\rho u}{r} \\ \frac{\rho\omega_k u}{r} \\ \frac{\rho u^2}{r} \\ \frac{\rho uw}{r} \\ \frac{\rho u e_t + up}{r} \end{pmatrix} \tag{3.194}$$

This system of equations can be solved through the method of fractional steps. The first step solves the advective part, whose equations can be solved via the method already derived for Cartesian coordinates. The second step takes into account the terms that appear in cylin-

drical coordinates. The numerical model for this step is to first order:

$$\bar{\mathbf{U}}_{i,j}^{n+1} = \bar{\mathbf{U}}_{i,j}^{n} - \Delta t^n \begin{pmatrix} \frac{\bar{\rho}_{i,j}\bar{u}_{i,j}}{r_{i,j}} \\ \frac{\bar{\rho}_{i,j}\bar{\omega}_{k,i,j}\bar{u}_{i,j}}{r_{i,j}} \\ \frac{\bar{\rho}_{i,j}(\bar{u}_{i,j})^2}{r_{i,j}} \\ \frac{\bar{\rho}_{i,j}\bar{u}_{i,j}\bar{w}_{i,j}}{r_{i,j}} \\ \frac{\bar{u}_{i,j}(\bar{\rho}_{i,j}\bar{e}_{t,i,j}+\bar{p}_{i,j})}{r_{i,j}} \end{pmatrix} \tag{3.195}$$

where the quantities on the right-hand side comes from the advection step. If necessary, time-stepping can be used to control the accuracy of the solution. Alternatively, a MATLAB ordinary differential equation solver could be employed.[3]

3.6.4 Boundary Conditions

Gas/gas boundaries are treated through an outflow or reflective model. The outflow model assumes that the flow is free to exit and there is no inflow. For instance, if the outflow boundary is located at $(x_{i+\frac{1}{2}}, y_j, z_k)$, the flux is the solution to the trivial Riemann problem given by:

$$U(x - x_{i+\frac{1}{2}}, y_j, z_k, t^n) = \begin{cases} U(x^-_{i+\frac{1}{2}}, y_j, z_k, t^n) & \text{if } x < x_{i+\frac{1}{2}} \\ U(x^-_{i+\frac{1}{2}}, y_j, z_k, t^n) & \text{if } x > x_{i+\frac{1}{2}} \end{cases} \tag{3.196}$$

The reflective model assumes that the flow cannot exit. This model is used for symmetric boundary conditions, as well as gas/solid and gas/liquid boundaries, when mass and heat transfer phenomena are neglected and the condensed phase is assumed to be perfectly rigid. If the reflective boundary is located at $(x_{i+\frac{1}{2}}, y_j, z_k)$, the flux at the boundary is the solution of

[3] A body force such as gravity can be treated to first order in a similar manner, in axially-symmetric cylindrical or Cartesian coordinates.

Test	ρ_l (kg m^{-3})	u_l (m s^{-1})	p_l (Pa)	ρ_r (kg m^{-3})	u_r (m s^{-1})	p_r (Pa)
1 [67]	1.0	0.0	1.0	0.125	0.0	0.1
2 [29]	1.0	-2.0	0.4	1.0	2.0	0.4
3 [75]	1.0	0.0	1000.0	1.0	0.0	0.01
4 [75]	1.0	0.0	0.01	1.0	0.0	100.0
5 [75]	5.99924	19.5975	460.894	5.99242	-6.19633	46.0950

Table 3.1: A few of the Riemann problems used as test cases.

the following Riemann problem:

$$U(x-x_{i+\frac{1}{2}},y_j,z_k,t^n) = \begin{cases} U(x^-_{i+\frac{1}{2}},y_j,z_k,t^n) & \text{if } x < x_{i+\frac{1}{2}} \\ \begin{pmatrix} \rho(x^-_{i+\frac{1}{2}},y_j,z_k,t^n) \\ \rho(x^-_{i+\frac{1}{2}},y_j,z_k,t^n)\omega_k(x^-_{i+\frac{1}{2}},y_j,z_k,t^n) \\ -\rho(x^-_{i+\frac{1}{2}},y_j,z_k,t^n)u(x^-_{i+\frac{1}{2}},y_j,z_k,t^n) \\ \rho(x^-_{i+\frac{1}{2}},y_j,z_k,t^n)v(x^-_{i+\frac{1}{2}},y_j,z_k,t^n) \\ \rho(x^-_{i+\frac{1}{2}},y_j,z_k,t^n)w(x^-_{i+\frac{1}{2}},y_j,z_k,t^n) \\ \rho(x^-_{i+\frac{1}{2}},y_j,z_k,t^n)e_t(x^-_{i+\frac{1}{2}},y_j,z_k,t^n) \end{pmatrix} & \text{if } x > x_{i+\frac{1}{2}} \end{cases} \tag{3.197}$$

Gas/liquid boundaries may be treated as reflective or through the model developed in Chapter 5.

3.7 Benchmarking

3.7.1 Riemann Solvers

A variety of Riemann problems were used to benchmark the ideal gas and real gas Riemann solvers. (Only the most significant cases are listed in Table 3.1. $\gamma = 1.4$ was used for these

test cases.)

1. Test case 1 is known as Sod's problem [67]. Its solution is made of a left rarefaction, a contact, and a right shock.

2. Test case 2 is an example of the symmetric two-rarefaction wave pattern that occurs, for instance, at reflective boundaries when the velocity is away from the boundary. Test case 2 is intended to illustrate the robustness of the exact Riemann solver when used to model a highly kinetic flow. (By highly kinetic it is meant that the ratio of kinetic to total energy is close to unity.) Einfeldt and co-workers [29] showed that some linearised Riemann solvers yield negative densities when applied to sufficiently kinetic flows. This is one of the primary reasons why an exact Riemann solver was implemented.

3. Test cases 3 and 4 are the left and right halves of Woodward and Colella's blast wave problem [75].

4. Test case 5 is the resulting wave from Woodward and Colella's blast wave problem [75], as reported by Toro [72].

Plots for test cases 1 through 5 are shown in Figures 3.1 through 3.5. The solutions from the Riemann solver are displayed with continuous lines.

3.7.2 Evolution-Reconstruction Schemes

One-Dimensional Test Cases

The Riemann problems used to benchmark the Riemann solvers are employed again to test the evolution-reconstruction schemes. Plots for test cases 1 through 5 are shown in Figures 3.1

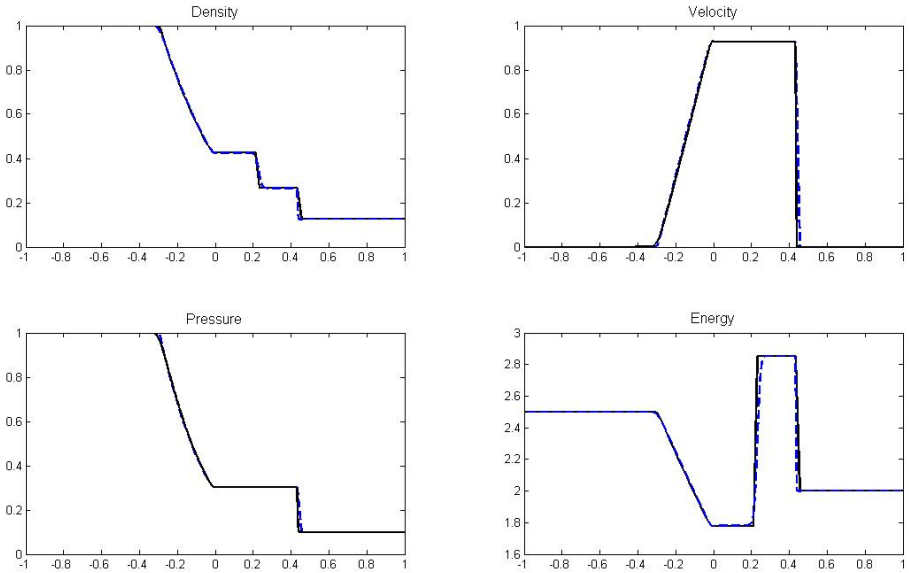

Figure 3.1: One-dimensional test case 1: density, velocity, pressure, specific energy.

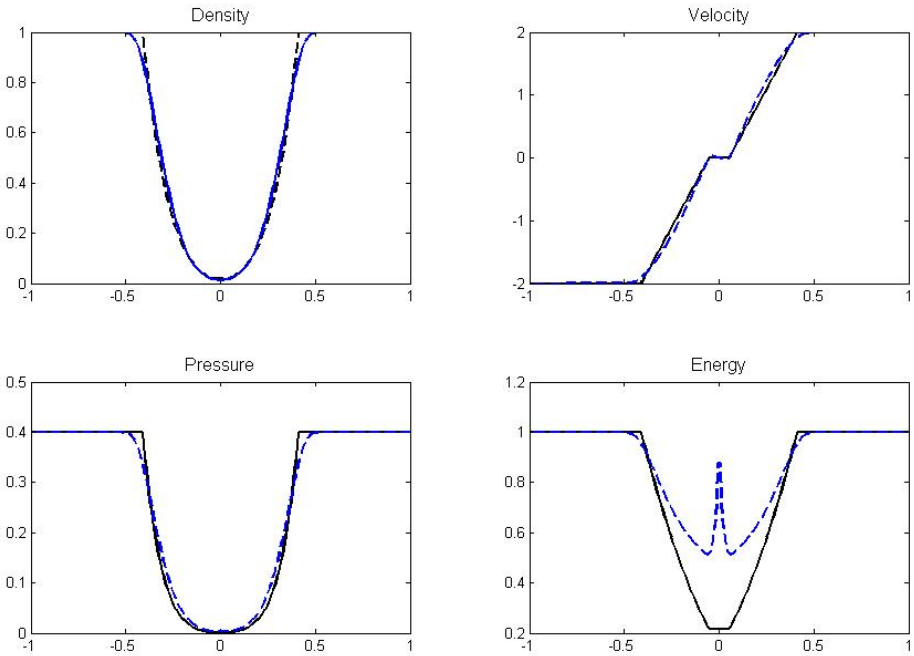

Figure 3.2: One-dimensional test case 2: density, velocity, pressure, specific energy.

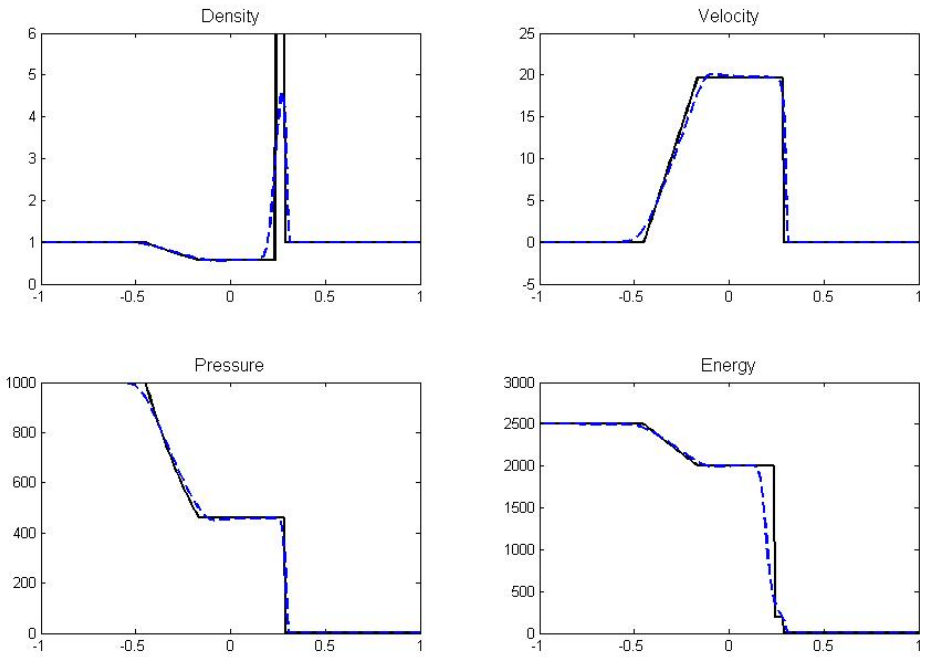

Figure 3.3: One-dimensional test case 3: density, velocity, pressure, specific energy.

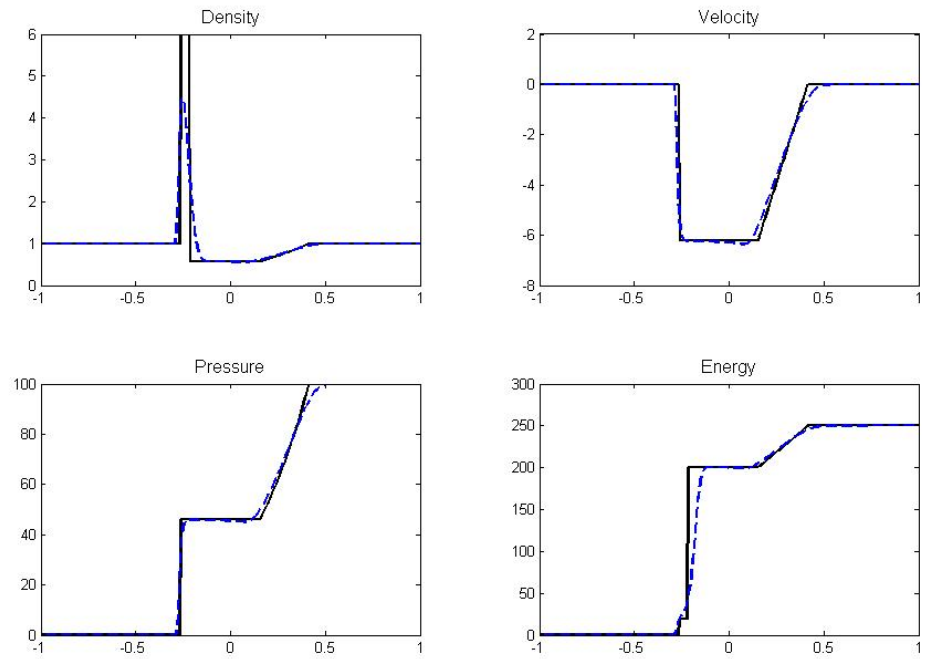

Figure 3.4: One-dimensional test case 4: density, velocity, pressure, specific energy.

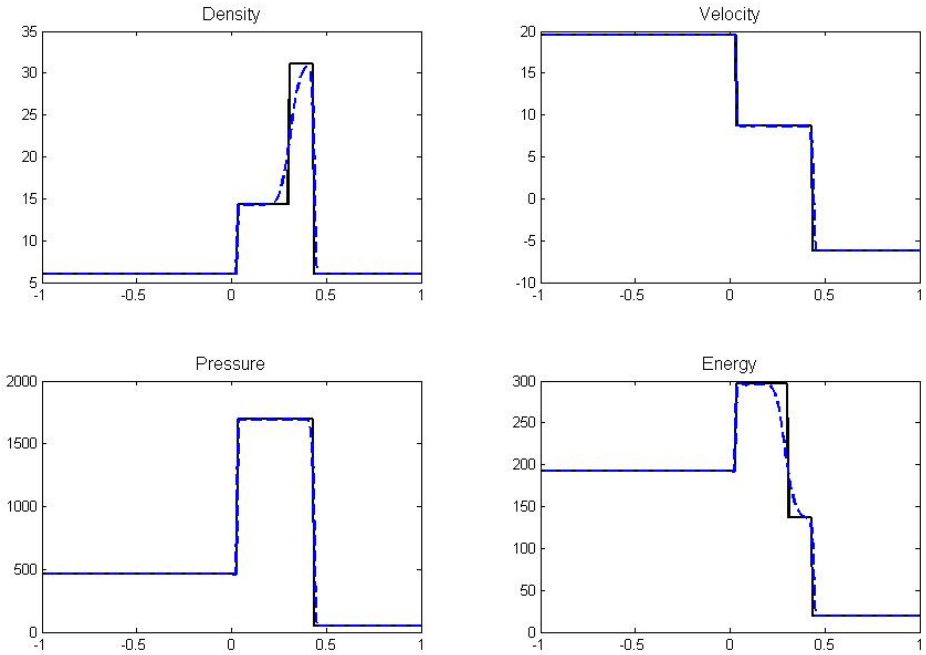

Figure 3.5: One-dimensional test case 5: density, velocity, pressure, specific energy.

through 3.5. The Godunov scheme solutions are displayed with discontinuous lines. A mesh of 300 cells, scaled from the coarsest Z-IFE simulation (to be described in Section 8.5), was employed. The error can be reduced by refining the mesh size, but is already sufficiently small for our purposes. The unphysical spike in the specific energy in Test case 2 is typical of reconstruction-evolution schemes in the low-density, highly kinetic regime.

Two-Dimensional Test Cases

As an illustration of the two-dimensional capability of the code, a set of two-dimensional, four-compartment Riemann problems were implemented. The particular example shown in Fig. 3.6 is our 2-D version of the 1-D test case 5. The mesh size is the one used for the 1-D problem, scaled from the coarsest Z-IFE simulation. Far from the center of the contour plot, one-dimensional Riemann problems are apparent along the horizontal and vertical axes, as

expected. In the center, a more complex 2-D pattern arises from the 2-D initial conditions.

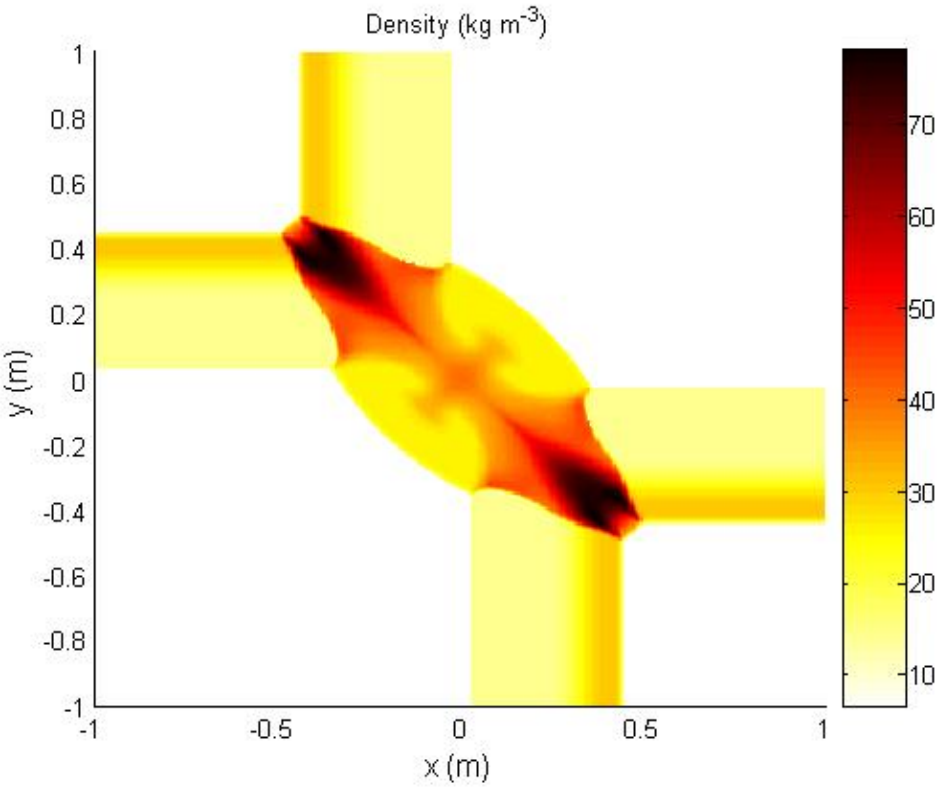

Figure 3.6: Two-dimensional test case 5: density.

Three-Dimensional Test Cases

The three-dimensional capability of Visual Tsunami was demonstrated with a set of three-dimensional Riemann problems. As an example, Fig. 3.7 shows a 3-D version of test case 1. In the planes shown in the figure, two-dimensional Riemann problems are apparent.

3.8 Conclusions and Perspectives

Exact Riemann solvers to the exact Riemann problems for ideal and real gases were implemented for the first time in a TSUNAMI code. A finite volume scheme was retained from

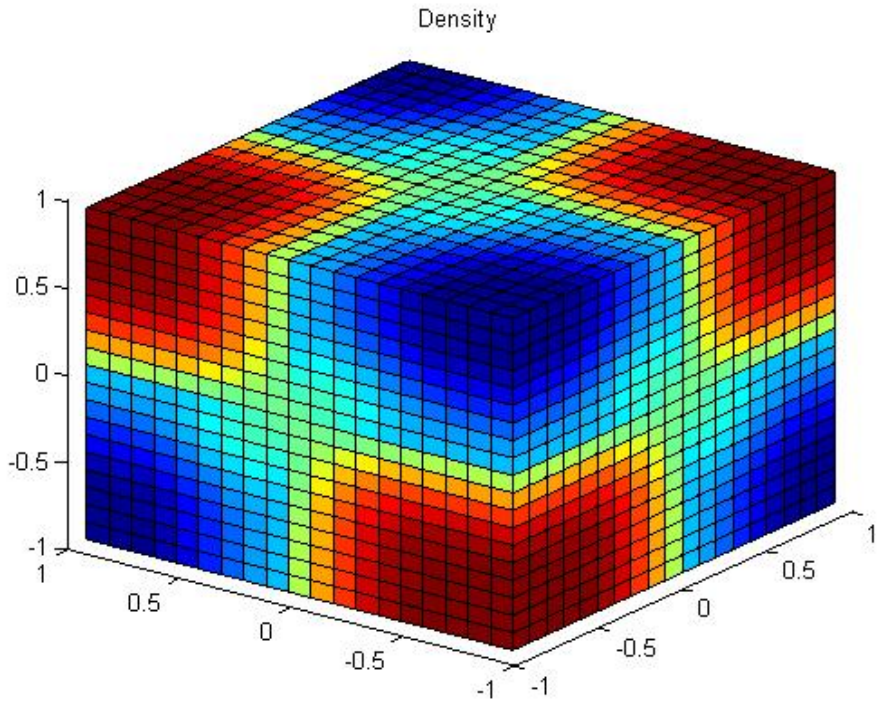

Figure 3.7: Three-dimensional test case 1: density.

previous versions in its most robust form. Future improvements could include higher-order reconstruction methods and unstructured meshes. The mesh size in Visual Tsunami simulations will likely be set by the necessity to resolve complex geometrical boundary conditions, not by the requirement for fine meshes imposed by first-order schemes. Numerical experiments reported in this section do indicate that the coarsest Z-IFE mesh can capture shock wave dynamics reasonably well and we therefore recommend implementing 2-D triangular and 3-D tetrahedral meshes prior to upgrading the code to a higher-order numerical scheme such as [73, 20]. (Unstructured meshes are particularly suited for simulations of complex geometries.) The gas dynamics code was designed and implemented to be easily ported to a distributed computing platform and finishing the implementation is encouraged. Substantial run time improvements are expected.

Chapter 4

Radiation Modeling

4.1 Introduction to Radiation Modeling

Detailed modeling of radiation interaction with matter is a daunting task, which is beyond current computing capability when performed in a multi-dimensional hydrodynamics design code. As a remedy, various approximate models can be used. However there is no *a priori* rigorous means of choosing the appropriate model for a given physical system. Choosing the best model for a given application is usually done empirically by implementing various models one at a time, from the simplest to the most elaborate. A typical case is run using each model and the error made with one model is assessed using the next, more accurate model. When the error seems to converge to zero, the last but one model can be used with some confidence. (Here a typical case would be a simulation of the target chamber and beam tubes. Examples of such simulations are presented in Chapter 8.)

Time-independent models represent the simplest class of approximate treatments of radiation transport. They include the most well-known cases, black and grey bodies for non-

participating media, as well as ray models for participating media. Black and grey bodies are inappropriate for gas dynamics calculations and cannot be applied for more than mere scoping analyses. Ray models are mono-directional and become invalid when the medium length is larger than several optical thicknesses. Jantzen [34] used such a model to estimate radiative heat losses from the target and ablated molten salt. Her approach was essentially one-dimensional. Each time step, heat losses by the spherical target, and independently, by the expanding ablated slabs of molten salt would be estimated. Geometry-wise, Jantzen's model may be justified for no more than the first few microseconds; at any rate, her approach lacks the generality expected for a versatile multi-dimensional radiation hydrodynamics code.

The simplest widely-used time-dependent model, the one-temperature diffusion model, also known as the conduction model, has been discarded since it is inadequate in optically "thin" regions where the density is low and the temperature high, resulting in large mean free paths. The next most commonly used model, two-temperature diffusion, is believed to yield the sought-after accuracy and has been retained. Radiation effects are expected to be secondary in a thick-liquid protected chamber, and, for time's sake, no attempt was made at benchmarking the approach against more elaborate models. (The average temperature of the ablated layers in the target chamber will be less than 100,000 K, a temperature too low for the radiation pressure to dominate its gas counterpart. Radiation may, however, play some role in a chamber in which the background vapor is dense enough to absorb some of the target x-rays.)

Chen [11] implemented such a two-temperature diffusion model into his 1-D version of TSUNAMI. The physical and mathematical models described here are close to Chen's, but the numerical scheme is expected to be significantly more accurate.

4.2 Physical Modeling: Flux-Limited Diffusion

The approach chosen in this section is purely intuitive. No formal derivation of the main differential equations will be given.

4.2.1 Differential Equations

The gas energy can be converted into radiation energy or can be transported away. The latter piece of physics is taken care of by the hydrodynamics model and thus only the former appears in the following gas energy balance equation:

$$\frac{\partial \rho e}{\partial t} = \frac{c}{\lambda_P}(E_r - aT^4) \tag{4.1}$$

where ρ is the gas density (kg m^{-3}), e the gas specific energy (J kg^{-1}), E_r the radiation energy density (J m^{-3}), and T the gas temperature (K). λ_P is the so-called Planck transport mean free path (m). c the speed of light in vacuum,[1] and a is given by:

$$a = \frac{4\sigma}{c} \tag{4.2}$$

σ is the Stefan-Boltzmann constant.[2] Intuitively, Eq. 4.1 means that if the radiation field temperature, $T_r = (\frac{E_r}{a})^{\frac{1}{4}}$, is greater than the gas temperature, T, then the gas will warm up and its energy per unit volume will increase.

The gas energy conservation equation can be simplified further through simple physical considerations. The effect of a volumetric energy change on the gas volume is not directly accounted for by the radiation scheme, but through the hydrodynamics model, according to which an increase in energy per unit volume will increase the gas pressure, which will in turn

[1] $c = 3.00 \times 10^8$ m s^{-1}

[2] $\sigma = 5.67 \times 10^{-8}$ W m^{-2} K^{-4}; $a = 7.56 \times 10^{-16}$J m^{-3} K^{-4}.

cause the gas to expand and its density to change. Here, radiation diffusion and exchange with the gas will not change the density of the gas:

$$\rho \frac{\partial e}{\partial t} = \frac{c}{\lambda_P}(E_r - aT^4) \tag{4.3}$$

and gas-radiation interactions are isochoric:

$$\frac{\partial V}{\partial t} = 0 \tag{4.4}$$

A little bit of thermodynamics is needed to relate a change in specific energy to a change in temperature:

$$\Delta e = \left.\frac{\partial e}{\partial T}\right|_V \Delta T + \left.\frac{\partial e}{\partial V}\right|_T \Delta V = c_v \Delta T + \left.\frac{\partial e}{\partial V}\right|_T \Delta V = c_v \Delta T \tag{4.5}$$

where c_v is the specific heat at constant volume (J K^{-1} kg^{-1}). The gas energy equation finally reads:

$$\rho \frac{\partial c_v T}{\partial t} = \frac{c}{\lambda_P}(E_r - aT^4) \tag{4.6}$$

Note that the numerical scheme makes use of Eq. 4.3 since $T = f(\rho, e)$ is more frequently available than $c_v = g(\rho, T)$.

The radiation energy can be diffused away or converted into gas energy. Mathematically, without any proof, this translates into:

$$\frac{\partial E_r}{\partial t} = \nabla \cdot (D \nabla E_r) - \frac{c}{\lambda_P}(E_r - aT^4) \tag{4.7}$$

where the only new variable is D, the radiation diffusion coefficient (m^2 s^{-1}).

In “thick” regions, where the radiation diffusion mean free path is much smaller than the typical length of the media, the diffusion coefficient, D_{thick}, is given by diffusion theory as:

$$D_{\text{thick}} = \frac{c\lambda_R}{3} \tag{4.8}$$

where λ_R is the so-called Rosseland diffusion mean free path (m).

In "thin" regions, the Rosseland diffusion mean free paths goes to infinity and Eq. 4.8 yields an unphysical diffusion coefficient. The effective diffusion coefficient, D_{thin}, should be in thin media:

$$D_{\text{thin}} = \frac{cE_r}{4\nabla E_r} \tag{4.9}$$

in order to recover the correct flux ($F = D\nabla E_r$) in non-participating media:

$$F_{\text{thin}} = \sigma T_r^4 = \frac{ca}{4} T_r^4 = \frac{c}{4} E_r \tag{4.10}$$

The so-called flux-limited diffusion coefficient, D, blends both thin and thick coefficients in an attempt at covering the full range of mean free paths:

$$D = f(D_{\text{thick}}, D_{\text{thin}}) \tag{4.11}$$

where f is a function *believed* to be appropriate. Among the wealth of possibilities available in the literature, a geometric mean was retained:

$$D = \frac{1}{\frac{1}{D_{\text{thin}}} + \frac{1}{D_{\text{thick}}}} = \frac{1}{\frac{1}{\frac{c\lambda_R}{3}} + \frac{1}{\frac{cE_r}{4\nabla E_r}}} \tag{4.12}$$

If the medium is optically thick, the Rosseland mean free path, λ_R, goes to 0 and Eq. 4.8 is recovered. Similarly, if the medium is optically thin, λ_R goes to ∞ and D is given by Eq. 4.9. Therefore the correct value of D will be used in the two limiting cases of optically thick and thin media. For finite mean free paths, on order of the typical length of the medium, it is common practice to *hope* that Eq. 4.12 yields a reasonably good effective diffusion coefficient. Exploring the sensitivity of the model to the choice of f could be valuable and is left for future work.

4.2.2 Initial and Boundary Conditions

The initial gas temperature distribution can usually be reasonably estimated in most cases, either through simple analytical or complex numerical models. For lack of a better model, local thermodynamics equilibrium may be assumed to prescribe the initial radiation energy density in Visual Tsunami simulations:

$$E_r = aT_r^4 = aT^4 \tag{4.13}$$

Cauchy boundary conditions are considered. The solid and liquid structures are assumed to be in local thermodynamics equilibrium and will radiate at their respective temperatures T, yielding the following Dirichlet boundary:

$$E_r = aT^4 \tag{4.14}$$

Neumann boundary conditions, with the energy density gradient set to zero, are used at symmetric and outflow gas boundaries. Implementation of more accurate boundary conditions is left for future work.

4.3 Numerical Model

4.3.1 Three-Dimensional Cartesian Coordinates

The gas and radiation transport equations, Eq. 4.3 and Eq. 4.7, now read:

$$\frac{\partial e}{\partial t} = \frac{c}{\rho \lambda_P}(E_r - aT^4) \tag{4.15}$$

and

$$\frac{\partial E_r}{\partial t} = \frac{\partial}{\partial x}\left(D\frac{\partial E_r}{\partial x}\right) + \frac{\partial}{\partial y}\left(D\frac{\partial E_r}{\partial y}\right) + \frac{\partial}{\partial z}\left(D\frac{\partial E_r}{\partial z}\right) - \frac{c}{\lambda_P}(E_r - aT^4) \tag{4.16}$$

This system is solved through the Adams-Bashforth-Moulton predictor-corrector scheme, as implemented in the MATLAB libraries. (This approach allows for an easy extension of the model to phenomena such as gas thermal heat conduction and viscous effects.) Time-stepping controls the accuracy of the time-integration. Details of the time integration are unnecessary for the present discussion and are omitted. Eq. 4.15 is trivially discretized in space as:[3]

$$\frac{\partial e_{i,j,k}}{\partial t} = \frac{c\left(E_{i,j,k} - a\left(T_{i,j,k}\right)^4\right)}{\rho_{i,j,k}\lambda_{i,j,k}} \tag{4.17}$$

where $T_{i,j,k} = f(\rho_{i,j,k}, e_{i,j,k})$ and $\lambda_{i,j,k} = g(\rho_{i,j,k}, T_{i,j,k})$. Eq. 4.16 is discretized in space as follows:

$$\begin{aligned}\frac{\partial E_{i,j,k}}{\partial t} = & \frac{D_{i+\frac{1}{2},j,k}\frac{E_{i+1,j,k}-E_{i,j,k}}{\frac{\Delta x_i+\Delta x_{i+1}}{2}} - D_{i-\frac{1}{2},j,k}\frac{E_{i,j,k}-E_{i-1,j,k}}{\frac{\Delta x_{i-1}+\Delta x_i}{2}}}{\Delta x_i} \\ & + \frac{D_{i,j+\frac{1}{2},k}\frac{E_{i,j+1,k}-E_{i,j,k}}{\frac{\Delta y_j+\Delta y_{j+1}}{2}} - D_{i,j-\frac{1}{2},k}\frac{E_{i,j,k}-E_{i,j-1,k}}{\frac{\Delta y_{j-1}+\Delta y_j}{2}}}{\Delta y_j} \\ & + \frac{D_{i,j,k+\frac{1}{2}}\frac{E_{i,j,k+1}-E_{i,j,k}}{\frac{\Delta z_k+\Delta z_{k+1}}{2}} - D_{i,j,k-\frac{1}{2}}\frac{E_{i,j,k}-E_{i,j,k-1}}{\frac{\Delta z_{k-1}+\Delta z_k}{2}}}{\Delta z_k} \\ & - \frac{c}{\lambda_{i,j,k}}\left(E_{i,j,k} - a\left(T_{i,j,k}\right)^4\right)\end{aligned} \tag{4.18}$$

Note that the non-linear dependence on the temperature is retained. (Most other diffusion schemes linearize the term with the fourth power of T.) In the flux-limited diffusion approximation used in this model, the diffusion coefficient D is computed as follows:

$$D_{i+\frac{1}{2},j,k} = \left(\frac{3}{c\lambda_{R,i+\frac{1}{2},j,k}} + \frac{\Delta E_{i+\frac{1}{2},j,k}}{F_{i+\frac{1}{2},j,k}}\right)^{-1} \tag{4.19}$$

where

$$\Delta E_{i+\frac{1}{2},j,k} = \frac{E_{i+1,j,k} - E_{i,j,k}}{\frac{\Delta x_i+\Delta x_{i+1}}{2}} \tag{4.20}$$

and

$$F_{i+\frac{1}{2},j,k} = \frac{c}{4}\frac{E_{i,j,k}+E_{i+1,j,k}}{2} = \frac{c}{8}(E_{i,j,k}+E_{i+1,j,k}) \tag{4.21}$$

[3]The subscripts r (radiation) and P (Planck) are dropped in all the discretized equations for clarity's sake.

boundary	location	material properties
Neumann	$(\frac{1}{2}, j, k)$	$E_{0,j,k} = E_{1,j,k}$ and $\rho_{0,j,k} = \rho_{1,j,k}$ and $e_{0,j,k} = e_{1,j,k}$
Neumann	$(I+\frac{1}{2}, j, k)$	$E_{I+1,j,k} = E_{I,j,k}$ and $\rho_{I+1,j,k} = \rho_{I,j,k}$ and $e_{I+1,j,k} = e_{I,j,k}$
Neumann	$(i, \frac{1}{2}, k)$	$E_{i,0,k} = E_{i,1,k}$ and $\rho_{i,0,k} = \rho_{i,1,k}$ and $e_{i,1,k} = e_{i,1,k}$
Neumann	$(i, J+\frac{1}{2}, k)$	$E_{i,J+1,k} = E_{i,J,k}$ and $\rho_{i,J+1,k} = \rho_{i,J,k}$ and $e_{i,J+1,k} = e_{i,J,k}$
Neumann	$(i, j, \frac{1}{2})$	$E_{i,j,0} = E_{i,j,1}$ and $\rho_{i,j,0} = \rho_{i,j,1}$ and $e_{i,j,0} = e_{i,j,1}$
Neumann	$(i, j, K+\frac{1}{2})$	$E_{i,j,K+1} = E_{i,j,K}$ and $\rho_{i,j,K+1} = \rho_{i,j,K}$ and $e_{i,j,K+1} = e_{i,j,K}$

Table 4.1: Radiation cells.

$\lambda_{R,i+\frac{1}{2},j,k}$ is evaluated using:

$$\lambda_{R,i+\frac{1}{2},j,k} = \frac{\lambda_{R,i,j,k} + \lambda_{R,i+1,j,k}}{2} \tag{4.22}$$

Additional equations are needed at reflective boundaries. All cases are presented in Table 4.1. For the radiation model, interior liquid and solid cells obey the following trivial equations:

$$\frac{\partial e}{\partial t} = 0 \tag{4.23}$$

and

$$\frac{\partial E_r}{\partial t} = 0 \tag{4.24}$$

(Changes in temperature are taken into account in Chapter 5.) The Rosseland and Planck mean free paths are computed using the Los Alamos National Laboratory code TOPS [35]. Reducing the numerical scheme to 1-D or 2-D is trivial.

4.3.2 Axially-Symmetric Cylindrical Coordinates

Only minor modifications are necessary to adapt the scheme to axially-symmetric cylindrical coordinates. Equations 4.3 and 4.17 remain unchanged, while the radiation diffusion

equation, Eq. 4.7, now reads:

$$\frac{\partial E_r}{\partial t} = \frac{1}{r}\frac{\partial}{\partial r}\left(rD\frac{\partial E_r}{\partial r}\right) + \frac{\partial}{\partial z}\left(D\frac{\partial E_r}{\partial z}\right) - \frac{c}{\lambda_P}(E_r - aT^4) \tag{4.25}$$

which leads to the following discretization in space:

$$\frac{\partial E_{i,j}}{\partial t} = \frac{1}{r_{i,j}}\frac{r_{i+\frac{1}{2},j}D_{i+\frac{1}{2},j}\frac{E_{i+1,j}-E_{i,j}}{\frac{\Delta r_i+\Delta r_{i+1}}{2}} - r_{i-\frac{1}{2},j}D_{i-\frac{1}{2},j}\frac{E_{i,j}-E_{i-1,j}}{\frac{\Delta r_{i-1}+\Delta r_i}{2}}}{\Delta r_i} + \frac{D_{i,j+\frac{1}{2}}\frac{E_{i,j+1}-E_{i,j}}{\frac{\Delta z_j+\Delta z_{j+1}}{2}} - D_{i,j-\frac{1}{2}}\frac{E_{i,j}-E_{i,j-1}}{\frac{\Delta z_{j-1}+\Delta_j}{2}}}{\Delta z_j} - \frac{c}{\lambda_{i,j}}\left(E_{i,j} - a\left(T_{i,j}\right)^4\right) \tag{4.26}$$

with the usual notations.

4.4 Conclusions and Perspectives

The two-temperature model coupled to the method of fractional steps was deemed suitable for the purposes of efficient computing and accurate modeling of thick-liquid protected target chambers. The radiation module still needs to be validated. In the near-term, various formulae for the diffusion coefficient and the boundary conditions could be explored and a numerical model compatible with unstructured meshes could be developed. As the level of sought-after accuracy is raised and other Visual Tsunami models are refined, the radiation model may have to be revised as well. A multi-group diffusion model or an unsplit radiation hydrodynamics model could be developed and implemented. (The current split implementation neglects the radiation pressure and energy compared to their gas dynamics counterparts.) As mentioned, the numerical model discussed in this chapter was chosen because it can easily be extended to include viscous and conductive effects, if necessary.

Chapter 5

Gas-Liquid Interface

5.1 Introduction

Ablation and target debris cause a rise in density and pressure in the fusion chamber. For the next target to be ignited, the initial background gas density needs to be restored. Thick-liquid protected chambers rely on condensation as their main clearing mechanism and modeling condensation phenomena is essential for high-fidelity simulations. Condensation will happen over tens of milliseconds; the model presented in this chapter is only meant to capture "early-time" condensation phenomena, which happen over the gas dynamics time scale.

The temperature of the surface of the liquid structures is a key parameter that needs to be known accurately to predict condensation and evaporation fluxes, for the mass and energy transfers are driven by the temperature difference at the gas-liquid interface. For early-time (sub-millisecond) simulations, the temperature distribution inside the liquid is necessary to assess secondary ablation—ablation caused by the hot gas in the target chamber, after the initial ablation induced by the burst of target x-rays. An accurate assessment of the mass and energy

fluxes up heavy-ion beam tubes requires some modeling of condensation and evaporation as well.

Two different conduction models were coded in three distinct versions of TSUNAMI. Liu [38] modeled condensation/evaporation phenomena and needed the temperature at the interface to determine the mass, momentum and energy fluxes. Jantzen [34] required the temperature field to model secondary ablation. Calderoni [8] implemented Liu's model into an early version of TSUNAMI 2.8. The heat transfer model presented in the following section captures the physics relevant to treat condensation and radiation simultaneously. The third section of this chapter focuses on a novel condensation/evaporation model that can be used at the gas/liquid interface.

5.2 Submillisecond Heat Transfer in Liquid Jets

5.2.1 Physical and Mathematical Models

Over the typical gas dynamics time scale, conduction is assumed to be the only mechanism by which heat is transported away from the surface into the liquid structures. (Typical time scales for internal convection and turbulent effects are substantially greater than simulation run times.) Consistently with the gas dynamics modeling, the liquid bulk velocity is assumed to be negligible compared to that of the gas, and the liquid structures are stationary. Moreover, secondary ablation will ablate thin layers of molten salt [11] and the gas/liquid interface will be treated as immobile. For the liquid structures, the equation of thermal energy then reads:[1]

$$\rho \frac{\partial e}{\partial t} = \nabla \cdot (k \nabla T) + q(x,y,z,t) \tag{5.1}$$

[1] No derivation of this equation is provided.

A local change in specific energy can be due to a volumetric heat source, q (W m^{-3}), or a heat flux, $k\nabla T$. ρ is the liquid density (kg m^{-3}) and k the liquid thermal conductivity (W m^{-1} K^{-1}).

The characteristic diffusion length is given by the product of the thermal diffusivity $\alpha = \frac{k}{\rho c_p}$ times the simulation run time to the one-half power. For liquid flibe or flinabe and a simulation time of 1 ms, the diffusion length is $\sqrt{\alpha t} \approx \sqrt{2 \times 10^{-7} \times 10^{-3}} \approx 10^{-5}$ m. In the target chamber, typical lengths are the height of the liquid jets (a few meters), the radius of curvature of the slab jets ($\approx \infty$) and the radius of curvature of the cylindrical jets (a few centimeters). In the beam tubes, the length of the vortex is a couple of meters and its radius of curvature a couple of centimeters. As x-ray deposition is essentially a one-dimensional process and the characteristic diffusion length is smaller than any of the typical physical lengths in the target chamber and the beam tubes, the heat conduction equation reduces to the following one-dimensional form in Cartesian coordinates:

$$\rho \frac{\partial e}{\partial t} = \frac{\partial}{\partial x}\left(k \frac{\partial T}{\partial x}\right) + q(x,t) \tag{5.2}$$

where x (m) is defined inward, from the surface location. (Note that the physics is one-dimensional in the local coordinate attached to the jet; the initial and boundary conditions do depend on the location in the target chamber.)

As presented in Chapter 6, radiation deposition is essentially a one-dimensional process assumed to follow an exponential law. The average gas temperature after the initial ablation will be of order of one eV. Since the average mean free path of a 1-eV photon in molten salts such as flibe and flinabe is practically null[2], the volumetric source term will be approximated

[2] A *100-eV* photon has a mean free path of order of a few microns in liquid flibe.

as a surface source term and Eq. 5.2 reads:[3]

$$\rho \frac{\partial e}{\partial t} = \frac{\partial}{\partial x}\left(k \frac{\partial T}{\partial x}\right) \tag{5.3}$$

At $x = 0$, the heat flux is then determined by the condensation and radiation models:

$$-k \frac{\partial T}{\partial x}\bigg|_{x=0} = J_e + J_{\text{radiation}} \tag{5.4}$$

where the radiation heat flux $J_{\text{radiation}}$ (W m^{-2}) was derived in the previous chapter and is given by $D\nabla E_r$ at the boundary. The hydrodynamics heat flux, J_e (W m^{-2}), is obtained in Section 5.4.

As mentioned, secondary radiation happens over very small distances. The amount of heat conducted at a depth x can be neglected, if $x \gg \delta_{\text{conduction}} \approx 10^{-5}$ m. Accordingly, at, say, $x = L = 10^{-3}$ m, the specific energy is set constant and keeps its initial value:

$$T(L,t) = T(L,0) \tag{5.5}$$

The initial temperature distribution $T(x,0)$ is given by the initial heating caused by target neutrons and x-rays.

5.2.2 Numerical Model

In the framework of his condensation/evaporation model, Liu [38] dealt with a heat conduction equation with constant physical properties; he chose an explicit scheme to discretize it. This imposed a very constraining stability condition. Jantzen [34] used an implicit Crank-Nicolson finite difference scheme. A common approximation underlying their numerical schemes replaces e by $c_p T$ in Eq. 5.3; c_p is the heat capacity at constant pressure and is then

[3] Jantzen [34] used a volumetric source term, without any justification.

assumed to be constant for convenience. This approximation is usually fairly good but does not apply here since the "liquid" structure is actually a two-phase mixture near the interface. (The mixture is creature by the initial ablation described in Chapter 6.)

Here, Eq. 5.3 is directly solved with an Adams-Bashforth-Moulton predictor-corrector method. The details of the time evolution are implemented in the MATLAB library, and only the space discretization is presented here:

$$\rho \frac{\partial e(x_i, t^n)}{\partial t} = \frac{\partial}{\partial x}\left(k(T_i^n)\frac{\partial T_i^n}{\partial x}\right) \tag{5.6}$$

A centered scheme is used for the interior nodes:

$$\frac{\partial}{\partial x}\left(k(T_i^n)\frac{\partial T_i^n}{\partial x}\right) = \frac{k^n_{i-\frac{1}{2}} T^n_{i-1} - \left(k^n_{i-\frac{1}{2}} + k^n_{i+\frac{1}{2}}\right) T_i^n + k^n_{i+\frac{1}{2}} T^n_{i+1}}{(\Delta x)^2} \tag{5.7}$$

where

$$k^n_{i+\frac{1}{2}} = \frac{k_i^n + k_{i+1}^n}{2} \tag{5.8}$$

At the boundaries, it is assumed that:

$$\frac{\partial}{\partial x}\left(k(T_I^n)\frac{\partial T_I^n}{\partial x}\right) = 0 \tag{5.9}$$

and

$$\frac{\partial}{\partial x}\left(k(T_1^n)\frac{\partial T_1^n}{\partial x}\right) = \frac{\frac{k^n_{\frac{3}{2}}\left(T_2^n - T_1^n\right)}{\Delta x} - \left(J_e^n + J^n_{\text{radiation}}\right)}{\Delta x} \tag{5.10}$$

where J_e^n and $J^n_{\text{radiation}}$ are the energy and radiation fluxes at $t = t^n$. As usual, $T_i^n = f(\rho_i^n, e_i^n)$ is provided by the caloric equation of state.

5.3 Benchmarking

The code can be tested with a well-known analytical solution to a simplified form of Eq. 5.3 with $e = c_p T$ where T is the temperature and c_p is the heat capacity at constant pressure, which

is assumed to be constant. For a semi-infinite slab with initial conditions

$$T(x,0) = 0 \tag{5.11}$$

and left boundary condition

$$f = -k\frac{\partial T}{\partial x} = f_0 = \text{constant} \tag{5.12}$$

the solution reads:

$$T(x,t) = \frac{2f_0}{k}\left(\sqrt{\frac{\alpha t}{\pi}}\exp\left(-\frac{x^2}{4\alpha t}\right) - \frac{x}{2}\text{erfc}\left(\frac{x}{2\sqrt{\alpha t}}\right)\right) \tag{5.13}$$

5.4 A Novel Gas-Liquid Interface Model

Mass transfer at the interface between a gas and a liquid has been widely studied. The most famous contribution may be found in Schrage's doctoral dissertation, subsequently published in [61]. His assumptions have been progressively challenged and more refined results have been obtained through Monte-Carlo simulations. A Monte-Carlo model could be incorporated into Visual Tsunami; however, Visual Tsunami is meant to be a design code, and, as such, the typical run time should remain reasonable. A fancy Monte-Carlo model is deemed too CPU-intensive. Analytical models, albeit more approximate, are preferred. Transfers of momentum and energy have not been studied as thoroughly and no simple, explicit analytical formula is known to the author. A new model has therefore been developed for this doctoral work, based on Schrage's well-understood assumptions.

Schrage's approach relies on two major assumptions, bold and unjustified, but very practical and convenient:

1. Condensation and evaporation partial fluxes can be computed separately and added algebraically to give the net transfer fluxes;

2. Gas molecules obey a Maxwellian distribution at the gas/liquid interface.

The following analysis is presented for a planar interface located at $x = 0$, with the gas phase occupying the half-space $x > 0$.

5.4.1 Interface Mass Transfer

The impacting, condensing, rebounding and evaporating fluxes are respectively noted J_i, J_c, J_r, and J_e (kg s^{-1} m^{-2}).

Evaporating flux

According to Schrage's second assumption, evaporating molecules follow the canonical Maxwellian distribution. It is further assumed that the bulk of the fluid is assumed to be at rest:

$$f(u,v,w) = n_f \frac{\beta_f^3}{\pi^{\frac{3}{2}}} \exp\left(-\beta_f^2\left(u^2+v^2+w^2\right)\right) \tag{5.14}$$

where n_f is the density (m^{-3}) of liquid molecules. u, v, and w are the velocity components (m s^{-1}) and β_f is given by:

$$\beta_f = \sqrt{\frac{M}{2RT}} \tag{5.15}$$

where M is the molar mass (kg mol^{-1}), R the universal gas constant[4], and T is the temperature (K). The evaporating mass flux, J_e, is given by:

$$J_e = \int_0^\infty du \int_{-\infty}^\infty dv \int_{-\infty}^\infty mu f(u,v,w)\, dw \tag{5.16}$$

Substituting for f using Eq. 5.14 and noticing that $\rho = nm$ yield:

$$J_e = \rho_f \frac{\beta_f^3}{\pi^{\frac{3}{2}}} \int_0^\infty du \int_{-\infty}^\infty dv \int_{-\infty}^\infty u \exp\left(-\beta_f^2\left(u^2+v^2+w^2\right)\right) dw \tag{5.17}$$

[4]R=8.31 J mol^{-1} K^{-1}

By Fumini's theorem,

$$J_e = \rho_f \frac{\beta_f^3}{\pi^{\frac{3}{2}}} \left(\int_0^\infty u \exp\left(-\beta_f^2 u^2\right) du \right) \left(\int_{-\infty}^\infty \exp\left(-\beta_f^2 v^2\right) dv \right) \left(\int_{-\infty}^\infty \exp\left(-\beta_f^2 w^2\right) dw \right) \tag{5.18}$$

Evaluating the three integrals gives:

$$J_e = \rho_f \frac{\beta_f^3}{\pi^{\frac{3}{2}}} \left(\frac{1}{2\beta_f^2} \right) \left(\frac{\pi^{\frac{1}{2}}}{\beta_f} \right) \left(\frac{\pi^{\frac{1}{2}}}{\beta_f} \right) \tag{5.19}$$

Collecting,

$$J_e = \frac{\rho_f}{2\pi^{\frac{1}{2}} \beta_f} \tag{5.20}$$

Using Eq. 5.15 yields:

$$J_e = \rho_f \sqrt{\frac{RT_f}{2\pi M}} \tag{5.21}$$

Inserting the ideal gas law, the following well-known formula is obtained:

$$J_e = p_f \sqrt{\frac{M}{2\pi R T_f}} \tag{5.22}$$

Impacting flux

For the gas, Schrage assumed a skewed Maxwellian distribution. The fluid moves perpendiculary to the surface at a bulk speed u_g:

$$f(u,v,w) = n_g \frac{\beta_g^3}{\pi^{\frac{3}{2}}} \exp\left(-\beta_g^2 \left((u-u_g)^2 + v^2 + w^2 \right) \right) \tag{5.23}$$

The impacting mass flux, J_i, is given by

$$J_i = \int_{-\infty}^0 du \int_{-\infty}^\infty dv \int_{-\infty}^\infty mu f(u-u_g, v, w)\, dw \tag{5.24}$$

$$= \rho_g \frac{\beta_g^3}{\pi^{\frac{3}{2}}} \int_{-\infty}^0 du \int_{-\infty}^\infty dv \int_{-\infty}^\infty u \exp\left(-\beta_g^2 \left((u-u_g)^2 + v^2 + w^2 \right) \right) dw \tag{5.25}$$

$$= \rho_g \frac{\beta_g^3}{\pi^{\frac{3}{2}}} \left(\frac{\pi^{\frac{1}{2}} u_g}{2\beta_g} \left(1 - \operatorname{erf}(\beta_g u_g)\right) - \frac{1}{2\beta_g^2} \exp\left(-\beta_g^2 u_g^2\right) \right) \left(\frac{\pi^{\frac{1}{2}}}{\beta_g} \right) \left(\frac{\pi^{\frac{1}{2}}}{\beta_g} \right) \tag{5.26}$$

$$= \frac{\rho_g}{2\pi^{\frac{1}{2}} \beta_g} \left(\pi^{\frac{1}{2}} u_g \beta_g \left(1 - \operatorname{erf}(\beta_g u_g)\right) - \exp\left(-\beta_g^2 u_g^2\right) \right) \tag{5.27}$$

If the particular case that $u_g = 0$, Eq. 5.27 reduces to:

$$J_i = -\frac{\rho_g}{2\pi^{\frac{1}{2}}\beta_g} \tag{5.28}$$

as expected from Eq. 5.20.

Net Mass Flux

Following Schrage's first assumption, the net mass flux, $J_{\text{mass}}^{\text{kinetics}}$, is given by

$$J_{\text{mass}}^{\text{kinetics}} = J_e - J_c \tag{5.29}$$

Equivalently, the net mass flux can be obtained through

$$J_{\text{mass}}^{\text{kinetics}} = J_e - \sigma_c J_i \tag{5.30}$$

where the accommodation coefficient, σ_c, is by definition the ratio of the condensing flux to the impacting flux. The evaporating and impacting fluxes are given by Equations 5.21 and 5.27, respectively. No satisfying theory has been found to evaluate σ_c accurately and effectively. The accomodation coefficient is assumed to be unity in the remainder of the chapter. Schrage's first approximation fails for very intense condensation and evaporation: a fraction of the evaporating molecules may collide and re-condense. Schrage focused on mass transfer; the next two subsections present the first application of his methodology to momentum or energy transfer known to the author.

5.4.2 Interface Momentum Transfer

For the momentum transfer, Schrage's two main assumptions are retained. The evaporating and impacting/condensing fluxes are computed separately and Maxwellian distributions are assumed.

Evaporating Flux

The evaporating momentum flux is given by:

$$J_e = \int_0^\infty du \int_{-\infty}^\infty dv \int_{-\infty}^\infty mu^2 f(u,v,w)\, dw \tag{5.31}$$

$$= \rho_f \frac{\beta_f^3}{\pi^{\frac{3}{2}}} \int_0^\infty du \int_{-\infty}^\infty dv \int_{-\infty}^\infty u^2 \exp\left(-\beta_f^2\left(u^2+v^2+w^2\right)\right) dw \tag{5.32}$$

$$= \rho_f \frac{\beta_f^3}{\pi^{\frac{3}{2}}} \int_0^\infty u^2 \exp\left(-\beta_f^2 u^2\right) du \int_{-\infty}^\infty \exp\left(-\beta_f^2 v^2\right) dv \int_{-\infty}^\infty \exp\left(-\beta_f^2 w^2\right) dw \tag{5.33}$$

$$= \rho_f \frac{\beta_f^3}{\pi^{\frac{3}{2}}} \left(\frac{\pi^{\frac{1}{2}}}{4\beta_f^3}\right)\left(\frac{\pi^{\frac{1}{2}}}{\beta_f}\right)\left(\frac{\pi^{\frac{1}{2}}}{\beta_f}\right) \tag{5.34}$$

$$= \frac{\rho_f}{4\beta_f^2} \tag{5.35}$$

Impacting Flux

The impacting momentum flux follows from:

$$J_i = \int_{-\infty}^0 du \int_{-\infty}^\infty dv \int_{-\infty}^\infty mu^2 f(u-u_g,v,w)\, dw \tag{5.36}$$

$$= \rho_g \frac{\beta_g^3}{\pi^{\frac{3}{2}}} \int_{-\infty}^0 du \int_{-\infty}^\infty dv \int_{-\infty}^\infty u^2 \exp\left(-\beta_g^2\left((u-u_g)^2+v^2+w^2\right)\right) dw \tag{5.37}$$

$$= \rho_g \frac{\beta_g^3}{\pi^{\frac{3}{2}}} \left(\frac{\pi^{\frac{1}{2}}\left(1+2\beta_g^2u_g^2\right)\left(1-\operatorname{erf}(\beta_g u_g)\right)}{4\beta_g^3} - \frac{u_g \exp\left(-\beta_g^2 u_g^2\right)}{2\beta_g^2}\right)\left(\frac{\pi^{\frac{1}{2}}}{\beta_f}\right)\left(\frac{\pi^{\frac{1}{2}}}{\beta_f}\right) \tag{5.38}$$

$$= \frac{\rho_g}{4\pi^{\frac{1}{2}}\beta_g^2}\left(\pi^{\frac{1}{2}}\left(1+2\beta_g^2u_g^2\right)\left(1-\operatorname{erf}(\beta_g u_g)\right) - 2\beta_g u_g \exp\left(-\beta_g^2 u_g^2\right)\right) \tag{5.39}$$

If $u_g = 0$, Eq. 5.39 reduces to

$$J_i = \frac{\rho_g}{4\beta_g^2} \tag{5.40}$$

as expected from Eq. 5.35.

Net Momentum Flux

The net momentum flux is then:

$$J_{\text{momentum}}^{\text{kinetics}} = J_e - J_i \tag{5.41}$$

where J_e and J_i are given by Equations 5.35 and 5.39, respectively.

5.4.3 Interface Heat Transfer

The energy evaporating and impacting fluxes are computed separately and Maxwellian distributions are used.

Evaporating Flux

The evaporating energy flux is given by:

$$J_e = \int_0^\infty du \int_{-\infty}^\infty dv \int_{-\infty}^\infty \frac{1}{2} mu(u^2+v^2+w^2) f(u,v,w)\, dw \tag{5.42}$$

$$= \rho_f \frac{\beta_f^3}{\pi^{\frac{3}{2}}} \int_0^\infty du \int_{-\infty}^\infty dv \int_{-\infty}^\infty \frac{1}{2} u(u^2+v^2+w^2) \exp(-\beta_f^2(u^2+v^2+w^2))\, dw \tag{5.43}$$

$$= \rho_f \frac{\beta_f^3}{\pi^{\frac{3}{2}}} \frac{\pi}{2\beta_f^6} \tag{5.44}$$

$$= \frac{\rho_f}{2\pi^{\frac{1}{2}}\beta_f^3} \tag{5.45}$$

Impacting Flux

The impacting energy flux comes from:

$$J_i = \int_{-\infty}^{0} du \int_{-\infty}^{\infty} dv \int_{-\infty}^{\infty} mu\frac{1}{2}(u^2+v^2+w^2)\, f(u-u_g,v,w)\, dw \tag{5.46}$$

$$= \rho_g \frac{\beta_g^3}{\pi^{\frac{3}{2}}} \int_{-\infty}^{0} du \int_{-\infty}^{\infty} dv \int_{-\infty}^{\infty} u\frac{1}{2}\left(u^2+v^2+w^2\right) \exp\left(-\beta_g^2\left((u-u_g)^2+v^2+w^2\right)\right) dw \tag{5.47}$$

$$= \frac{\rho_g}{8\pi^{\frac{1}{2}}\beta_g^3}\left(\pi^{\frac{1}{2}}\beta_g u_g\left(5+2u_g^2\beta_g^2-(5+2\beta_g^2u_g^2)\mathrm{erf}(\beta_g u_g)\right)-(4+2\beta_g^2u_g^2)\exp(-\beta^2u_g^2)\right) \tag{5.48}$$

which reduces to

$$J_i = -\frac{\rho_g}{2\pi^{\frac{1}{2}}\beta_g^3} \tag{5.49}$$

if $u_g = 0$, as expected from Eq. 5.45.

Net Energy Flux

The net heat flux is then:

$$J_{\text{energy}}^{\text{kinetics}} = J_e - J_i \tag{5.50}$$

where J_e and J_i are given by Equations 5.45 and 5.48, respectively.

5.4.4 Choking Considerations

Schrage's simple treatment predicts unbounded mass fluxes. For high pressures and low temperatures, J_t goes to infinity. As pointed out by Schrock and co-workers [62], a phenomenon similar to nozzle flow choking can occur during intensive condensation and the kinetic mass flux should be limited by the maximum flux allowed by gas dynamics. The equations are not repeated here.

5.5 Conclusions and Perspectives

The liquid heat conduction model allows for an accurate representation of heat transfer through the two-phase and liquid regions of the jets. Future models could take into account the actual dynamics of this two-phase region and the formation of liquid droplets. The gas/liquid interface model presented here follows Schrage's mass transfer assumptions. It still needs to be tested against more elaborate models in order to assess the error. This is left for future work.

The difference of volatibility between the different flibe and flinabe molecules is believed to be of very little importance during the early phase of gas dynamics and condensation. Non-condensibles are pumped out, and very little should be present in the target chamber and beam tubes at any time. Hence, neither non-condensibles nor the difference of volatibility between the various molecules were modeled. However, in order to model gas dynamics phenomena over longer time scales, multi-species effects will have to be appropriately modeled.

Chapter 6

Target and Ablation Modeling

6.1 Introduction

Neutrons and photons constitute the two major threats to the target chamber. Most of the neutrons and x-rays emitted by the target and hohlraum debris will be absorbed in the surrounding liquid and solid structures. The typical mean free path for a fusion neutron, about 7 cm in the molten salt flibe, is somewhat larger than the typical dimension of the jets, which is a few centimeters or so. Neutron deposition in the jets will therefore result in a somewhat flat energy profile and a rather uniform increase in the temperature of each jet. The typical x-ray mean free path in flibe and flinabe, on the order of tens of microns, is small compared to the dimensions of the liquid jets and most of the x-ray energy will be deposited in a small layer near the surface of the jets. The energy deposited in the jets is substantial and sufficient to induce partial vaporization of the layers in which x-rays are absorbed. This phenomenon—vaporization due to radiation emitted by target debris—is known as “ablation.” Some more vaporization will be induced by the energy radiated by the hot gas expanding in the target

chamber and beam tubes. This is sometimes called “secondary radiation and ablation” and was treated in Chapters 4 and 5. Target and hohlraum debris will carry a small fraction of the target yield and most of its energy will be deposited in the ablated layer. Helium ions are mostly stopped inside the target and the hohlraum and are usually included in the target and hohlraum debris bookkeeping.

6.2 Target Modeling

A detailed modeling of target and ablation related phenomena is outside of the scope of this doctoral dissertation; the target threat modeling discussed is this section is only meant to provide the initial conditions for the radiation hydrodynamics schemes described in Chapters 3 and 4. Gas dynamics phenomena typically happen over tens to hundreds of microseconds and are rather insensitive to the details of the target and holhraum disassembly and x-ray interaction with matter, which happen over hundreds of nanoseconds.

6.2.1 Neutrons

Neutron energy deposition in liquid and solid structures is not directly modeled by Visual Tsunami but can be taken into account reasonably well through an appropriate initial temperature field. Neutron energy deposition over small time scales causes isochoric heating of the liquid and solid structures. Their mechanical response is not modeled by Visual Tsunami, but could be included.

6.2.2 Target and Hohlraum Remnants

Target and hohlraum debris tend to be loosely described as slow and fast ions. Slow ions travel as a continuum and are modeled with the equations and schemes described in Chapters 4 and 5. Fast ions travel ballistically. For indirect drive targets, fast ions carry about 2% of the target yield; a simple model is expected to be sufficient for our purposes. Fast ions are assumed to stop in the ablated layers, where they deposit their energies. Their mass and energy are simply added to the mass and energy of the ablated layers, as determined in this chapter.

6.2.3 X-Rays

A direct-drive target emits a couple of percents of its energy as x-rays while indirect-drive target debris hits the hohlraum and radiates significantly—about 25% of the target yield. The fluence, Φ (J m^{-2}), impinging on a surface is by definition:

$$\Phi = \text{target yield} \times \text{fraction of target yield carried by x-rays} \times \frac{\cos(\theta)}{4\pi r^2} \tag{6.1}$$

where r is the distance (m) between the liquid surface and the target and θ (rad) is the angle between the normal to the irradiated surface and the line-of-sight to the target. Fusion target spectral emissivities (J m^{-2} sr^{-1}) have usually been approximated as a blackbody:

$$J_{\text{target}}(\nu) = B(\nu) = \frac{\frac{2h\nu^3}{c^2}}{e^{\frac{h\nu}{kT}} - 1} \tag{6.2}$$

or a sum of three blackbodies:

$$J_{\text{target}}(\nu) = \omega_1 \frac{\frac{2h\nu^3}{c^2}}{e^{\frac{h\nu}{kT_1}} - 1} + \omega_2 \frac{\frac{2h\nu^3}{c^2}}{e^{\frac{h\nu}{kT_2}} - 1} + \omega_3 \frac{\frac{2h\nu^3}{c^2}}{e^{\frac{h\nu}{kT_3}} - 1} \tag{6.3}$$

B is the spectral emittance of a blackbody and has units of J m^{-2} sr^{-1}. ν is the photon frequency (Hz); c is the speed of light in vacuum[1]; h is Planck's constant[2]; k is Boltzmann's

[1] $c = 3.00 \times 10^8$ m s^{-1}
[2] $h = 6.63 \times 10^{-34}$ J s

constant[3]. Eq. 6.2 is known as the Planck law. Note that the weights are dimensionless and can be functions of time.

6.3 Initial Ablation Modeling

6.3.1 Energy Deposition: An Improved TSUNAMI Model

Over the short time scales of the target x-ray pulse, the mechanical response of the material (its motion) is deemed unimportant and the energy of the irradiated material can only vary due to photon energy absorption, and, posssibly, re-radiation and electronic heat conduction. The heat conduction and exchange terms are given by Equations 4.7 and 4.8:

$$\nabla \cdot (D\nabla E_r) - \frac{c}{\lambda_P}\left(E_r - aT^4\right) = \nabla \cdot \left(\frac{c\lambda_R}{3}\nabla E_r\right) - \frac{c}{\lambda_P}\left(E_r - aT^4\right) \tag{6.4}$$

As usual, λ_R is the Rosseland mean free path (m). It is further assumed that thermal equilibrium enforces $E_r = aT^4$. Hence,

$$\nabla \cdot (D\nabla E_r) - \frac{c}{\lambda_P}\left(E_r - aT^4\right) = \nabla \cdot \left(\frac{c\lambda_R}{3}\nabla aT^4\right) = \nabla \cdot \left(\frac{4ac\lambda_R}{3}T^3\nabla T\right) \tag{6.5}$$

which can be simplified somewhat using the definition of $a = \frac{4\sigma}{c}$

$$\nabla \cdot (D\nabla E_r) - \frac{c}{\lambda_P}\left(E_r - aT^4\right) = \frac{16\sigma}{3}\nabla \cdot \left(\lambda_R T^3 \nabla T\right) \tag{6.6}$$

Taking into account photon energy absorption, re-radiation, and electronic heat conduction, conservation of the total energy per unit volume (J m^{-3}) $E = E_r + \rho e$ translates into:

$$\frac{\partial E}{\partial t} = \nabla \cdot (k_{\text{eff}}(T)\nabla T) + \int_0^\infty 4\pi\mu_0(\nu, T)I(\nu, t)\,d\nu \tag{6.7}$$

[3] $k = 1.38 \times 10^{-23}$ J K^{-1}

where μ_0 is the linear attenuation coefficient (m^{-1}) and k_{eff} ($\mathrm{W\ m^{-1}\ K^{-1}}$) is the "effective" conductivity, which is the sum of the electronic and radiative conductivities:

$$k_{\mathrm{eff}}(T) = k_{\mathrm{electronic}} + \frac{16}{3}\sigma\lambda_R(T)T^3 \tag{6.8}$$

Following the discussion in Chapter 5, the energy balance equation is solved in one dimension:

$$\frac{\partial E}{\partial t} = \frac{\partial}{\partial x}\left(k_{\mathrm{eff}}(T)\frac{\partial T}{\partial x}\right) + \int_0^\infty 4\pi\mu_0(\nu,T)I(\nu,t)\,d\nu \tag{6.9}$$

The total energy density E, the material specific energy e, and the material temperature T are assumed to be related by the following equation of state:

$$E = \rho e + aT^4(\rho,e) \tag{6.10}$$

where T is given as a function of ρ and e by the caloric equation of state. Along the mean path of the photons, the spectral intensity equation reads in the quasi-equilibrium approximation:

$$\frac{\partial I(\nu)}{\partial s} = -\mu_0(\nu)I(\nu) \tag{6.11}$$

or, in the local coordinate system perpendicular to the ablated surface:

$$\frac{\partial I(\nu)}{\partial x} = -\frac{\mu_0(\nu)I(\nu)}{\cos(\theta)} \tag{6.12}$$

This is known as the Beer-Lambert law. The $\cos(\theta)$ term has the practical effect to reduce the "apparent" mean free path of the photons, the inverse of the linear attenuation coefficient. The boundary condition at the surface is assumed to be given by:

$$I(\nu,t) = \frac{J_{\mathrm{target}}(\nu,t)}{\int_0^\infty J_{\mathrm{target}}(\nu,t)\,d\nu}\frac{\phi(t)}{4\pi} \tag{6.13}$$

where ϕ is the energy flux at the surface and is related to the fluence by:

$$\Phi = \int_{\Delta t}\phi(t)\,dt \tag{6.14}$$

(Δt is the total duration of the x-ray pulse.) I is therefore given by:

$$I(\nu,t) = \frac{\phi(t)}{4\pi} \frac{J_{\text{target}}(\nu,t)}{\int_0^\infty J_{\text{target}}(\nu,t)\,d\nu} \exp\left(-\frac{\mu_0 x}{\cos(\theta)}\right) \tag{6.15}$$

For a mono-energetic x-ray and an instantaneous energy deposition, the previous equation reads

$$I = \frac{\phi}{4\pi} \exp\left(-\frac{\mu_0 x}{\cos(\theta)}\right) \tag{6.16}$$

The energy conservation equation then reads:

$$\frac{\partial E}{\partial t} = 4\pi\mu_0 I = \mu_0 \phi \exp\left(-\frac{\mu_0 x}{\cos(\theta)}\right) \tag{6.17}$$

The instantaneous model is appropriate for relatively small increases in temperature (and short pulse duration.) Hence,

$$\rho \frac{\partial e}{\partial t} = \mu_0 \phi \exp\left(-\frac{\mu_0 x}{\cos(\theta)}\right) \tag{6.18}$$

Finally, the increase in specific energy is given by

$$\Delta e(x) = \frac{\mu_0}{\rho} \Phi \exp\left(-\frac{\mu_0 x}{\cos(\theta)}\right) = \mu \Phi \exp\left(-\frac{\mu_0 x}{\cos(\theta)}\right) \tag{6.19}$$

where $\mu = \frac{\mu_0}{\rho}$ is the mass attenuation coefficient.

The mass attenuation coefficients mainly depend on the photon energy, the composition of the medium, and its temperature. The temperature dependence of the mass attenuation coefficients mainly comes into play through the photoelectric effect, which is the primary interaction mechanism at the range of x-ray energies of interest. “Cold” opacities (as function of photon energy and medium composition) can be looked up in various references available in the literature or evaluated using one of several computer codes. Visual Tsunami makes use of tabulated absorption coefficients extracted from the Lawrence Livermore National Laboratory

(LLNL) cross-section library known as EPDL97 [22]. The LLNL code EPICSHOW [21] can be used to format and plot the data from EPDL97.[4]

"Cold" opacities are valid for low fluences, when the temperature of the ablated layer does not increase significantly. If the fluence is high enough, the temperature of the ablated medium can be such that significant ionization occurs, to the point that fewer photoelectric interactions are possible; the medium becomes transparent to the target photons. (This is called bleaching.) Chen [11] assumed arbitrarily in his instantaneous energy deposition model that the "hot" mean free path of the photons was on average twice as long as the "cold" one. Visual Tsunami makes use of hot opacities provided by the Los Alamos National Laboratory code TOPS [35]. The opacities are computed as a function of composition, density, temperature and photon energy.

6.3.2 Numerical Model

Eq. 6.9 is solved using the Adams-Bashforth-Moulton predictor-corrector method, as implemented in the MATLAB libraries. Accuracy of the time-integration is ensured via adaptive time-step control. Details of the time evolution are omitted here; suffice it to mention the space discretization:

$$\frac{\partial E(x_i,t^n)}{\partial t} = f(x_i,t^n) \tag{6.20}$$

where

$$f(x_i,t^n) = \frac{\partial}{\partial x}\left(k_{\text{eff}}(T_i^n)\frac{\partial T_i^n}{\partial x}\right) + \int_0^\infty 4\pi\mu_0(\nu,T_i^n)I(\nu,t^n)\,d\nu \tag{6.21}$$

The diffusion term is discretized in space with a centered scheme:

$$\frac{\partial}{\partial x}\left(k_{\text{eff}}(T_i^n)\frac{\partial T_i^n}{\partial x}\right) \approx \frac{k^n_{i-\frac{1}{2}}T^n_{i-1} - \left(k^n_{i-\frac{1}{2}} + k^n_{i+\frac{1}{2}}\right)T^n_i + k^n_{i+\frac{1}{2}}T^n_{i+1}}{(\Delta x)^2} \tag{6.22}$$

[4] A corollary of this work was to help debug the EPICSHOW code.

with

$$k^n_{i+\frac{1}{2}} = \frac{k^n_i + k^n_{i+1}}{2} = \frac{k^n_{e,i} + k^n_{e,i+1}}{2} + \frac{8\sigma}{3}\left(\lambda^n_{R,i}(T^n_i)^3 + \lambda^n_{R,i+1}(T^n_{i+1})^3\right) \tag{6.23}$$

It is assumed that:

$$\frac{\partial}{\partial x}\left(k_{\text{eff}}(T^n_1)\frac{\partial T^n_1}{\partial x}\right) \approx \frac{\partial}{\partial x}\left(k_{\text{eff}}(T^n_2)\frac{\partial T^n_2}{\partial x}\right) \tag{6.24}$$

and

$$\frac{\partial}{\partial x}\left(k_{\text{eff}}(T^n_I)\frac{\partial T^n_I}{\partial x}\right) \approx 0 \tag{6.25}$$

The source term is discretized as follows:

$$\int_0^\infty 4\pi\mu_0(\nu, T^n_i)I(\nu, t^n)\,d\nu \approx 4\pi\rho\sum_{\nu_g}^{G}\mu^n_i(\nu_g, T^n_i)I^n_i(\nu_g, t^n)\Delta\nu_g \tag{6.26}$$

where the continuous photon frequency interval has been discretized into G groups. For a monoenergetic pulse, this reads:

$$\int_0^\infty 4\pi\mu_0(\nu, T^n_i)I(\nu, t^n)\,d\nu = 4\pi\rho\mu^n_i(\nu, T^n_i)I^n_i(\nu, t^n) \tag{6.27}$$

The temperature is obtained by solving the following discrete equation:

$$E^n_i = \rho e^n_i + a\,(T^n_i(\rho, e^n_i))^4 \tag{6.28}$$

via Brent's method, as implemented in the MATLAB libraries.

6.3.3 Energy Profiles and Ablation Depths: A Review

In this section, several ablation models are reviewed. Most formulae are given for a monoenergetic x-ray pulse, but the approach is generic and can be easily applied to more complex spectra. (Visual Tsunami can handle any spectrum.) Even though there is no direct line of sight between the target and the solid first-wall in a thick-liquid protected chamber, the formulae will be developed for liquid and solid materials, since the latter case arises frequently

in ablation experiments and will be needed for the modeling of the condensation debris experiment, described in Chapter 7.

Upper-Bound Estimate

An upper bound estimate of the ablated mass can easily be estimated by assuming all the x-ray energy is distributed uniformly and used for heating and phase change:

$$m \approx \frac{\text{x-ray and ion energy}}{\text{specific cohesive energy}} \tag{6.29}$$

The specific cohesive energy is the energy required to heat and sublimate or vaporize the solid or liquid material, respectively. The cohesive energy is therefore given by:

$$e_c \approx c_v(T - T_0) + h \tag{6.30}$$

where c_v is the solid or liquid heat capacity at constant volume, T is the melting or boiling temperature, T_0 is the initial temperature, and h is the sublimation or vaporization enthalpy.

For a typical heavy-ion driven target, with a yield of 400 MJ and a fraction of yield going to x-rays and ions of 30%:

$$m \approx \frac{\text{x-ray and ion energy}}{\text{specific cohesive energy}} \approx \frac{0.3 \times 300 \times 10^6}{8 \times 10^6} = 15 \text{ kg} \tag{6.31}$$

This upper-bound is useful to check more refined models and for safety analyses.

Cohesive Energy Model

To first order, ablation is assumed to occur down to the depth where the specific energy equals the cohesive energy. Mathematically, the ablation depth δ, is given most generally by:

$$e(\delta) = e(x_{vap}) = e_c \tag{6.32}$$

For a monochromatic x-ray pulse, Eq. 6.19 applies and Eq. 6.32 reduces to

$$\delta = x_{vap} = \lambda \cos(\theta) \ln\left(\frac{\Phi}{\rho \lambda e_c}\right) \tag{6.33}$$

where λ (m) is the mean free path of the photons. If Φ is less than the threshold ablation fluence $\rho \lambda e_c$, no ablation occurs and $\delta = 0$.

Explosive Boiling

Down to the depth where the material temperature is greater than 90% of the critical temperature, classical nucleation theory predicts than the rate of nucleation will be extremely high, creating a region of bubbles, suddenly decreasing the pressure and launching rarefaction waves into the two-phase region below. This well-known result from the laser ablation community has recently been employed by Zaghloul and Raffray [84]. This approach can be summarized as:

$$e(\delta) = e_{\text{eb}} = c_v(0.9T_c - T_0) \tag{6.34}$$

$$\delta = \lambda \cos(\theta) \ln\left(\frac{\Phi}{\rho \lambda e_{\text{eb}}}\right) \tag{6.35}$$

This simple model consitutes a significant conceptual improvement over the cohesive energy approach.

Multi-Phase Region

Below the explosive boiling threshold, the energy deposition is sufficient to partially sublimate the solid layer or partially boil the liquid. Therefore, between the vapor phase and the solid (liquid) phase, there will be a multi-phase (two-phase) layer and it is reasonable to assume that some of the gas will escape off the surface ultimately. Thus, the ablation depth is

bounded by the sublimation (vaporization) depth and the saturation depth:

$$x_{\text{vap}} \leq \delta \leq x_{\text{sat}} \tag{6.36}$$

where x_{vap} is given by Eq. 6.33 and x_{sat} is defined by:

$$x_{\text{sat}} = \lambda \cos(\theta) \ln\left(\frac{\Phi}{\rho \lambda e_{\text{sat}}}\right) \tag{6.37}$$

where $e_{\text{sat}} = c_v(T_v - T_0)$.

Chen [11] chose to define the ablation depth δ where the vapor quality is one-half. His (arbitrary) choice stemmed from the fact that where vapor quality is high, the vapor would be likely to vent out of the two-phase region. It was also believed that the rarefaction wave launched into the liquid by the expanding ablated layer would liquefy the vapor trapped in the (low quality) two-phase region. Chen's approach can be summarized by:

$$\delta = \lambda \cos(\theta) \ln\left(\frac{\Phi}{\rho \lambda (e_{\text{sat}} + \frac{h}{2})}\right) \tag{6.38}$$

Another arbitrary approach has been retained in the IFE design study HIBALL and is currently used in the University of Wisconsin computer code BUCKY [55]. The energy contained in the two-phase layer is entirely used to ablate some more material. (This is sometimes referred to as "unexplosive explosive boiling," in opposition to the explosive boiling mechanism previously described.) The ablation depth δ is then defined implicitly as:

$$\int_{x_{\text{vap}}}^{\delta} e_c - e(x)\, dx = \int_{\delta}^{x_{\text{sat}}} e(x) - e_{\text{sat}}\, dx \tag{6.39}$$

Hence,

$$\int_{x_{\text{vap}}}^{\delta} h dx = \int_{x_{\text{vap}}}^{x_{\text{sat}}} e(x) - e_{\text{sat}}\, dx \tag{6.40}$$

and the ablation depth is given by:

$$\delta = x_{\text{vap}} + \frac{1}{h} \int_{x_{\text{vap}}}^{x_{\text{sat}}} e(x) - e_{\text{sat}}\, dx \tag{6.41}$$

Thus,

$$\delta = x_{\text{vap}} + \frac{1}{h}\left(e_{\text{sat}}(x_{\text{vap}} - x_{\text{sat}}) + \int_{x_{\text{vap}}}^{x_{\text{sat}}} e(x)dx\right) \tag{6.42}$$

Substituting 6.19 and using $\mu_0 = \lambda^{-1}$ yield:

$$\delta = x_{\text{vap}} = \frac{1}{h}\left(e_{\text{sat}}(x_{\text{vap}} - x_{\text{sat}}) + \int_{x_{\text{vap}}}^{x_{\text{sat}}} \frac{\Phi}{\rho\lambda} \exp\left(-\frac{x}{\lambda\cos(\theta)}\right) dx\right) \tag{6.43}$$

Integrating,

$$\delta = x_{\text{vap}} + \frac{1}{h}\left(e_{\text{sat}}(x_{\text{vap}} - x_{\text{sat}}) + \frac{\Phi\cos(\theta)}{\rho}\left(\exp\left(-\frac{x_{\text{vap}}}{\lambda\cos(\theta)}\right) - \exp\left(-\frac{x_{\text{sat}}}{\lambda\cos(\theta)}\right)\right)\right) \tag{6.44}$$

Making use of the definitions of x_{sat} and x_{vap} gives:

$$\delta = x_{\text{vap}} + \frac{e_{\text{sat}}(x_{\text{vap}} - x_{\text{sat}}) + \lambda\cos(\theta)(e_{\text{vap}} - e_{\text{sat}})}{h} \tag{6.45}$$

If the cohesive energy threshold is replaced by its explosive boiling counterpart, the previous equation becomes:

$$\delta = x_{\text{eb}} + \frac{e_{\text{sat}}(x_{\text{eb}} - x_{\text{sat}}) + \lambda\cos(\theta)(e_{\text{eb}} - e_{\text{sat}})}{h} \tag{6.46}$$

6.3.4 Discussion

TSUNAMI models typically neglected bleaching. Chen's fudge factor [11] is the only documented attempt at taking into account the fact that the ablated material becomes transparent to x-rays when heated to sufficiently high temperatures. Reradiation has never been modeled as part of the ablation module. (Jantzen [34] made some attempt at modeling reradiation from the ablated layer during the early phase of her gas dynamics simulations.) Back-of-the-envelope calculations indicate that for the typical fluences of interest, bleaching matters while re-radiation and heat conduction do not play a significant role, at least over short periods of

time. Fig. 6.1 and Fig. 6.2 display the energy deposition and resulting temperature profiles without bleaching nor re-radiation, and with bleaching and re-radiation. (Target parameters are those of the Z-IFE simulation described in Section 8.5; the standoff distance is 1.5 m and the incidence x-ray pulse is normal to the liquid surface.) The results with bleaching and

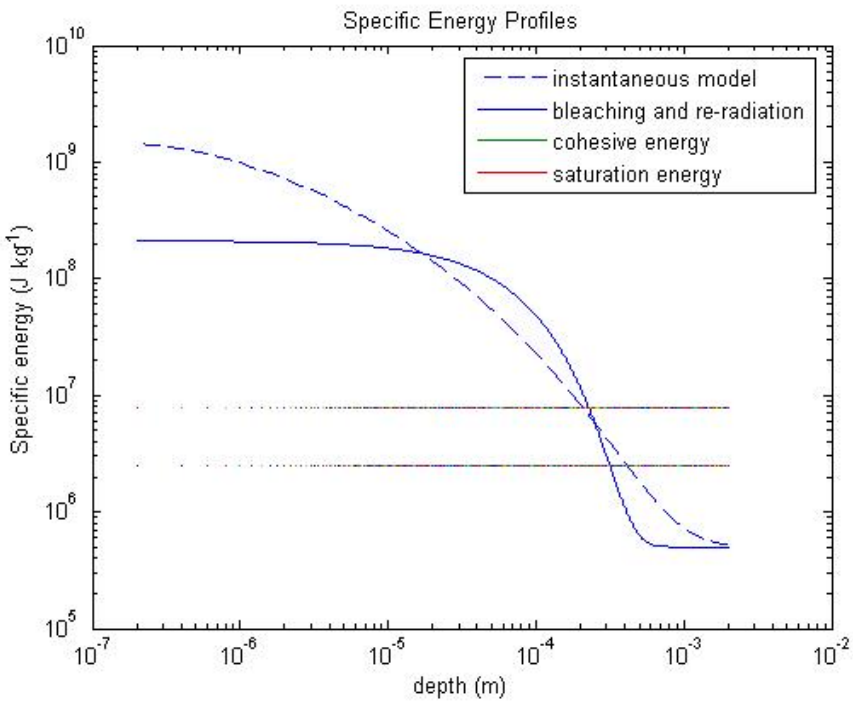

Figure 6.1: Comparison of energy deposition models for a typical Z-IFE case.

reradiation and those with bleaching but no reradiation (not shown) are actually almost the same. As expected, re-radiation does not play a role over the short period of times and at the relatively low temperatures of interest.

6.4 Conclusions and Perspectives

The new time-dependent ablation model with detailed equation of state and radiative properties helps predict reasonable temperature profiles. For the typical case presented here, the

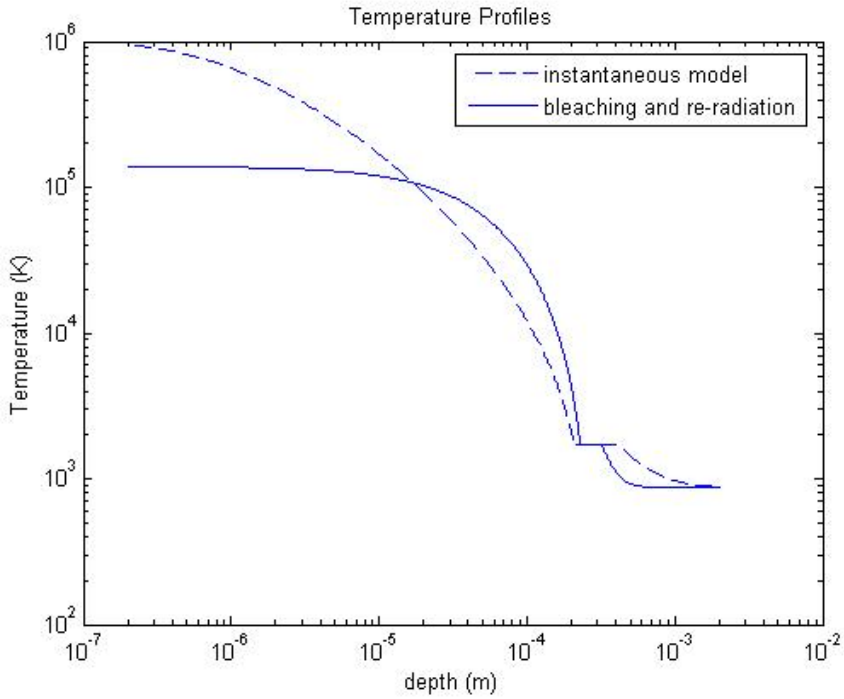

Figure 6.2: Comparison of temperature profiles.

acoustic penetration depth is on order of a tenth of the ablation length, which justifies *a posteriori* the assumption according to which the motion of the ablated material has been neglected. Accurate prediction of small ablation depths can sometimes be essential, for instance in dry-wall chambers. For such systems, the ablation model should be refined to include the mechanical response of the ablated material. The molten salts of interest for fusion systems have high heat capacities and might be slightly retrograde. Retrograde liquid-vapor mixtures may evaporate when expanded adiabatically—a phenomenon that a regular mixture cannot exhibit. Hence a tensile wave could vaporize a significant portion of the two-phase region that lies between the saturation and explosive boiling depths. Exploring this effect is expected to be interesting but is not essential for our purposes and is left for future work.

Part II

Applications

Chapter 7

The Condensation Debris Experiments

7.1 Overview of the Condensation Debris Experiments

In September 2003, a team led by the Lawrence Livermore National Laboratory started a new series of experiments to investigate in-flight condensation in complex geometries. Observing in-flight condensation of a multi-fluid gas and quantifying the resulting aerosol size distribution are the primary scientific goals of the series of Condensation Debris Experiments (CDEs). In-flight condensation may occur in a thick-liquid protected chamber; developing a predictive capability therefore is of interest. In dry-wall chambers, in-flight condensation may create a fog of droplets that might degrade target and beam propagation. HYLIFE-II and its variants are less prone to this aerosol issue. The oscillating jets are designed to clear the center of the pocket dynamically and the use of cold droplet sprays should cause most of the remaining hot areosols to evaporate.

Fig. 7.1 shows a generic representation of the experimental setup. (The particular device depicted in Fig. 7.1 was fielded on the Z-Beamlet facility at Sandia National Laboratory, New

Mexico, USA, in April 2004 and is about 30-cm high and 15-cm wide. A similar setup was used for all the experimental campaigns.)

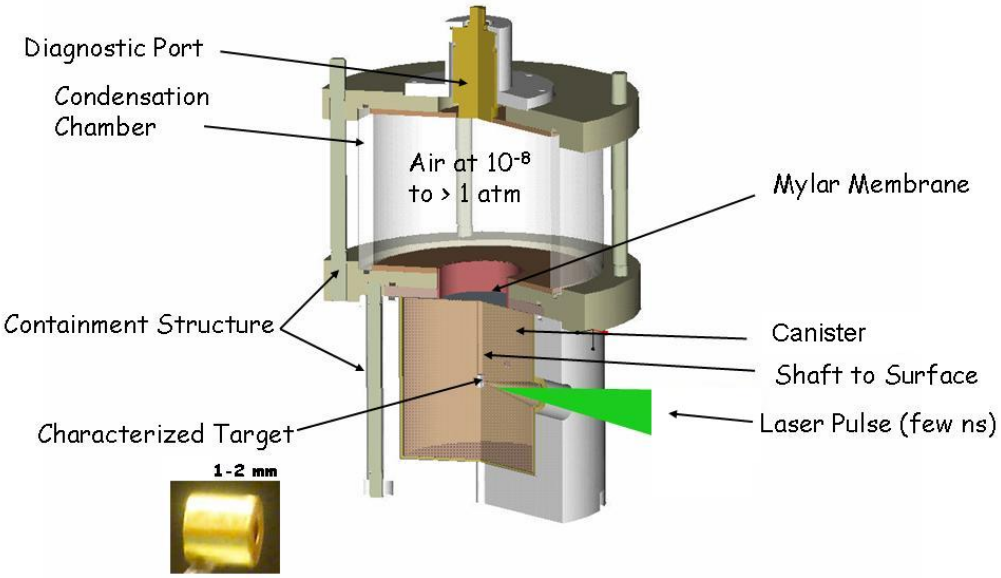

Figure 7.1: Schematic of the Condensation Debris Experiment.

A laser beam is used to illuminate a target (or “halfraum”) and generate a superheated vapor. Most of the halfraum debris will then jet outside of the canister through the large vertical shaft, while some will vent through the narrow horizontal laser entrance cone. Simple arguments based on the ratio of the canister shaft to laser entrance hole areas indicate that the leakage through the laser hole can be neglected to first order. (TSUNAMI simulations, not reported here, confirmed this assertion.) The halfraum debris expands in the canister shaft and into the condensation volume on top of the halfraum canister. The hot halfraum interacts with the cavity and the shaft walls: A thin layer of the inner surfaces of the canister is expected to be ablated. Ultimately, the debris from the halfraum and the canister will mainly

condense on-flight or onto the surfaces of the upper chamber. A background gas was present in the condensation chamber to favor in-flight condensation over surface condensation. (A thin membrane was used to hold the background gas in the condensation chamber; it was designed to rupture when hit by the halfraum debris.)

The gas jet exiting the canister was recorded by a CCD camera in order to check that the halfraum was actually hit by the laser. A pressure gauge (not shown in Fig. 7.1) can be inserted through a port at the top of the condensation chamber. Collection surfaces are analyzed for particle composition and size distribution. The experimental results concerning halfraum x-ray output and debris condensation were not modeled in detail with TSUNAMI and are not presented. Only a reference experiment, made with a near-vacuum background, is reported and compared to Visual Tsunami predictions.

7.2 Dimensioning of the Condensation Chamber

Obviously, the condensation chamber needs to be long enough for the gas plume to condense in-flight before reaching the top lid. Assuming that the gas follows the ideal gas law and expands isentropically in the condensation chamber from an original volume V_0 and temperature T_0 to a volume V and a temperature T of order a couple of times the boiling temperature, the adiabatic equation reads:

$$\frac{T}{T_0} = \left(\frac{V_0}{V}\right)^{\gamma-1} \tag{7.1}$$

or

$$V = V_0 \left(\frac{T_0}{T}\right)^{\frac{1}{\gamma-1}} \tag{7.2}$$

We assume that the original volume is that of the exit shaft and that the plume only expand axially, and not radially:

$$\pi R_{\text{shaft}}^2 L_{\text{chamber}} = \pi R_{\text{shaft}}^2 L_{\text{shaft length}} \left(\frac{T_0}{T}\right)^{\frac{1}{\gamma-1}} \tag{7.3}$$

Hence,

$$L_{\text{chamber}} = L_{\text{shaft length}} \left(\frac{T_0}{T}\right)^{\frac{1}{\gamma-1}} \tag{7.4}$$

Visual Tsunami predicts that the gas temperature at the shaft exit is of order of 5×10^4 K; as already mentioned, in-flight condensation for gold is estimated to begin to occur when the plume temperature is a couple of times the gold boiling temperature $T_b \simeq 3 \times 10^3$ K. This leads to:

$$\frac{L_{\text{chamber}}}{L_{\text{shaft length}}} \approx \left(\frac{5 \times 10^4}{5 \times 10^3}\right)^{\frac{1}{\frac{5}{3}-1}} \approx 30 \tag{7.5}$$

For a 1-cm shaft length,

$$L \approx 10^{-2} \left(\frac{5 \times 10^4}{5 \times 10^3}\right)^{\frac{1}{\frac{5}{3}-1}} \approx 0.3 \text{ m} \tag{7.6}$$

On the one hand, this approach is somewhat conservative. First, the actual plume expands in a cone whose half-angle is a function of time and is bigger than the assumed cylinder. Secondly, the plume is likely to be hot enough to radiate while expanding, especially near the shaft exit, causing the temperature to drop over distances shorter than those predicted by the adiabatic model. (In the case of the CDE vacuum shots performed in November 2003, the gas jet was observed to be hot enough to radiate.) Finally, there is some mixing between the plume and the background gas, if the density of the latter is high enough. On the other hand, the estimated initial temperature at the exit of the shaft may be too low for high laser energies and small shaft lengths. (The value of 5×10^5 K was inferred from the particular Visual Tsunami simulation presented in Section 7.3.)

Eq.7.6 indicates that the condensing chamber fielded on the Z-Beamlet facility at Sandia might have been too small for in-flight condensation to be dominant, at least for the low background gas density shots with the pressure gauge. (A high-density low-temperature background gas causes the debris jet to cool down faster and favors in-flight condensation.) Plans exist to field the experiment on the National Ignition Facility, which would allow for a bigger condensation volume. (The size of the CDE setup is limited by that of the experimentation chamber of the facility in which CDE is fielded.)

7.3 Visual Tsunami Simulations of CDE

The detailed use of TSUNAMI 2.8 as a design code to assist successfully in the dimensioning of the experimental apparatus is not reported here; only the Visual Tsunami 2.0 modeling of one experiment of the first campaign is presented. (Visual Tsunami was not ready in Fall 2003 when most of the design work was performed and TSUNAMI 2.8 was therefore employed at the time.)

As a first attempt at modeling CDE with Visual Tsunami, an ideal gas law is used and multi-species effects are neglected. Compared to the actual geometry, the orientation of the halfraum is shifted and its axis of symmetry aligned with the canister shaft. Initial conditions are obtained using simple ICF scaling laws developed to model similar cylindrical hohlraums [2]. Fig. 7.2 shows four Visual Tsunami 2.0 density contour plots at various times.

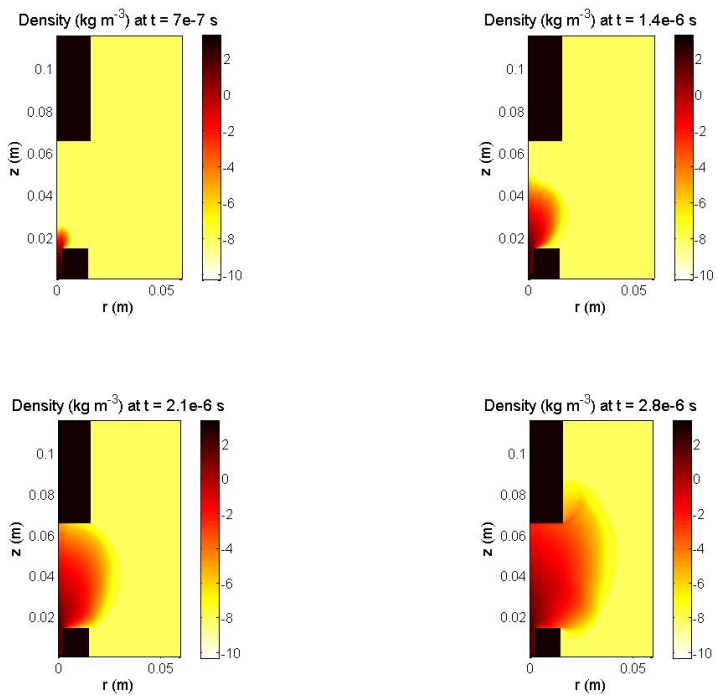

Figure 7.2: Visual Tsunami density contour plots. The density of the solid structures is arbitrarily low.

7.4 Experimental and Numerical Results

A CCD image was recorded and is compared to a Visual Tsunami 2.8 time-integrated contour plot in Fig. 7.3. (The pictures are to the same vertical scale.)

Both the Visual Tsunami snapshot (left) and CCD image (right) show the same three phases of early gas dynamics in the condensation chamber, along the vertical axis. First, near the exit of the canister shaft (bottom of picture), the gas is still dense and radiating. The gas then expands, its density decreases, and its thermal energy is converted into kinetic energy. Finally, the gas hits the gauge surface and stagnates. Its density increases and its kinetic energy is converted back into thermal energy. The expansion around the gauge takes a remarkably similar “whisker” shape on the CCD picture and Visual Tsunami time-integrated contour. A better qualitative agreement could be obtained by space integrating the Visual Tsunami snap-

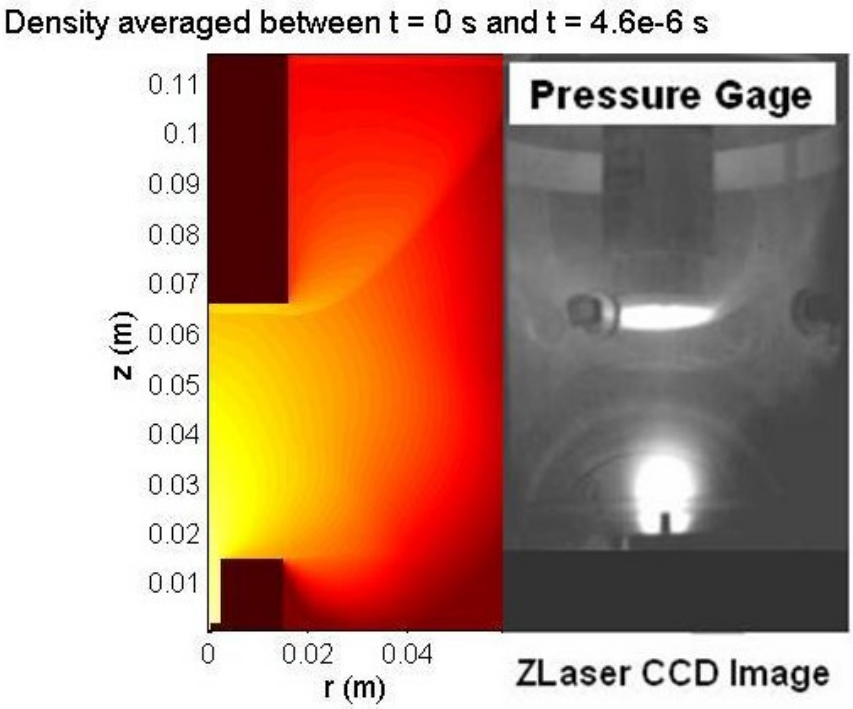

Figure 7.3: Visual Tsunami 2.0 time-integrated contour plot and CCD image.

shots along the line of sight. Since the CCD picture was meant to be a mere visual check that a debris plume was formed and was not intended to be used for comparison with Visual Tsunami, no further analysis was performed.

7.5 Conclusions and Perspectives

Agreement between Visual Tsunami simulations and experimental results is satisfactory and constitutes a first validation of Visual Tsunami as a design tool for gas dynamics systems. Three directions could be explored for more accurate simulations. First, a detailed radiation hydrodynamics simulation would be helpful to provide the initial conditions to Visual Tsunami. Second, a few physical models could be improved: for instance, real gas effects, radiation diffusion, detailed gas/solid interaction, and in-flight condensation could be taken

into account. Finally, a three-dimensional simulation would better take into account some of the geometrical effects.

Chapter 8

Gas Venting in Thick-Liquid Protected Fusion Chambers

8.1 Introduction

Four thick-liquid protected chambers are described in this chapter. First, the Robust Point Design [79] chamber is considered. The Robust Point Design uses a variant of the HYLIFE-II chamber [43, 44, 31, 45] compatible with the neutralized ballistic transport mode. (The heavy-ion beams are charge-neutralized before entering the target chamber and then travel to the target on their own, ballistically.) The second chamber is another variant [28] of HYLIFE-II tailored for the assisted-pinch transport scheme. (The heavy-ion beams travel through a channel that a laser creates in the target chamber background gas.) The third chamber is the vortex chamber [28], which is compatible with final-focusing performed by a set of solenoidal magnets. The physics of the different heavy-ion beam propagation schemes was reviewed by Olson [48], Rose *et al.* [59], and Davidson *et al.* [23]. The fourth chamber is compatible with

a Z-pinch driver.

8.2 Neutralized Ballistic Final-Focusing

8.2.1 Gas Density Control

Target Chamber Gas Density Control

The RPD-2002 target chamber is based upon the HYLIFE-II design [45]. Fig. 8.1 shows the thick-liquid jet configuration in RPD-2002. The pocket around the target has been docu-

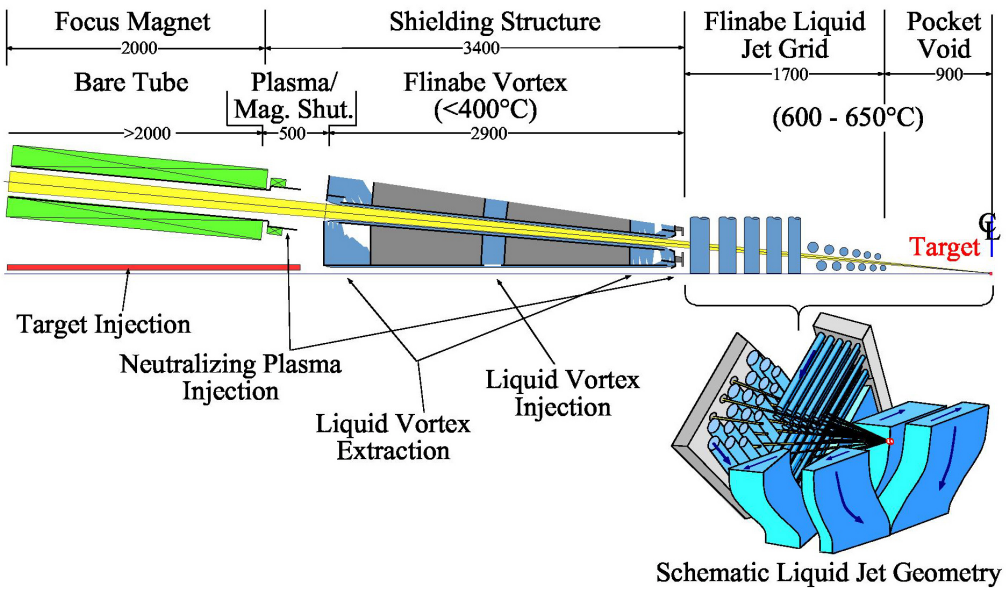

Figure 8.1: Scaled cross-section of the RPD chamber and beam-lines [26, 27]. Lengths are in mm.

mented by Pemberton and coworkers [51] and is derived from the “hybrid” pocket presented by Peterson [52, 53]. The hybrid pocket uses oscillating slab jets [56, 66] with finely dispersed voids to mitigate the response of neutron heating and ablation shock waves. Other improvements concern the liquid configuration close to the beams: cylindrical jets replace the

HYLIFE-II slabs. All the major components of the pocket, such as the cylindrical and voided slab jets, have been demonstrated in scaled fluid mechanics experiments using water [1, 51].

Flinabe has been chosen as the target chamber coolant in lieu of flibe, for reasons first advanced in References [24, 26]. Flinabe and flibe have similar neutronics and heat transfer characteristics. Flinabe has a lower melting point (less than 630 K), which allows its use at lower temperatures (≈673 K) in the beam tubes, where its equilibrium vapor pressure is very low. Flibe could be used in the target chamber, which operates at 873 K, but mixing of x-ray ablation debris from each region would require periodic purification of each molten-salt stream. Using flinabe for the main pocket therefore simplifies the design of the RPD-2002 power plant. The need for modeling of ablation and venting phenomena partially stems from the stringent requirements set for the propagation of heavy-ion beams. Ablation and gas venting phenomena must be modeled to predict how much mass is ablated and where it vents, so that appropriate condensing surfaces can be provided and the requirements for controlling debris propagation up the beam lines can be met. X-rays deposit onto thin layers of target facing thick-liquid structures and cause vaporization of a fraction of these layers. The ablation debris then expands off the jets. The pressure exerted on the surfaces results in an impulse load, equal to the time integral of the pressure history, which must be quantified to determine the mechanical response of the pocket. Ablation debris then fills the pocket interior and pressurizes it, adding to the impulse load to the pocket. The pocket has been designed to limit the venting up the beam tubes into the final-focus magnet region, where very little contamination of the metallic surfaces can be tolerated. Thus ablation and venting calculations can estimate the impulse delivered to inside surfaces of the pocket and how much debris reaches the beam ports.

Beam Line Gas Density Control

In the beam tubes, protection of target-facing beam tube metallic surfaces is improved by adding renewable liquid structures. Cold flinabe vortexes have been proposed to coat the first half of the beam tubes [24] and have been studied experimentally with scaled water experiments [50, 51]. The vortexes offer condensing surfaces for target chamber debris and background gas. In the beam tubes, flinabe can be used at a low temperature, around 673 K, at which the vapor pressure is expected to be less than 0.1 mPa [24]. This vapor pressure is too low to equilibrate with the vapor in the target chamber. The target chamber will blow gas in the beam tubes continuously to impose the vapor pressure at 873 K. Assuming that the flinabe vortex is a perfect absorber, the gas blown from the target chamber will expand isotropically. The density at any location z from the beam port is obtained by equating the number of gas molecules that enters the beam tube to the one of those that streams through a half sphere of radius z, and is therefore given by [26]:

$$n(z) = \frac{n(0)}{2}\left(\frac{R}{z}\right)^2 \tag{8.1}$$

where n is the gas density (m^{-3}) and R the beam port radius (m). For a 4-cm radius beam port, a two-meter long, perfectly condensing flinabe vortex reduces the density by a factor of 2×10^{-4}, and suppresses the needs for mechanical shutters to stop steady state vapor blowing into the final-focus magnet region. At the vortex end next to the final-focus region, the equilibrium density (2×10^{15} m^{-3}) will be dictated by the vapor pressure of flinabe at the vortex temperature, 673 K. The density decreases along the vortex as z^{-2} until it reaches the equilibrium value at the vortex temperature. Additionally, the vortexes protect the walls from target x-rays, ions, and neutrons while offering condensing surfaces for target chamber debris as well. Magnetic shutters have been proposed to divert the small fraction of debris that vents

past the vortex and must be diverted before reaching the final-focus magnet region [26]. As shown in Fig. 8.1, RPD-2002 includes equipment for injection of a neutralizing plasma and a magnetic shutter located between the last final focus magnet and the vortex. A second neutralizing plasma injection location is also provided between the exit of the vortex tube and the main chamber. The magnetic shutters use an ionizing plasma, a magnetic dipole to stop and sweep the debris, and a debris condenser. The same plasma and injection system are used to neutralize the beam and subsequently ionize the fraction of the debris that is gaseous. Before the debris arrives, the plasma density must be ramped up substantially from its low value used for space charge neutralization. The typical strength of the magnetic field and the length of the dipole have been investigated [26] and are reasonable: typically 0.1 T over 15 cm. The dipole will also help prevent emittance growth through neutralizing electron streaming up the beams. A magnetic field of 0.2 T applied over 5 cm is enough to mitigate this effect [26]. A more detailed description of the magnetic shutter system is provided in Ref. [26]. Integrated simulations encompassing the beam tubes and the target chamber provide estimates for the amount of and the ionization state of the debris that must be diverted by the magnetic shutters, allowing the design of the shutters.

8.2.2 TSUNAMI Ablation and Venting Simulations

Recent TSUNAMI simulations of the HYLIFE-II-like hybrid target chambers were presented by the author in References [24, 26, 27]. The geometry of the liquid structures modeled here is closely related and assumptions are similar. Visual Tsunami was not available at the time of these studies, and an improved variant of TSUNAMI 2.6 [12] was employed. The code TSUNAMI 2.8 solves the one-dimensional Euler equations for compressible flows using

a Godunov scheme. Operator splitting is used for these two-dimensional axially-symmetric simulations. Viscous and magnetic effects are neglected compared to convection. X-ray ablation from the hot target is assumed to be instantaneous and adiabatic. Rapid condensation is expected to occur onto droplet sprays [5, 41] injected in the main chamber and onto the vortexes [6, 7], so these regions are treated as open boundaries in the calculation. The thick-liquid jets are modeled as perfectly reflective: convective effects are assumed to be preponderant in this region. Liquid jet motion is neglected over the sub-millisecond time scales of the venting process. Typically, in one millisecond, the jets move by a millimeter, a fraction of the length of a TSUNAMI computational cell. Isochoric heating launches rarefaction waves into the jets and disrupts them, which will at longer times block the direct line of sight that exists from the beam tubes to the target. As far as the geometrical assumptions are concerned, the mass flux at the beam ports is expected to be overestimated. Fig. 8.2 shows a cutaway view of the simulation geometry. The two trapezoids and the block in between simulate the voided slab jets, while the dots represent the cylindrical jets. Only one beam tube is simulated in the top left-hand corner, on the axis of symmetry. (In the actual chamber, the centerline tube is reserved for the target injection system.)

This TSUNAMI model simulates gas dynamics phenomena from the end of the target and hohlraum disassembly to the time when only a small gaseous fraction of the initial mass and energy remains in the target chamber near the main pocket. Spatially, they are the first to cover all the thick-liquid structures and a beam tube, up to the magnetic shutters, in an integrated manner. Fig. 8.2 shows four TSUNAMI 2.8 density contour plots. The expansion of the ablated debris off the liquid surfaces from which they were vaporized can be seen on the first plot. The other three plots show the venting of the target and ablation debris through the

thick-liquid structures, as well as the expansion of vortex ablation debris up the beam tube and down into the target chamber. Figures 8.3 and 8.4 show the peak pressure on the target-facing

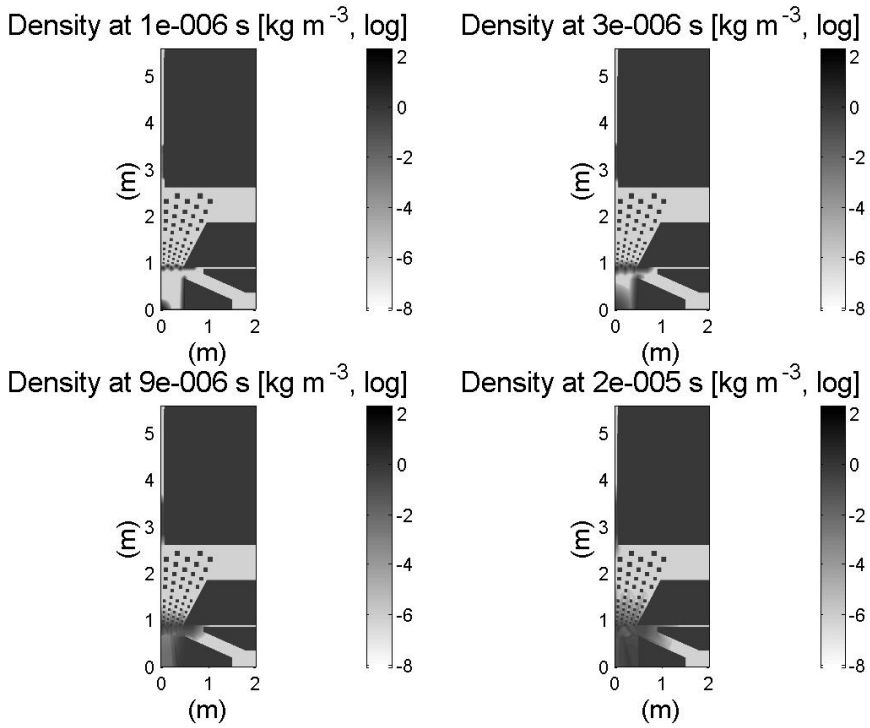

Figure 8.2: TSUNAMI density contour plots at various times. The density of the liquid and solid structures is arbitrarily low.

side of the oscillating liquid slab and the impulse load on the same slab, respectively. The first part of the impulse load is due to the rocket effect when the ablated layers expand off the slab surface; the second part of the impulse is due to the pocket pressurization while the target and ablation debris vent through the pocket. Minimizing this venting time by offering large venting openings is a note-worthy feature of the RPD jet configuration. As discussed in Section 8.2.3, the predicted impulse has been shown to be manageable in scaled partial pocket experiments [51].

Thick-liquid pocket were originally designed to minimize the debris flux up the beamlines. TSUNAMI helped confirm that the mass output at the entrance of the beamlines would be too

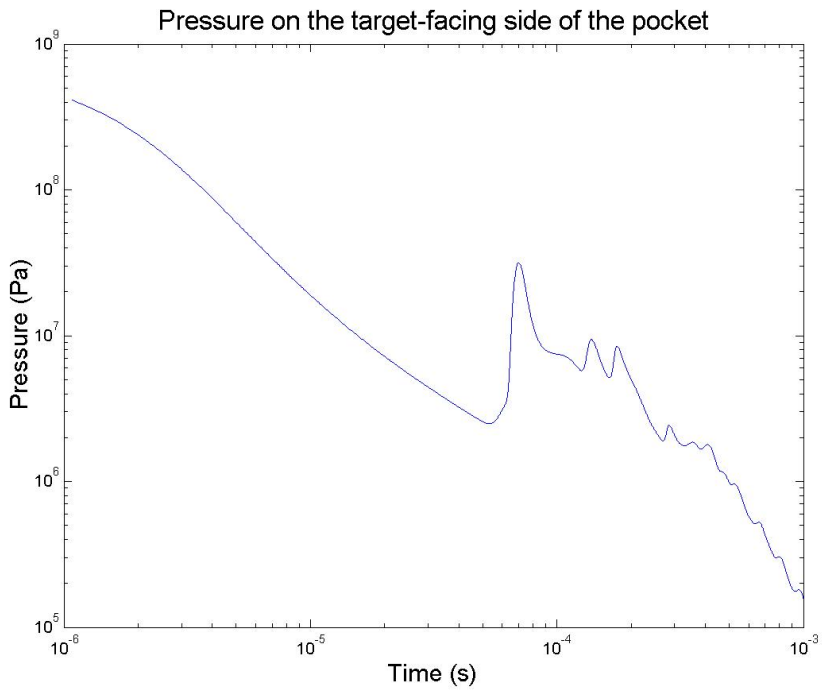

Figure 8.3: Peak gas pressure onto the liquid pocket in the RPD chamber.

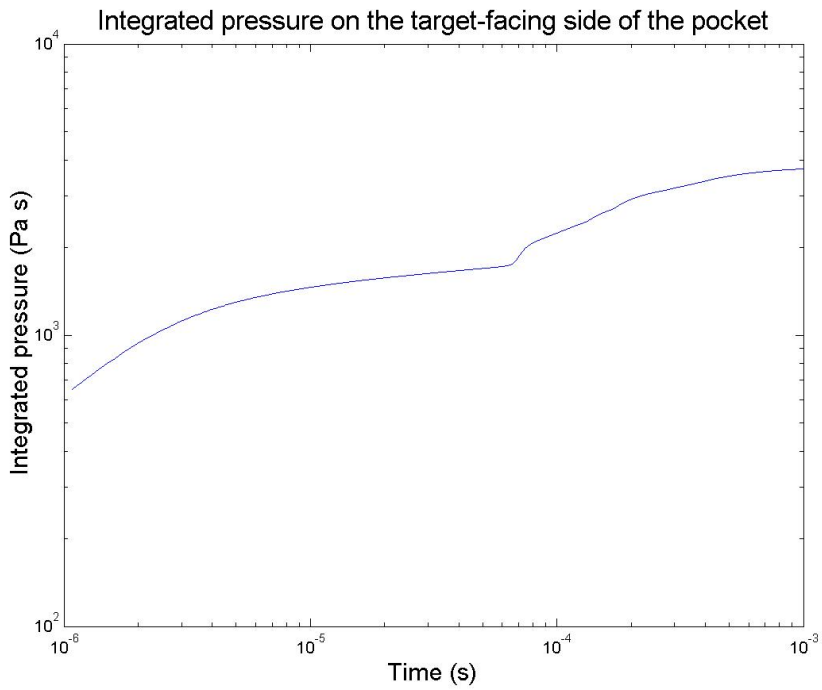

Figure 8.4: Impulse load to the liquid pocket in the RPD chamber.

high, all the more with the recent recognition that neutralized ballistic transport requires no debris contamination in the final-focus magnet region. Figures 8.5 and 8.6 show the density at the entrance of the centerline tube and the integrated mass flux at the same location. Ablation

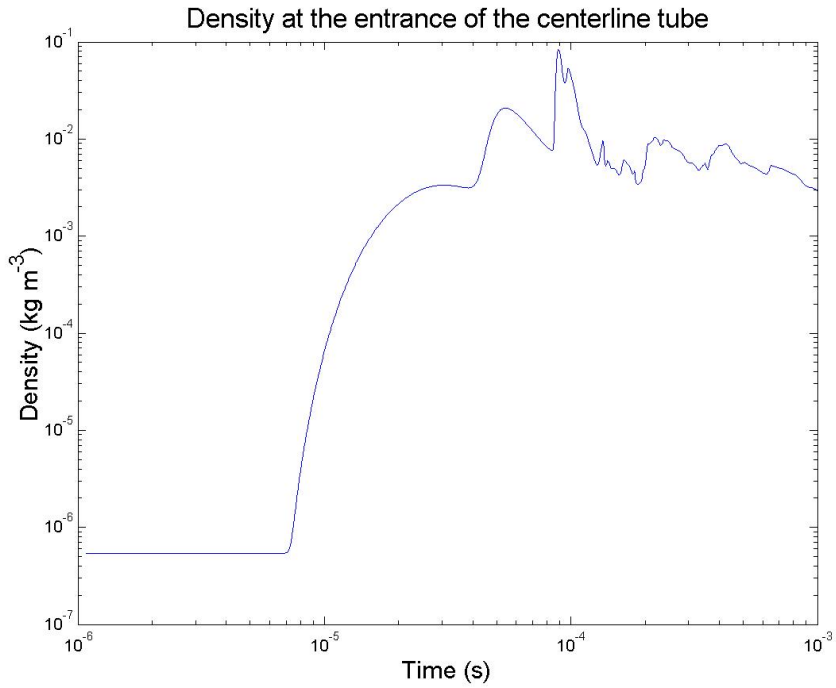

Figure 8.5: Density at the entrance of the RPD centerline tube.

debris expanding off the vortex into the target chamber causes the initial negative mass flux. The use of a vortex partly stems from the need to accommodate this mass output [24].

Figures 8.7 and 8.8 display the density and integrated mass flux at the entrance of the magnetic shutters, past the liquid vortex. The last two plots can be compared to Figures 8.5 and 8.6. The cold vortex remarkably reduces the mass output up the beamlines, but, even when assumed a perfect condenser, the vortex is not long enough to suppress any debris ingression in the final-focus magnet region. Accommodation on debris up the beamlines has never been tackled in detail in any heavy-ion power plant study. Usually mechanical shutters would be envoked, but these TSUNAMI simulations show debris will arrive before the closing of fast

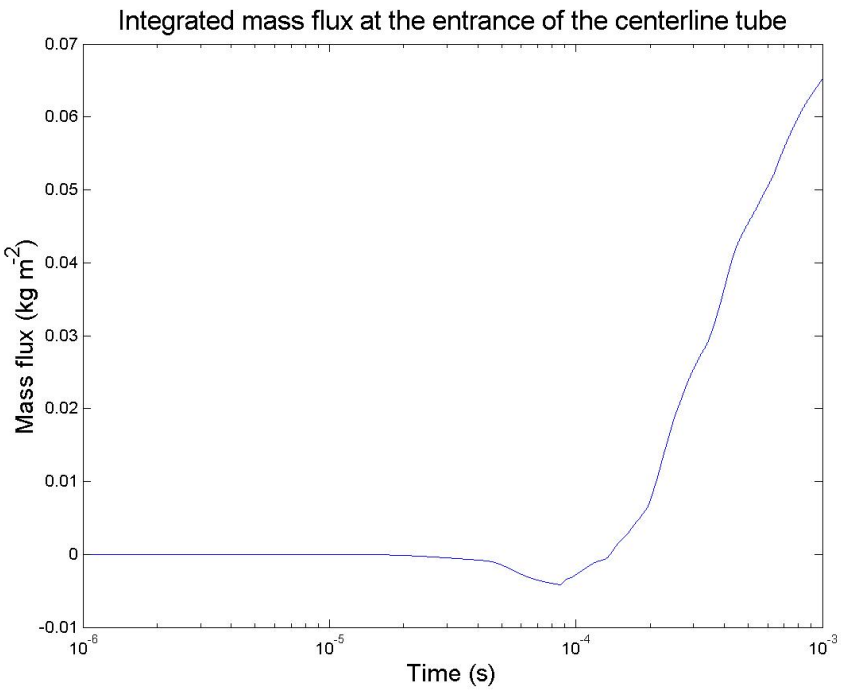

Figure 8.6: Integrated mass flux at the entrance of the RPD centerline tube.

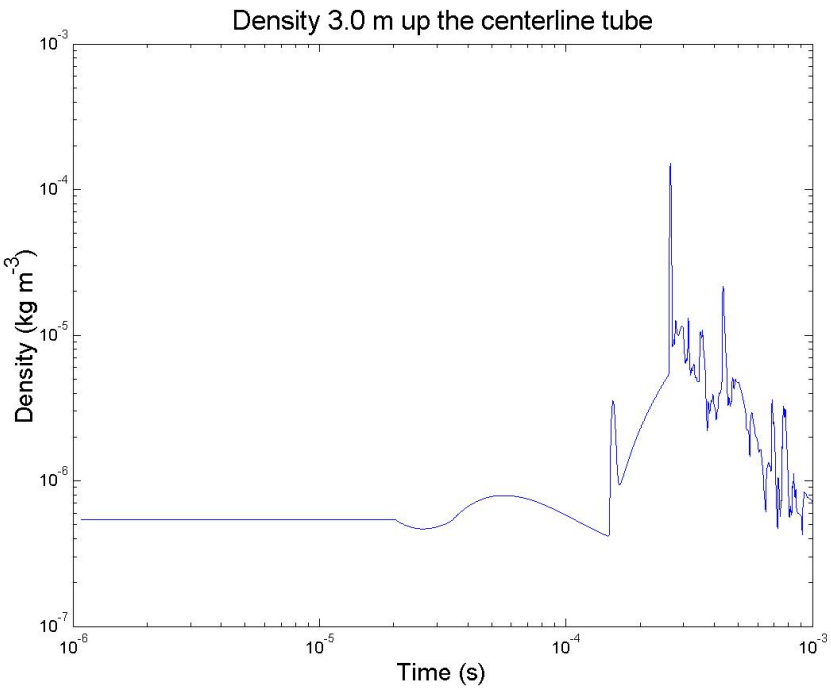

Figure 8.7: Density at the entrance of the magnetic shutters in the RPD centerline tube.

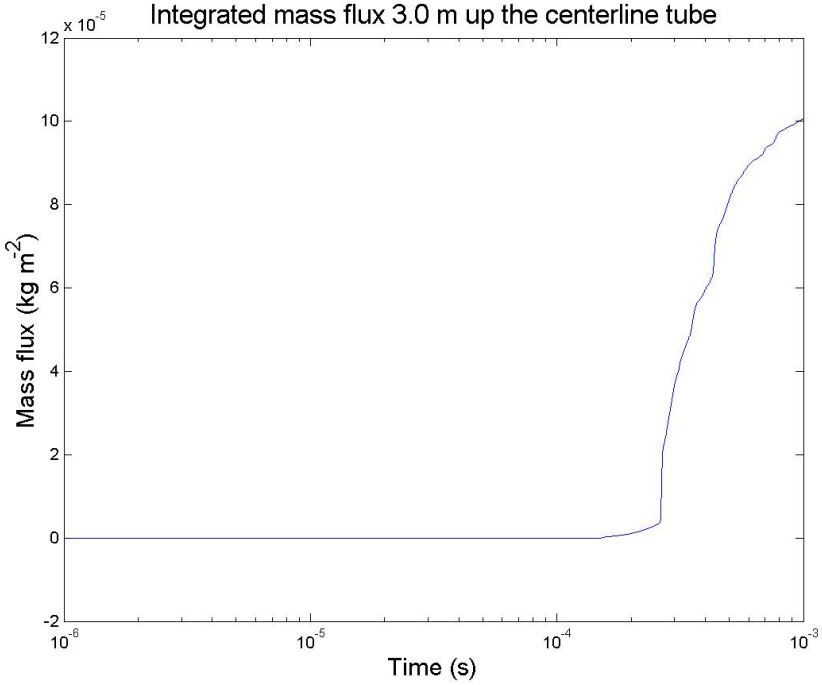

Figure 8.8: Integrated mass flux at the entrance of the magnetic shutters in the RPD centerline tube.

mechanical shutters. Magnetic shutters were proposed instead [26]. At the entrance of the magnetic shutters, TSUNAMI predicts that the time-integrated mass and energy fluxes are 1×10^{-4} kg m^{-2} and 1×10^{3} J m^{-2}, respectively. The average plasma molecular density, temperature, and axial speed are 3×10^{20} m^{-3}, 2×10^{4} K, and 3×10^{4} m s^{-1}, respectively. (The radial speed is negligible.) PIC simulations performed with the LSP code indicate that such plasma can be stopped by a reasonable magnetic field—0.1 T applied over 5 cm [26]. The relatively low temperature implies that the gas is not (fully) ionized, hence the need for the ionizing plasma. (All the more that the temperature is likely to be overestimated in this simulation, performed without radiation.)

8.2.3 Possible Optimization

Hohlraum

Obviously, the target and hohlraum must be designed so that a substantial yield is obtained, but other considerations are also important, such as fabrication feasibility, cost, and recoverability from the chamber coolant. Several parameters are relevant to our gas dynamics modeling, such as total mass, yield, energy partitioning, and the temperature of target and hohlraum after disassembly. The yield is determined by target physics and power plant economics. The mass of casing material around the hohlraum can be increased and its shape can be modified to control the x-ray temperature, the partitioning of the energy between x-rays and target debris, as well as the anisotropy of the expansion of the target debris. Investigation of multi-dimensional effects and optimization of the target output have not been performed yet. Here the expansion of the target debris is assumed to be spherically symmetric and the x-rays radiated from the target are assumed to have a spectrum characteristic of a 500 eV blackbody.

Liquid Geometry

The inner-radius of the pocket is chosen to avoid excessive bulk boiling due to the heat deposited by the neutrons and to avoid excessive impulse loading due to target and ablation debris, before venting has occurred. TSUNAMI 2.8 predicts an impulse load of 3 kPa s. Distributed uniformly into a layer of flinabe 60-cm thick, this impulse momentum results in an outward velocity of 2 m s^{-1}—20% of the injection velocity. Partial pockets have been created, disrupted under slightly higher scaled impulse loads, and subsequently reformed in a timely manner in scaled water experiments [51]. The volume of the inner pocket and the open area through the oscillating slab jets determine how rapidly the pocket vents and how pressure

builds up. Increasing the venting area would reduce the impulse load, if necessary.

8.3 Assisted-Pinch Final-Focusing

8.3.1 A variant of the RPD Chamber with Assisted-Pinch Focusing

As discussed, the Robust Point Design includes a detailed description of a thick-liquid protected chamber, based on the HYLIFE-II design [45]. Experiments and simulations led to a few changes to the baseline HYLIFE-II: for instance, the RPD oscillating sweeping jets have approximately a 50% porous void fraction and are generated using flinabe ($LiNaBeF_4$) molten salt rather than flibe (Li_2BeF_4). Flinabe liquid vortexes and stationary cylindrical jets are used to protect the beam ports. A heavy-ion inertial fusion power plant including assisted-pinch final focusing and thick-liquid walls based on the HYLIFE-II design was presented by Yu and co-workers in 1998 [76]. Recently, the author proposed to modify Yu's design and introduced the same improvements to the HYLIFE-II design that were made to finalize the RPD [28]. Fig. 8.9 shows a schematic of the modified chamber, yet to be optimized.

The assisted-pinch requires a background gas density equivalent to 5 Torr of Xe at 873 K; this high-density heavy-element background gas is required to establish and maintain the integrity of the plasma channels that guide the heavy-ion beams. (Using the non-condensable Xe may reduce the condensation rate and might require an increase of the condensing spray flow rate, but this is not expected to be an issue.)

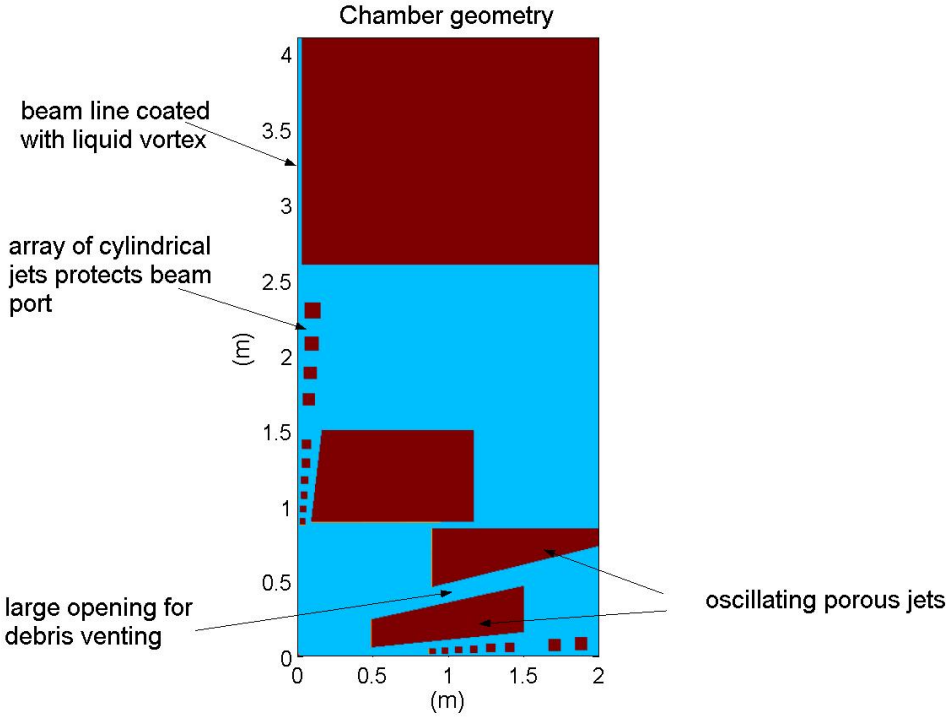

Figure 8.9: Geometry of the assisted-pinch chamber.

8.3.2 TSUNAMI Ablation and Venting Simulations

Numerical models and assumptions are similar to those used for the RPD modeling and other related thick-liquid chambers recently modeled with TSUNAMI. As usual, the motivation for these simulations stems from the need to determine the pocket response and the cleanliness and background gas requirements set by proper beam and target propagation. Target x-rays deposit most of their energy in thin liquid layers that are then vaporized. Fig. 8.10 shows four density contour plots at different times, showing the expansion and venting of the target debris and ablated layers. The impulse load to the thick-liquid structures in the assisted-pinch chamber is shown on Fig. 8.11. As usual, the first part of the impulse load comes from the rocket effect as the ablated layers expand against the liquid structures. The second part of the loading comes from the pocket pressurization. Since the assisted-pinch thick-liquid pocket

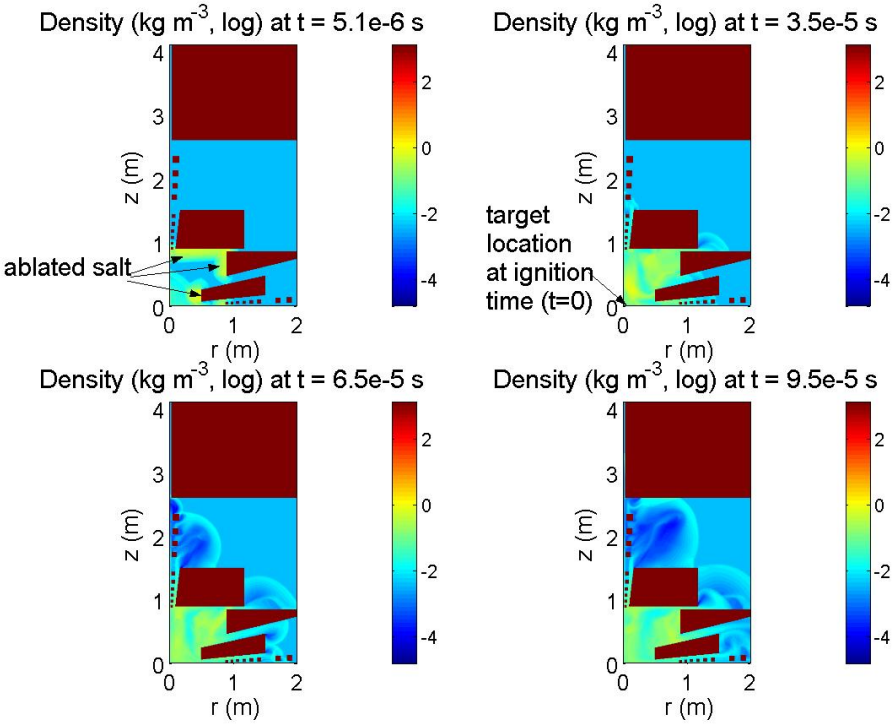

Figure 8.10: TSUNAMI simulations of the assisted-pinch chamber. The density of the liquid and solid structures is arbitrarily low.

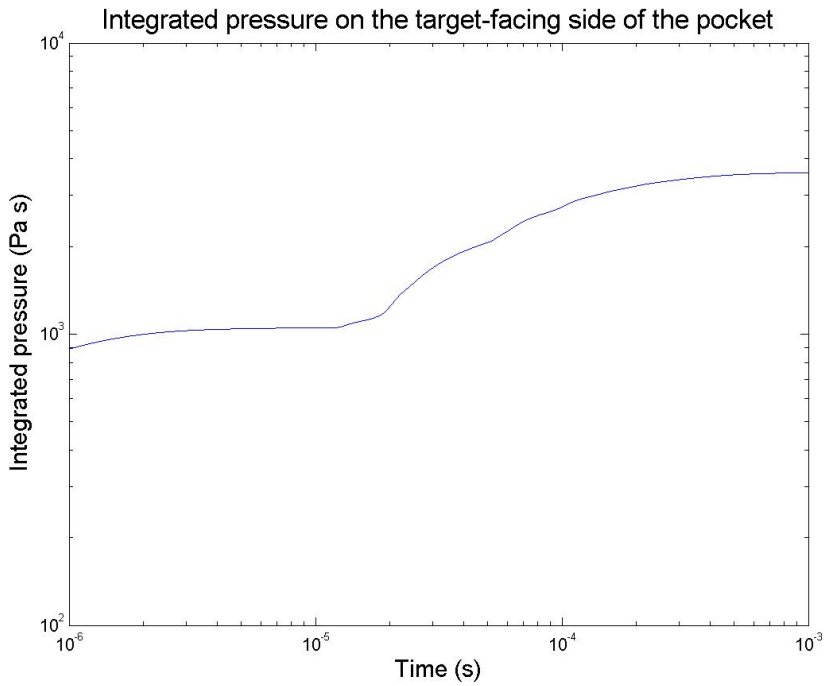

Figure 8.11: Impulse load to the liquid pocket in the assisted-pinch chamber.

derives closely from the RPD chamber and the target yield and output are assumed to be those of the RPD, the assisted-pinch impulse load is similar to that obtained for the RPD. Mass fluxes up the beam lines are similar to the neutralized ballistic case and are not reported here since the cleanliness requirements are less stringent in the assisted-pinch case. (Here, the heavy-ion beams are charge-neutralized before entering the beam tubes.) If necessary, magnetic shutters similar to those described for the neutralized ballistic mode could be employed.

8.4 Solenoidal Final-Focusing

8.4.1 A Novel "Vortex Chamber" for Solenoidal Focusing

A novel chamber geometry was recently proposed to accommodate the solenoids that may be employed to final-focus the ion beams [28]. Fig. 8.12 illustrates this concept. The dark layer in Fig. 8.12 represents the swirling vortex flow. The vortex will expand past the ends of the target chamber, in order to protect the beam lines and offer additional condensation surfaces for background vapor, target debris and ablated salt.

The vortex is a variation of the device presented by Pemberton and co-workers [50] and integrated into the RPD to generate a liquid layer inside the beam tubes. Pemberton used one injection and two extraction sections. For the large aspect ratio vortex envisioned for the solenoid chamber, fluid is injected and extracted continuously along the wall, as shown conceptually on Fig. 8.13.

Proper beam propagation for solenoid focusing requires a high background electron density for space charge neutralization and a low background ion density to minimize scattering. A low-Z gas such as He or H_2 is being considered for the drift lines, while a compromise be-

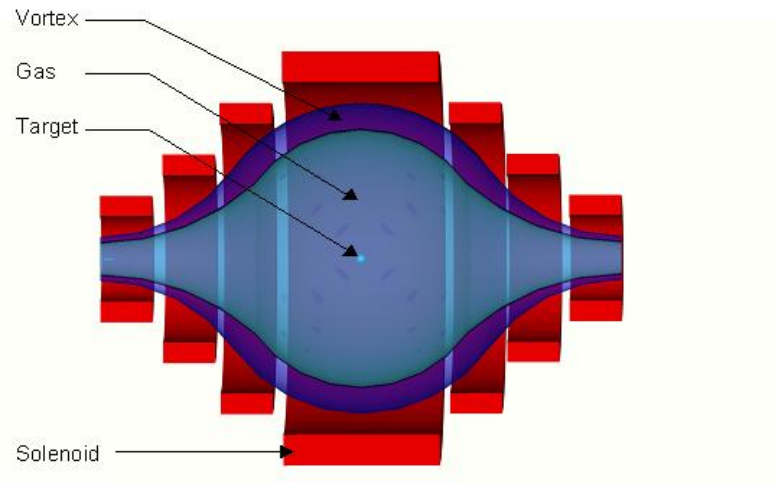

Figure 8.12: Schematic of the vortex chamber [28]. The first wall is not depicted.

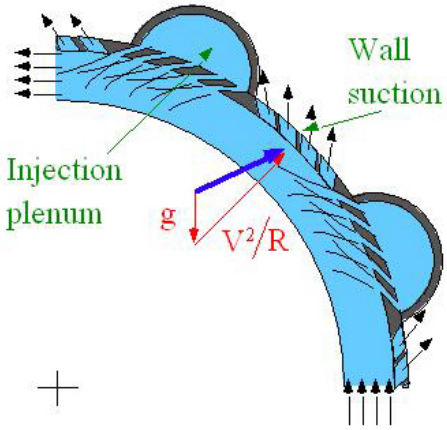

Figure 8.13: A combination of liquid blowing and sucking generates the vortex flow. The centrifugal force maintains the flow attached to the wall [28].

tween the electron and ion density requirements could be achieved in the vortex chamber using the flinabe vapor in equilibrium with the liquid jets at 873 K. Higher densities, if desirable, could be achieved using a molten salt more volatile than flinabe or flibe. A mixture of LiF, BeF_2, and ZrF_4 could be a reasonable candidate to obtain high vapor pressure and a sufficient tritium breeding ratio. (Obtaining high vapor pressure with flinabe or flibe would require an operating temperature that would raise chamber material issues.) There is some concern over the activation of Zr, but limiting the residence time in the chamber may avoid the generation of long-lived elements.

8.4.2 Vortex Response to Target Output

The target neutrons will deposit a significant fraction of their energy in the liquid layer over very short time scales, heating the liquid isochorically. Isochoric heating will generate rarefaction waves and, after reflection off the first wall, tensile waves; the standoff distance to the target (at least two meters) is expected to be sufficient to avoid spallation off the vortex surface and excessive loading to the first wall. However, x-rays will deposit their energy over small distances in the target-facing surface of the liquid vortex and will vaporize small layers, possibly launching waves into the bulk of the vortex and causing spallation and droplet ejection. Increasing the mass of the hohlraum could shift down the x-ray spectrum and cause a substantial fraction of the x-ray energy to be radiated at lower energies over time scales that could possibly be long enough for the heat to be accommodated by the vortex through heat conduction and surface renewal. If the target casing is designed optimally, a significant fraction of the target yield could then be accommodated without inducing much x-ray ablation off the surface of the vortex. The effect of the solenoidal magnetic field on target and ablation

debris expansion has not been investigated, but back-of-the-envelope estimates tend to indicate that the debris will first expand hydrodynamically and then be deflected into the vortex by the solenoidal magnetic field. A small fraction, yet to be quantified, will jet up the centerline. Significant work remains to be done and is outside of the scope of this dissertation, which is centered around the target chamber and beam tube interface in the Robust Point Design. A detailed Visual Tsunami model would require including a magneto-gasdynamics algorithm.

8.5 Z-Pinch Inertial Fusion Energy

8.5.1 Z-Pinch Target Chamber

A “Z-pinch” is an x-ray source made of an array of tiny wires. An intense current is pulsed through the wires and causes them to collapse inwardly. When the wires stagnates, x-rays are produced. A recyclable transmission line (RTL) brings the current to the Z-pinch. Parts of the RTL will be destroyed by the exploding target and the RTL will be replaced after each shot. The Z-pinch and RTL are surrounded by a neutronically-thick array of vertical jets. As usual, the thick liquid structures are interposed between the target and the solid first wall. X-rays and ions are stopped in the jets and neutrons deposit a significant fraction of the target yield in the jets, so that the neutron fluence seen by the first wall can be accommodated by fast-fission nuclear-grade materials.

8.5.2 Visual Tsunami Ablation and Venting Modeling

In 2004, Lawrence Livermore proposed two different jet configurations. Fig. 8.14, a CAD drawing, shows the so-called “closed” geometry, with a symmetric array of jets regularly

spaced. Fig. 8.15 displays the Visual Tsunami model of the same chamber, once the CAD

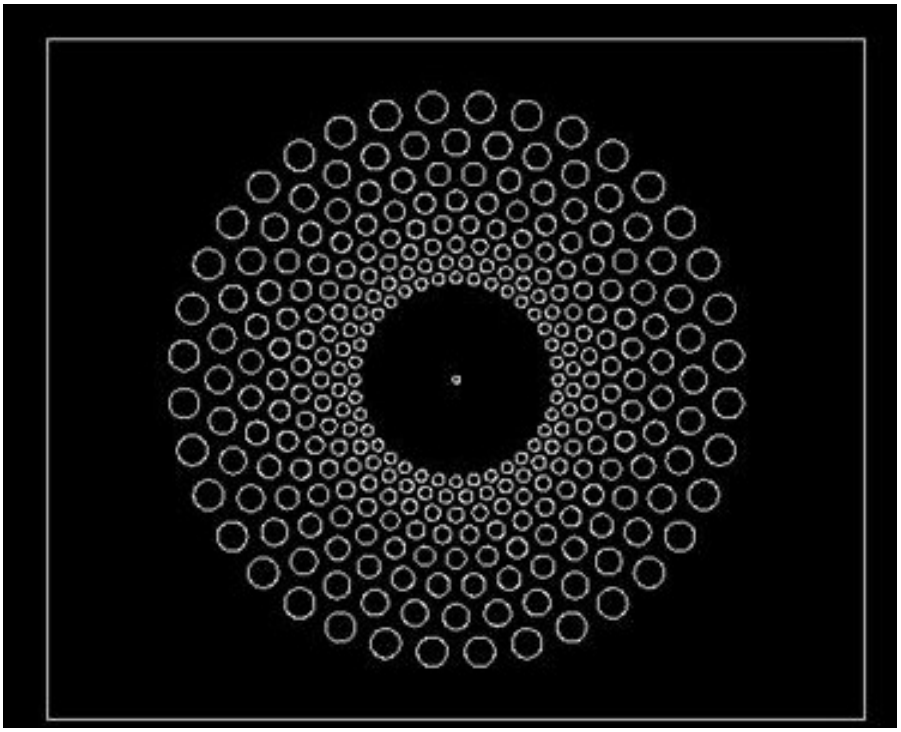

Figure 8.14: Two-dimensional cutaway view of LLNL's 2004 "closed" configuration.

drawing has been processed by the Visual Tsunami mesher and before ray-tracing is performed and ablation profiles are computed. It is assumed that there is no non-condensable background gas and that the recyclable transmission line is made of frozen flibe. The simulation was performed in Cartesian coordinates with an ideal gas law, no radiation transport, and reflective boundaries at gas/liquid interfaces. Snapshots of density and pressure contour plots are shown in Figures 8.16 and 8.17, respectively.

Figure 8.18 illustrates LLNL's 2004 "somewhat open" geometry, which is based on the "closed" geometry, with a few jets removed. Fig. 8.19 shows the open configuration, as modeled by Visual Tsunami. Snapshots of density and pressure contour plots are shown in Figures 8.20 and 8.21, respectively.

Visual Tsunami predicts (peak) impulse loads close to 10^6 Pa s for both the close and open

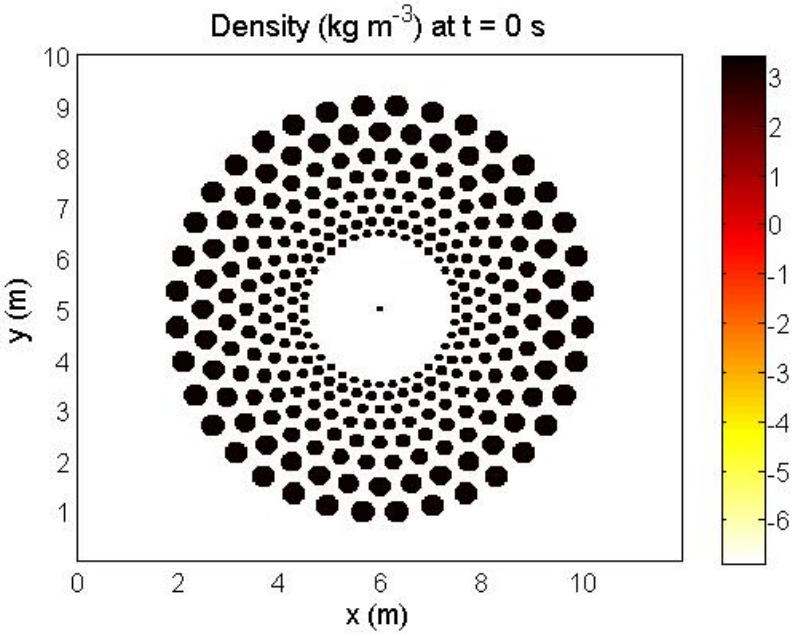

Figure 8.15: Visual Tsunami geometrical model of LLNL's 2004 "closed" configuration.

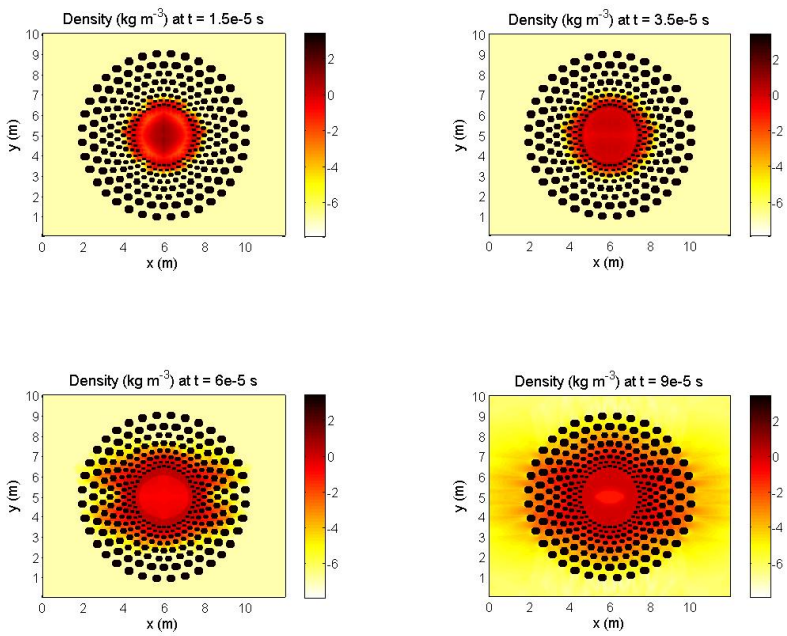

Figure 8.16: Density contour plots for the "closed" case.

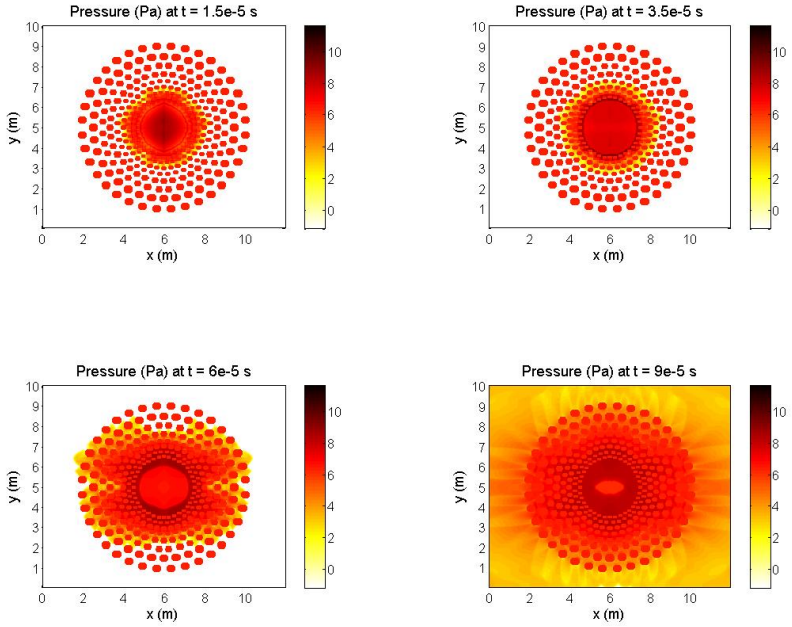

Figure 8.17: Pressure contour plots for the “closed” case.

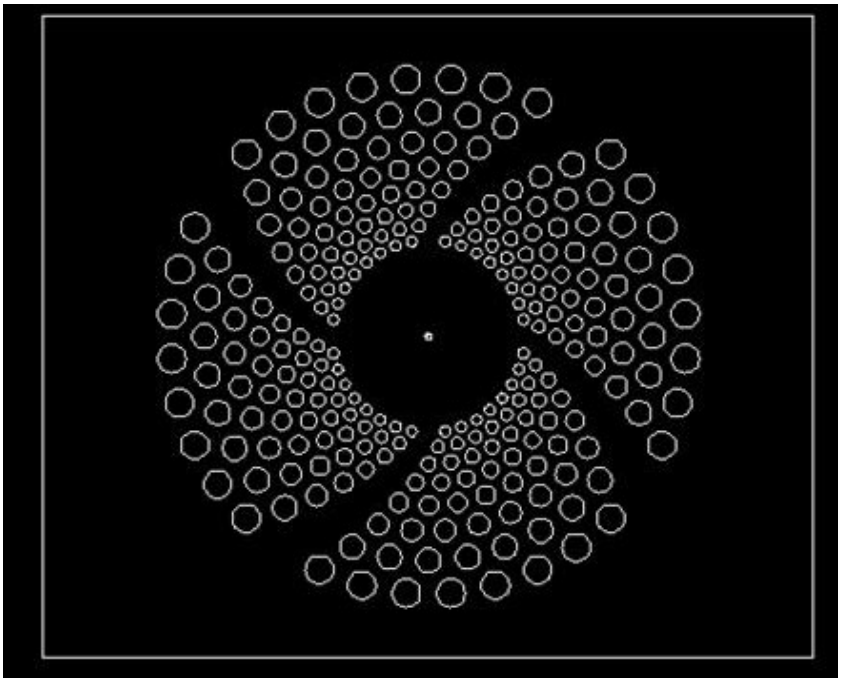

Figure 8.18: Two-dimensional cutaway view of LLNL’s 2004 “open” configuration.

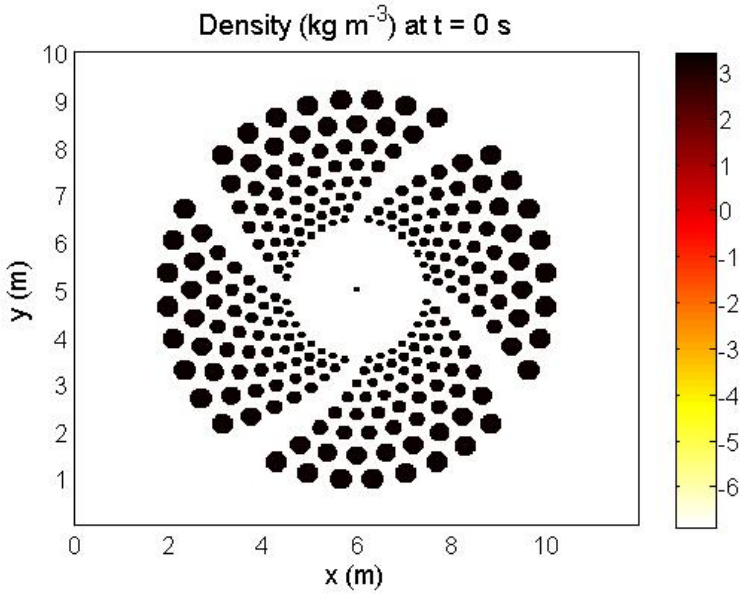

Figure 8.19: Visual Tsunami geometrical model of LLNL's 2004 "open" configuration.

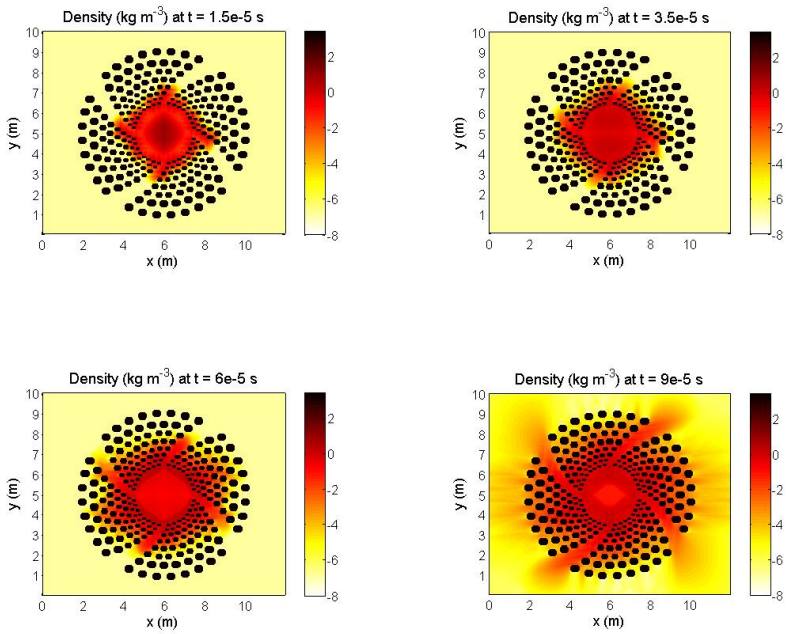

Figure 8.20: Density contour plots for the "open" case.

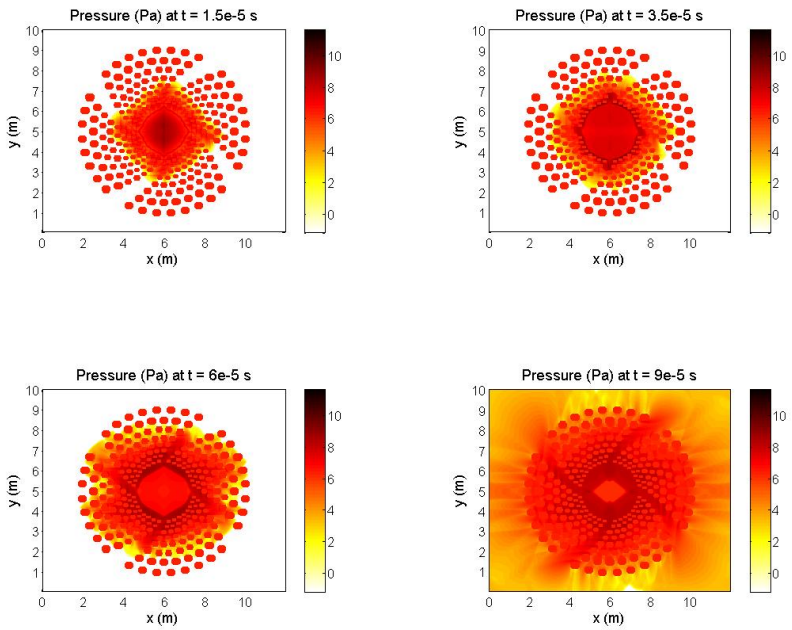

Figure 8.21: Pressure contour plots for the “open” case.

configurations, as can be seen in Fig. 8.22. While these simulations do not take into account three-dimensional effects and are expected to be conservative, more design work is required to bring down the impulse load to a reasonable value.

8.5.3 On-Going Optimization

The closed and somewhat open configurations are reminiscent of the original HYLIFE chamber, which had limited success in terms of gas density and pressure control. Fig. 8.23 shows the jet configuration proposed by Livermore in 2005. This geometry might be slightly more attractive from a fast debris venting and pressure build-up mitigation point of view. Turning the jets on and off so that when the fusion pellet explodes there will be a large venting opening at the bottom of the chamber may constitute a promising approach to controling the

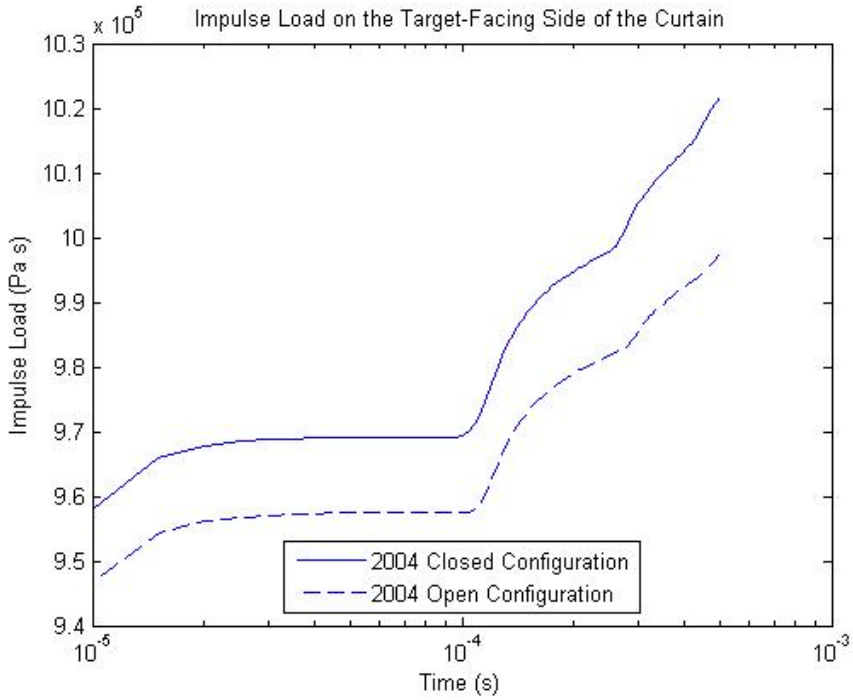

Figure 8.22: Impulse load to the liquid curtain in the “closed” and “open” Z-IFE chambers.

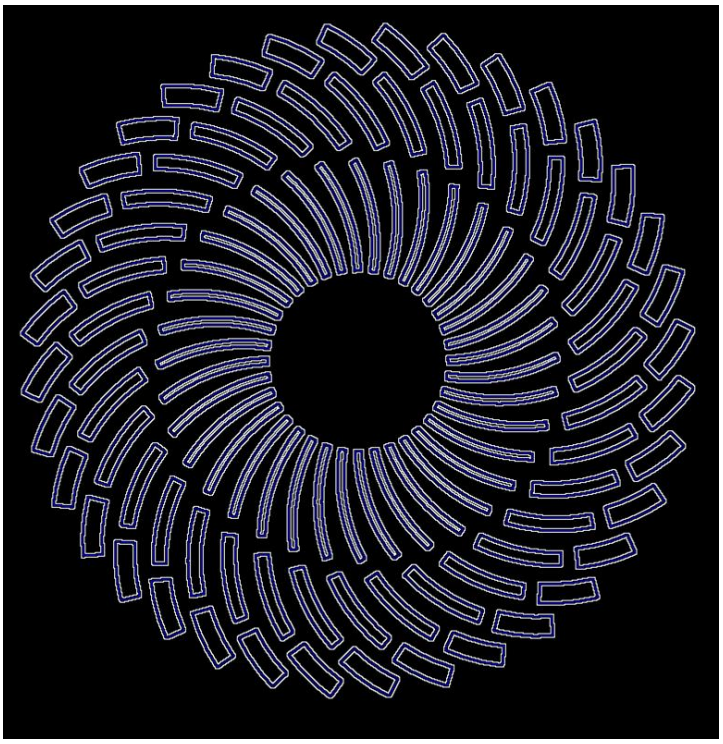

Figure 8.23: Two-dimensional cutaway view of LLNL’s 2005 configuration (courtesy of R.P. Abbott, LLNL).

gas pressure inside the liquid curtain and prevent too high an impulse loading.

8.6 Conclusions and Perspectives

TSUNAMI was modified to model gas dynamics phenomena in two HYLIFE-II-like thick-liquid chambers, one tailored for neutralized ballistic tranport, and the other compatible with the assisted-pinch scheme. The TSUNAMI simulations were the first to include the whole target chamber and beam lines. They indicated that liquid structures would not be sufficient to prevent any debris ingression up the beam lines and showed the need for the magnetic shutters in the case of neutralized ballistic transport. TSUNAMI and LSP simulations do indicate that liquid structures and magnetic shutters can be successfully combined to prevent debris ingression up the beam lines. Additionally, for both the neutralized ballistic and assisted-pinch chamber, TSUNAMI predicts impulse loads to liquid pockets that can be managed.

Future work could include revisiting these simulations employing Visual Tsunami. In particular, higher-fidelity simulations of the assisted-pinch chamber may need to take into account the x-ray and ion energy deposition in the background gas. Additional Z-IFE simulations should be performed and design changes made until a thick-liquid chamber that does not generate excessive impulse load is finalized. Modeling the impulse load to the top structures that hold the retransmission line would be valuable as well. This could be done with a 2-D simulation (in cylindrical coordinates) or with a 3-D model. Simulations for any IFE concept would benefit from multi-dimensional radiation hydrodynamics models of target and hohlraum disassembly.

Chapter 9

Conclusion

9.1 Simulation Code Development

The TSUNAMI series of gas dynamics codes has been well known in the fusion community for the last fifteen years or so. This doctoral work produced two simulation codes. The first one, TSUNAMI 2.8, is an improved version of TSUNAMI 2.6. The second code, Visual Tsunami, was written from scratch, building on the experience accumulated using TSUNAMI 2.8. The two versions of Visual Tsunami were developed using a host of modern programming techniques and improved algorithms. Emphasis was put on reaching those two always elusive goals of reusability and user-friendliness. Visual Tsunami is object-oriented, vectorized, and ready to be parallelized. The preprocessor and postprocessor provide a user-friendliness unheard of in the history of the code. They can help set up new simulations in a short amount of time and with a reduced likelihood of errors.

The gas dynamics scheme is still based on a Godunov scheme, with an exact solver to the exact Riemann problem, for both ideal and real gas equations of state—this is a first in the his-

tory of the code. Second-order accurate schemes are particularly useful with coarse meshes, which can rarely be employed with complex geometries; a first order Godunov scheme was deemed sufficient. The two-temperature radiation diffusion mathematical model is similar to that used by Chen in his 1-D version of TSUNAMI. The discrete scheme, however, is significantly more accurate. (Its detailed multi-dimensional implementation was left for future work.) The novel gas/liquid interface model is conceptually simpler than the traditional TSUNAMI model, first derived by Liu. Detailed comparison between the two models is left for future work. The new ablation model with radiation conduction and hot opacities surpasses the traditional instantaneous cohesive energy model. Future modifications could include an in-flight condensation model and a shift to unstructured meshes.

The improved TSUNAMI code was employed in support of the heavy-ion fusion Robust and Modular Point Designs and the conception of the first Condensation Debris Experiments. Additionally, Visual Tsunami was recently used for CDE and the novel thick-liquid protected Z-IFE target chamber.

9.2 Design and Modeling of the Condensation Debris Experiments

As described, the Condensation Debris Experiments investigate in-flight condensation of superheated gaseous mixtures. Back-of-the-envelope estimates, simple models, and simulations assisted in the design of the series of Condensation Debris Experiments, guided the dimensioning of the chamber, hinted at the scientific feasibility of the experiments, and helped in interpreting the results. For the sake of brevity, only a few highlights were reported in this

doctoral dissertation.

Due to the novelty of the experiment and the uncertitude in gas dynamics initial conditions resulting from the interaction of the laser beam with the halfraum, a qualitative agreement was sought after. Comparison between simulation and experimental results do show good qualitative agreement.

Future work should include implementing a detailed in-flight condensation model and the simulation of the proposed experimental campaign on the National Ignition Facility at the Lawrence Livermore National Laboratory. Since the energy density will be higher, inclusion of radiation and accurate gas/solid interaction models will then be essential.

9.3 Gas Transport and Control in Thick-Liquid Inertial Fusion Target Chambers

Due to the arrangement of numerous liquid jets, shock propagation through HYLIFE-II-type chambers is far more complex than in dry-wall or thin-liquid IFE chambers. In a thick-liquid chamber, indirect-drive target x-rays ablate a thin layer off the surface of the inner pocket; fast ions quickly deposit their energy in the ablated gas; and slow target debris interacts with the expanding ablated layer. A complex pattern of reflected and transmitted waves is then generated, in which waves can be transmitted through the jet structures, or reflected off the inner liquid pocket or other waves. The gas ultimately vents through the various thick-liquid jets, filling the volume of the target chamber.

During the course of the HYLIFE study, it was realized that a closed pocket (besides leaving no room for target or driver propagation!) would result in an excessive pressurization

of the inside pocket and the liquid curtain being slammed into the structural first wall. Both HYLIFE-II and the RPD rely on oscillating slab jets with venting openings to avoid pocket over-pressurization. Another crucial issue is the propagation of target and ablated gas up the beam lines where it could deposit and cause arcing between the still un-neutralized beam and the tube wall. Although pockets can be designed to maximize gas venting in directions opposite to the beam line, this doctoral work helped recognize that this approach would not be effective enough. As mechanical shutters are too slow to close off the beam lines quickly enough, a cold flinabe liquid vortex layer was suggested to coat and protect the beam line near the target chamber. TSUNAMI showed that it could not be long enough for all the debris and ablated molten salt to condense. The combination of an ionizing plasma and a weak magnetic dipole was proposed to effectively stop the debris and prevent its ingression past the vortex. The dipole will prevent the neutralizing electrons from streaming up the beam line as well, hence limiting beam emittance growth. Additionally, this work helped recognize that the cold vortex acts as an excellent getter and prevents blowing-up of target chamber background gas up the beamlines. This work was incorporated into the Robust Point Design, the first heavy-ion fusion conceptual design, with a driver, a target, and a chamber, that are self-consistent with one another.

This doctoral work supported preliminary work towards a modular point design, a potentially cheaper alternative to the Robust Point Design. The first multidimensional modeling of the assisted-pinch chamber was performed, but a detailed model may need to include the deposition of target x-rays in the background gas of the target chamber. (The gas density is much higher than in the RPD resulting in a photon mean free path of order of the standoff distance of the pocket.) Design questions raised by the novel vortex chamber were explored as well.

The first multidimensional simulation of a Z-IFE target chamber was performed. Future work should investigate improved liquid blanket configurations that would increase the venting rate and minimize the impulse load transmitted to the jets.

Bibliography

[1] R. Abbott, S. Pemberton, P.F. Peterson, G.-P. Sun, P. Wright, R. Holmes, J. Latkowski, R. Moir, and K. Springer. Cylindrical liquid jet grids for beam-port protection of thick-liquid heavy-ion fusion target chambers. *Fusion Technology*, 39(2):732–738, March 2001.

[2] A.T. Anderson. *X-Ray Ablation Measurements and Modeling for ICF Applications*. PhD thesis, University of California at Berkeley, 1996.

[3] A.T. Anderson, A.K. Burnham, M.T. Tobin, and P.F. Peterson. Modeling and experiments of x-ray ablation of National Ignition Facility first wall materials. *Fusion Technology*, 30(3):757–763, 1996.

[4] R.C. Arnold. Heavy-ion beam inertial-confinement fusion. *Nature*, 276:19–23, November 1978.

[5] R.Y. Bai and V.E. Schrock. An approximate method for analyzing transient condensation on spray in HYLIFE-II. *Fusion Technology*, 19:732–739, May 1991.

[6] P.M. Bardet, C.S. Debonnel, J. Freeman, G. Fukuda, B. Supiot, and P.F. Peterson. Dynamics of liquid-protected fusion chambers. *Fusion Science and Technology*, 47:626–632, April 2005.

[7] P.M. Bardet, B.F. Supiot, P.F. Peterson, and O. Savas. Liquid vortex shielding for fusion energy applications. *Fusion Science and Technology*, 47:1192–1196, May 2005.

[8] P. Calderoni. *On the study of vapor condensation for the assessment of Inertial Fusion Energy liquid chamber clearing*. PhD thesis, University of California at Los Angeles, 2004.

[9] D.A. Callahan-Miller and M. Tabak. A distributed radiator, heavy ion target driven by Gaussian beams in a multibeam illumination geometry. *Nuclear Fusion*, 39(7):883–891, 1999.

[10] D.A. Callahan-Miller and M. Tabak. Progress in target physics and design for heavy ion fusion. *Physics of Plasmas*, 7(5):2083–2091, May 2000.

[11] X.M. Chen. *A Study of Thermal Hydraulic and Kinetic Phenomena in HYLIFE-II—An Inertial Confinement Fusion Reactor*. PhD thesis, University of California at Berkeley, 1992.

[12] X.M. Chen, J.C. Liu, P.F. Peterson, V.E. Schrock, and J.M. Scott. *Code Description Document, TSUNAMI 2.6: A Program for Predicting Gas Dynamics in Inertial Fusion Energy Target Chambers*, October 1998.

[13] X.M. Chen, P.F. Peterson, and M.T. Tobin. TSUNAMI analysis of National-Ignition-Facility 2-D gas dynamics phenomenon. *Fusion Technology*, 26(3):814–818, March 1994.

[14] X.M. Chen, V.E. Schrock, and P.F. Peterson. The calculation of the kinetic rate constants for LiF and BeF_2. *Fusion Technology*, 21(3):1536–1540, May 1992.

[15] X.M. Chen, V.E. Schrock, and P.F. Peterson. The soft-sphere equation of state for liquid Flibe. *Fusion Technology*, 21(3):1525–1530, May 1992.

[16] X.M. Chen, V.E. Schrock, and P.F. Peterson. Coupling of radiation transport with the gas-dynamics for HYLIFE-II analysis. *Fusion Technology*, 26(3):906–911, November 1994.

[17] X.M. Chen, V.E. Schrock, and P.F. Peterson. Fitted equations of state for Flibe gas. *Fusion Technology*, 26(3):912–916, November 1994.

[18] X.M. Chen, V.E. Schrock, P.F. Peterson, and P. Colella. Gas-dynamics in the central cavity of the HYLIFE-II reactor. *Fusion Technology*, 21(3):1520–1524, May 1992.

[19] P. Colella and H.M. Glaz. Efficient solution algorithms for the Riemann problem for real gases. *Journal of Computational Physics*, 59:264–289, 1985.

[20] P. Colella and P.R. Woodward. The piecewise parabolic method (PPM) for gas-dynamics simulations. *Journal of Computational Physics*, 54:174–201, 1984.

[21] D.E. Cullen. PROGRAM EPICSHOW a computer code to allow interactive viewing of the EPIC data libraries (version 2002-1). Technical report, Lawrence Livermore National Laboratory, 2002. UCRL-ID-126455.

[22] D.E. Cullen, J.H. Hubbell, and L. Kissel. EPDL97: the Evaluated Photon Data Library, '97 version. Technical report, Lawrence Livermore National Laboratory, 1997. UCRL-50400.

[23] R.C. Davidson, B.G. Logan, J.J. Barnard, F.M. Bieniosek, R.J. Briggs, D.A. Callahan, M. Kireeff Covo, C.M. Celata, R.H. Cohen, J.E. Coleman, C.S. Debonnel, D.P. Grote,

P.C. Efthimion, S. Eylon, A. Friedman, E.P. Gilson, L.R. Grisham, E. Henestroza, I.D. Kaganovich, J.K. Kwan, E.P. Lee, W.W. Lee, M. Leitner, S.M. Lund, W.R. Meier, A.W. Molvik, C.L. Olson, G.E. Penn, H. Qin, P.K. Roy, D.V. Rose, A. Sefkow, P.A. Seidl, W.M. Sharp, E.A. Startsev, M. Tabak, C. Thoma, J.-L. Vay, W.L. Waldron, J.S. Wurtele, D.R. Welch, G.A. Westenskow, and S.S. Yu. US heavy ion beam research for high energy density physics applications and fusion. In *Proceedings of the fourth international conference on inertial fusion sciences and applications (IFSA)*, Biarritz, France, September 2005.

[24] C.S. Debonnel, G.T. Fukuda, P.M. Bardet, and P.F. Peterson. Control of the heavy-ion beam line gas pressure and density in the HYLIFE thick-liquid chamber. *Fusion Engineering and Design*, 63-64:647–652, 2002.

[25] C.S. Debonnel, T.X. Wang, M. Suzuki, E. Garcia, and P.F. Peterson. Visual Tsunami: A versatile, user-friendly, multidimensional ablation and hydrodynamics design code. *Fusion Science and Technology*, 47(4):1165–1169, May 2005.

[26] C.S. Debonnel, D.R. Welch, D.V. Rose, S.S. Yu, and P.F. Peterson. Gas transport and density control in the HYLIFE heavy-ion beam lines. *Fusion Science and Technology*, 43(3):408–413, May 2003.

[27] C.S. Debonnel, S.S. Yu, and P.F. Peterson. X-ray ablation and debris venting for the heavy-ion point design. *Fusion Science and Technology*, 44(2):274–278, 2003.

[28] C.S. Debonnel, S.S. Yu, and P.F. Peterson. Progress towards thick liquid fusion chambers for assisted-pinch and solenoid focusings. *Nuclear Instruments and Methods in Physics Research A*, 544:342–346, 2005.

[29] B. Einfeldt, C.D. Munz, P.L. Roe, and B. Sjögreen. On Godunov-type methods near low densities. *Journal of Computational Physics*, 92:273–295, 1991.

[30] J.J. Gottlieb and C.P.T. Groth. Assessment of Riemann solvers for unsteady one-dimensional inviscid flows of perfect gases. *Journal of Computational Physics*, 78:437–458, 1988.

[31] P.A. House. HYLIFE-II reactor chamber mechanical design. *Fusion Technology*, 21(3):1487–1491, May 1992.

[32] C. Jantzen, E.P. Lee, and P.F. Peterson. Parametric studies of ablation and venting from the central cavity of the HYLIFE-II reactor. *Fusion Technology*, 34(3):1047–1052, November 1998.

[33] C. Jantzen and P.F. Peterson. Scaled impulse loading for liquid hydraulic response in IFE thick-liquid chamber experiments. *Nuclear Instruments and Methods in Physics Research A*, 464:404–409, 2001.

[34] C.A. Jantzen. *Gas Dynamics and Radiative Heat Transfert in IFE Chambers with Emphasis on the HYLIFE-II Design*. PhD thesis, University of California at Berkeley, 2000.

[35] J. Abdallah Jr and R.E.H. Clark. TOPS: A multigroup opacity code. Technical report, Los Alamos National Laboratory, 1985. LA-10454.

[36] Y. Kozaki, M. Kabetani, H. Nagatomo, K. Yamamoto, H. Furukawa, K. Mima, S. Nakai, and T. Yamanaka. Simulation study on evacuation of metal vapor in laser fusion liquid wall chamber. *Fusion Engineering and Design*, 60(1):77–83, January 2002.

[37] R. Linford, R. Betti, J. Dahlburg, J. Asay, M. Campbell, P. Colella, J. Freidberg, J. Goodman, D. Hammer, J. Hoagland, S. Jardin, J. Lindl, G. Logan, K. Matzen, G. Navratil, A. Nobile, J. Sethian, J. Sheffield, M. Tillack, and J. Weisheit. A review of the U.S. Department of Energy's inertial fusion energy program. *Journal of Fusion Energy*, 22(2):93–126, June 2003.

[38] J.C. Liu. *Experimental and Numerical Investigation of Shock Wave Propagation Through Complex Geometry, Gas Continuous, Two-Phase Media*. PhD thesis, University of California at Berkeley, 1993.

[39] J.C. Liu, P. Colella, P.F. Peterson, and V.E. Schrock. Modeling supersonic flows through a gas-continuous 2-fluid medium. *Nuclear Engineering and Design*, 146(1-3):337–348, February 1994.

[40] J.C. Liu, P.F. Peterson, and V.E. Schrock. Blast venting through blanket material in the HYLIFE ICF reactor. *Fusion Technology*, 21(3):1514–1519, May 1992.

[41] X. Luo, M. Ni, A. Ying, and M. Abdou. Modeling for free surface flow with phase change. *Fusion Science and Technology*, 47:1187–1191, May 2005.

[42] S.P. Lyon and J.D. Johnson. SESAME: The Los Alamos National Laboratory equation of state database. Technical report, Los Alamos National Laboratory, 1992. LA-UR-92-3407.

[43] R.W. Moir. HYLIFE-II inertial confinement fusion reactor design. *Fusion Technology*, 19(3):617–624, May 1991.

[44] R.W. Moir. HYLIFE-II inertial fusion energy power plant design. *Fusion Technology*, 21(3):1475–1486, May 1992.

[45] R.W. Moir, R.L. Bieri, X.M. Chen, T.J. Dolan, M.A. Hoffman, P.A. House, R.L. Leber, J.D. Lee, Y.T. Lee, J.C. Liu, G.R. Longhurst, W.R. Meier, P.F. Peterson, R.W. Petzoldt, V.E. Schrock, M.T. Tobin, and W.H. Williams. HYLIFE-II: A molten-salt inertial fusion energy power plant design—final report. *Fusion Technology*, 25(1):5–25, January 1994.

[46] C.B. Moler. *Numerical computing with MATLAB*. Society for Industrial and Applied Mathematics, Philadelphia, 2004.

[47] G.A. Moses and R.R. Peterson. Computer modeling of ICF target chamber phenomena. *Laser and Particle Beams*, 12(2):125–162, 1994.

[48] C.L. Olson. Chamber transport. *Nuclear Instruments and Methods in Physics Research A*, 464:118–125, 2001.

[49] S. Pemberton, C. Jantzen, J. Kuhn, and P.F. Peterson. Partial pocket experiments for IFE thick-liquid pocket disruption and clearing. *Fusion Technology*, 39(2):726–731, March 2001.

[50] S.J. Pemberton, R.P. Abbott, and P.F. Peterson. Annular vortex generation for inertial fusion energy beam-line protection. *Fusion Science and Technology*, 43(3):378–383, 2003.

[51] S.J. Pemberton, R.P. Abbott, and P.F. Peterson. Thick-liquid blanket configuration and response for the HIF point design. *Fusion Science and Technology*, 44(2):294–299, September 2003.

[52] P.F. Peterson. Design methods for thick-liquid protection of inertial fusion chambers. *Fusion Technology*, 39(2):702–710, 2001.

[53] P.F. Peterson. HIF liquid hydraulics scaling and pocket design. *Nuclear Instruments and Methods in Physics Research A*, 464:159–164, 2005.

[54] P.F. Peterson and J.M. Scott. The mini-chamber, an advanced protection concept for NIF. *Fusion Technology*, 30(3):442–447, December 1996.

[55] R.R. Peterson, J.J. MacFarlane, J.F. Santarius, P. Wang, and G.A. Moses. The BUCKY and ZEUS-2D computer codes for simulating high energy density ICF plasmas. *Fusion Technology*, 30:783–787, December 1996.

[56] R.W. Petzoldt. Oscillating liquid flow ICF reactor. *Fusion Technology*, 19(3):758–762, May 1991.

[57] J. Pike. Riemann solvers for perfect and near-perfect gases. *AIAA Journal*, 31(10):1801–1808, October 1993.

[58] A.R. Raffray, W. Meier, S. Abdel-Khalik, R. Bonazza, P. Calderoni, C.S. Debonnel, Z. Dragojlovic, L. El-Guebaly, D. Haynes, J. Latkowski, C. Olson, P.F. Peterson, S. Reyes, P. Sharpe, M.S. Tillack, and M. Zaghloul. IFE thick liquid wall chamber dynamics: Governing mechanisms and modeling and experimental capabilities. *Fusion Science and Technology*, 49:1–27, January 2006.

[59] D.V. Rose, D.R. Welch, C.L. Olson, S.S. Yu, S. Neff, W.M. Sharp, and ARIES-IFE team. Impact of beam transport method on chamber and driver design for heavy ion inertial fusion energy. *Fusion Science and Technology*, 46:470–493, November 2004.

[60] R. Saurel, M. Larini, and J.C. Loraud. Exact and approximate Riemann solvers for real gases. *Journal of Computational Physics*, 112:126–137, 1994.

[61] R.W. Schrage. *A theoretical study of interphase mass transfer*. Columbia University Press, New York, 1953.

[62] V.E. Schrock, P.F. Peterson, and R.Y. Bai. A gas dynamic choking phenomenon in early time intense transient condensation. *Nuclear Engineering and Design*, 139:127–140, 1993.

[63] J.M. Scott. *X-Ray Ablated Plumes in Inertial Confinement Fusion Reactors*. PhD thesis, University of California at Berkeley, 1998.

[64] J.M. Scott and P.F. Peterson. Chamber-protection issues for near-target experiments in NIF. *Fusion Technology*, 34(3):772–776, November 1998.

[65] J.M. Scott, P.F. Peterson, and A. Burnham. Experimental and analytical studies of louvered first-wall systems for NIF. *Fusion Technology*, 34(3):459–463, November 1998.

[66] S.M. Senn, S.J. Pemberton, and P.F. Peterson. Nonsinusoidal nozzle oscillation functions for generating thick-liquid pockets for heavy-ion fusion chambers. *Fusion Science and Technology*, 45(4):573–582, June 2004.

[67] G.A. Sod. A survey of several finite difference methods for systems of nonlinear hyperbolic conservation laws. *Journal of Computational Physics*, 27:1–31, 1978.

[68] G. Strang. On the construction and comparison of difference schemes. *SIAM Journal on Numerical Analysis*, 5(3):506–517, September 1968.

[69] M. Tabak, D. Callahan-Miller, D.D.-M. Ho, and G.B. Zimmerman. Design of a distributed radiator target for inertial fusion driven from two sides with heavy ion beams. *Nuclear Fusion*, 38(4):509–513, 1998.

[70] M.S. Tillack and N. Basu. Simulation of gas dynamic behavior in dry-wall inertial fusion energy chambers. In *Proceedings of the 18th IEEE/NPSS symposium on fusion engineering*, San Diego, CA, October 1999.

[71] E.F. Toro. A fast Riemann solver with constant covolume applied to the random choice method. *International Journal for Numerical Methods in Fluids*, 9:1145–1164, 1989.

[72] E.F. Toro. *Riemann Solvers and Numerical Methods for Fluid Dynamics: A Practical Introduction*. Springer-Verlag, New York, 1997.

[73] B. van Leer. Towards the ultimate conservative difference scheme. V. A second-order sequel to Godunov's method. *Journal of Computational Physics*, 32:101–136, 1979.

[74] P. Vieille. Sur les discontinuités produites par la détente brusque de gaz comprimés. *Comptes Rendus des Séances de l'Académie des Sciences*, 129:1228–1230, 1899.

[75] P. Woodward and P. Colella. The numerical simulation of two-dimensional fluid flow with strong shocks. *Journal of Computational Physics*, 54:115–173, 1984.

[76] S. Yu, S. Eylon, T. Fessenden, E. Henestroza, R. Lafever, W. Leemans, R. Petzoldt, D. Ponce, M. Vella, R.W. Moir, W.M. Sharp, R. Peterson, M. Sawan, and A. Tauschwitz. Plasma-channel-based reactor and final transport. *Nuclear Instruments and Methods in Physics Research A*, 415:174–181, 1998.

[77] S.S. Yu, R.P. Abbott, R.O. Bangerter, J.J. Barnard, R.J. Briggs, D. Callahan, C.M. Celata, R. Davidson, C.S. Debonnel, S. Eylon, A. Faltens, A. Friedman, D.P. Grote, P. Heitzenroeder, E. Henestroza, I. Kaganovich, J.W. Kwan, J.F. Latkowaki, E.P. Lee, B.G. Logan, P.F. Peterson, D. Rose, P.K. Roy, G.-L. Sabbi, P.A. Seidl, W.M. Sharp, and D.R. Welch. Heavy ion fusion (HIF) driver point designs. *Nuclear Instruments and Methods in Physics Research A*, 544:294–299, 2005.

[78] S.S. Yu, J.J. Barnard, R.J. Briggs, D. Callahan-Miller, L.L. Chao, R. Davidson, C.S. Debonnel, S. Eylon, A. Friedman, E. Henestroza, I. Kaganovich, J.W. Kwan, E.P. Lee, M. Leitner, B.G. Logan, W. Meier, P.F. Peterson, L. Reginato, D. Rose, P. Roy, W. Waldron, and D.R. Welch. Towards a modular point design for heavy ion fusion. *Fusion Science and Technology*, 47(3):621–625, April 2005.

[79] S.S. Yu, W.R. Meier, R.P. Abbott, J.J. Barnard, T. Brown, D.A. Callahan, C. Debonnel, P. Heitzenroeder, J.F. Latkowski, B.G. Logan, S.J. Pemberton, P.F. Peterson, D.V. Rose, G.-L. Sabbi, W.M. Sharp, and D.R. Welch. An updated point design for heavy ion fusion. *Fusion Science and Technology*, 44(2):266–273, 2003.

[80] M.R. Zaghloul. A consistent model for the equilibrium thermodynamic functions of partially ionized flibe plasma with Coulomb corrections. *Physics of Plasmas*, 10(2):527–538, February 2003.

[81] M.R. Zaghloul. Ionization equilibrium and partition functions of high-temperature weakly non-ideal Flibe gas. *Journal of Physics D: Applied Physics*, 36:2249–2254, September 2003.

[82] M.R. Zaghloul. Ionization equilibrium and partition functions of high-temperature

weakly non-ideal Flibe gas. *Fusion Science and Technology*, 44:338–343, September 2003.

[83] M.R. Zaghloul. Equation of state of high-temperature weakly nonideal Flinabe (LiF-NaF-BeF_2) gas. *Fusion Science and Technology*, 49:28–38, January 2006.

[84] M.R. Zaghloul and A.R. Raffray. IFE liquid wall response to the prompt X-ray energy deposition: Investigation of physical processes and assessment of ablated material. *Fusion Science and Technology*, 47(1):27–45, January 2005.

[85] M.R. Zaghloul, D.K. Sze, and A.R. Raffray. Thermo-physical properties and equilibrium vapor-composition of lithium fluoride-beryllium fluoride (2LiF/BeF_2) molten salt. *Fusion Science and Technology*, 44:344–350, September 2003.

Appendix A

Flibe Properties

The molten salt flibe has been studied to some extent for various fission and fusion applications. A few of the thermal-physical properties that are among the most relevant for gas dynamics simulations are compiled here. In particular, a review of equations of state for real gas flibe is provided.

A.1 Miscellaneous Properties

Properties useful for gas dynamics simulations have been compiled and are presented in Table A.1. The molecular mass of liquid and gas flibe follows from the composition. The gas phase is assumed to be in thermodynamics and chemical equilibrium with its liquid counterpart.

property	value	comment	reference
Be molecular mass	9.012 g mol^{-1}		
F molecular mass	18.998 g mol^{-1}		
Li molecular mass	6.941 g mol^{-1}		
composition	2/3 LiF 1/3 BeF_2	liquid	[45]
molecular mass	40 g mol^{-1}	liquid	estimate
density (kg m^{-3})	2415.6 - 0.49072 T	T $\geq$ 732.2 K T $\leq$ 4498.8 K	[85]
cohesive energy e_c	7.8×10^6 J kg^{-1}	at 873 K	estimate
thermal diffusivity α	2×10^{-7} m^2 s^{-1}	liquid	estimate
heat capacity	$c_p \approx c_v \approx 2.3 \times 10^3$ J kg^{-1} K^{-1}	liquid	estimate
critical temperature	4498.8 K	liquid	[15]
composition	$>$ 99% BeF_2	gas	estimate
molecular mass	$\approx$ 47.2 g mol^{-1}	gas	

Table A.1: Various flibe properties.

A.2 Hydrodynamics Equations of State

Background information on hydrodynamics equations of state can be found in Section 3.2. The hydrodynamics equations of state in this section assume that the gas has the composition of liquid flibe.

A.2.1 Chen's Equations of State

Chen and co-workers [11, 14, 17] derived the first real gas equation of state for flibe. Their assumptions and methodology can be found elsewhere; here only the analytical formulae are presented. First, a non-dimensional energy y is defined:

$$y = \ln(\frac{e}{e_c}) \tag{A.1}$$

where e is the specific internal energy (J kg^{-1}) and e_c is the specific cohesive energy of flibe (J kg^{-1}). For this particular analytical fit, $e_c = 7.906 \times 10^6$ J kg^{-1}. The pressure p (Pa) is then

given by:

$$p = (\gamma_{\text{ideal}} - 1)\,\rho\,(e - e_c)\,g\,(y\,(e)) + \rho_0\,(\Gamma_0\,(e - e_v) - (\gamma_{\text{ideal}} - 1)\,(e - e_c)\,g\,(y\,(e)))\left(\frac{\rho}{\rho_0}\right)^{2.3} \tag{A.2}$$

where $\gamma_{\text{ideal}} = \frac{5}{3}$, $e_v = 8.508 \times 10^5$ J kg^{-1}, $\Gamma = 1.0$, $\rho_0 \approx 2000$ kg m^{-3} and the factor $g(y)$ is given by:

$$\begin{aligned} g(y) =& 1 - 0.79\exp\left(-0.32(y-1.27)^2\right) - 0.35\exp\left(-1.29(y-3.2)^2\right) \\ & - 0.6\exp\left(-0.39(y-5.02)^2\right) - 0.24\exp\left(-2.5(y-6.41)^2\right) \end{aligned} \tag{A.3}$$

The sound speed is evaluated using Eq. 3.42:

$$a^2 = \left(\frac{\partial p}{\partial \rho}\right)_e + \frac{p}{\rho^2}\left(\frac{\partial p}{\partial e}\right)_\rho \tag{A.4}$$

The gas temperature (K) is given by:

$$T = \frac{pM}{\rho R} \tag{A.5}$$

where R is the universal gas constant[1]. The molar mass M (kg mol^{-1}) is given as a function of specific internal energy by:

$$M = \begin{cases} 1.60036 - 0.170118\ln(e) + 0.00454296(\ln(e))^2 & \text{if } e \leq 10^8 \text{ J kg}^{-1} \\ 0.109337 - 0.0088785\ln(e) + 0.000377312(\ln(e))^2 & \text{if } e \geq 10^8 \text{ J kg}^{-1} \end{cases} \tag{A.6}$$

The second equation has a typographical error as pointed out independently by Debonnel (personal communication to G. Fukuda, UCB) and Zaghloul. The equation has been corrected by Zaghloul [80] and now reads:

$$M = \begin{cases} 1.60036 - 0.170118\ln(e) + 0.00454296(\ln(e))^2 & \text{if } e \leq 10^8 \text{ J kg}^{-1} \\ 0.109337 - 0.0088785\ln(e) + 0.000183843126(\ln(e))^2 & \text{if } e \geq 10^8 \text{ J kg}^{-1} \end{cases} \tag{A.7}$$

[1] R=8.31 J mol^{-1} K^{-1}

For e of order 10^{11} J kg^{-1}, Eq. A.6 overestimates M and subsequently T by two orders of magnitude. (In other words, the ideal gas law predicts a more accurate peak temperature than the uncorrected Chen's real gas caloric equation of state!)

A.2.2 Jantzen's Equations of State

Jantzen [34] adapted Zel'dovich and Raizer's thermodynamics treatment of ionization phenomena. An outline of her work can be found in her thesis [34]. For her simulations of gas dynamics phenomena in inertial fusion energy systems, she kept Chen's EOS in the dissociation regime and used hers at higher temperatures, at which the gas is ionized.

A.2.3 Zaghloul's Equations of State

Zaghloul derived an equation of state for flibe in the ionization regime [80, 81, 82] (at temperatures greater than 1 eV.) Chen made a few oversimplifying assumptions and Zaghloul's approach is substantially more generic and accurate, as discussed in Ref. [80]. Fig. A.1 displays flibe temperature as a function of density and specific energy. (Zaghloul provided the specific energy as a function of density and temperature. Inverse interpolation was performed to generate Fig. A.1.) Fig. A.2 and Fig. A.3 show pressure and sound speed as functions of density and temperature. In addition, Zaghloul provided the adiabatic exponent, heat capacity at constant pressure, and average ionization state, which are displayed on Fig. A.4, Fig. A.5, and Fig. A.6, respectively.

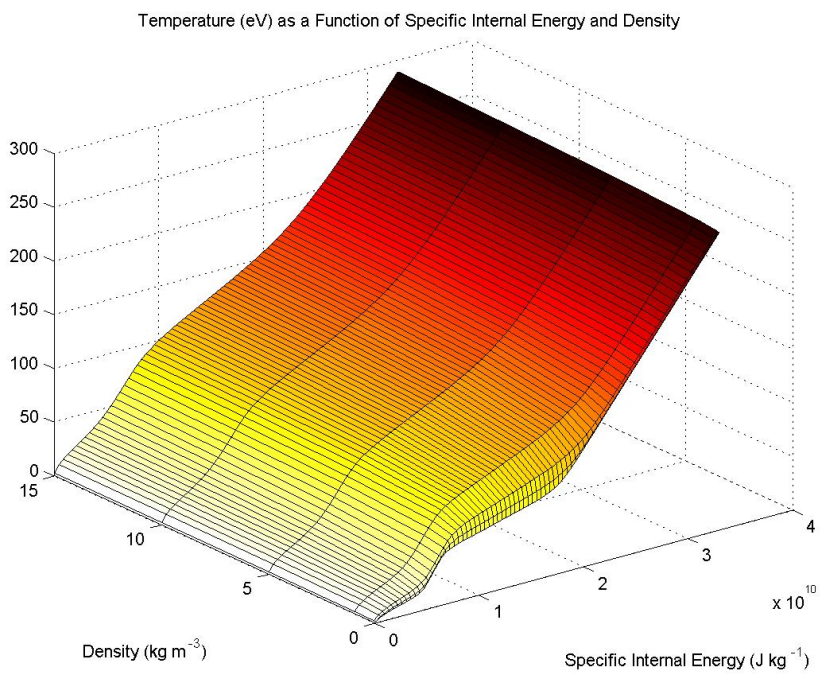

Figure A.1: Flibe pressure as a function of density and specific energy.

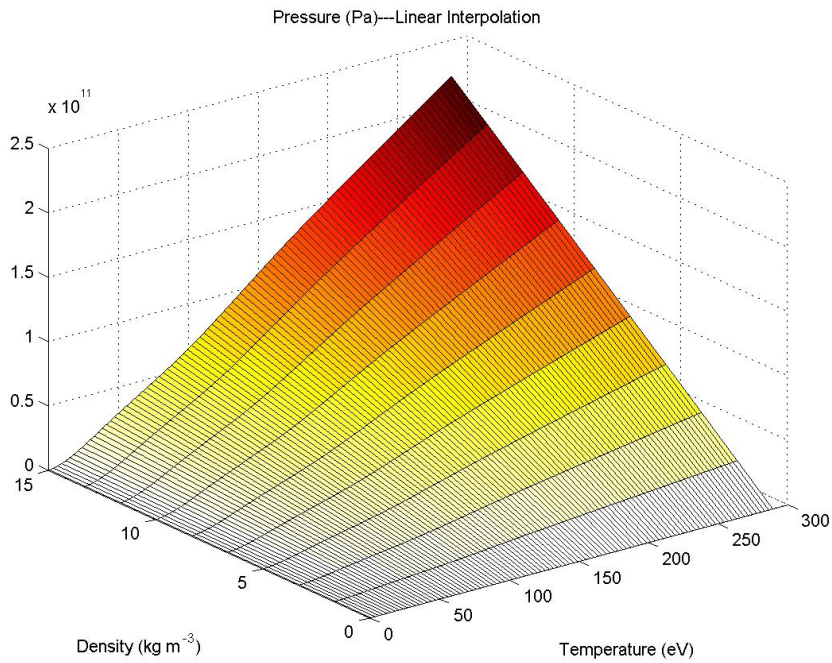

Figure A.2: Flibe pressure as a function of density and temperature.

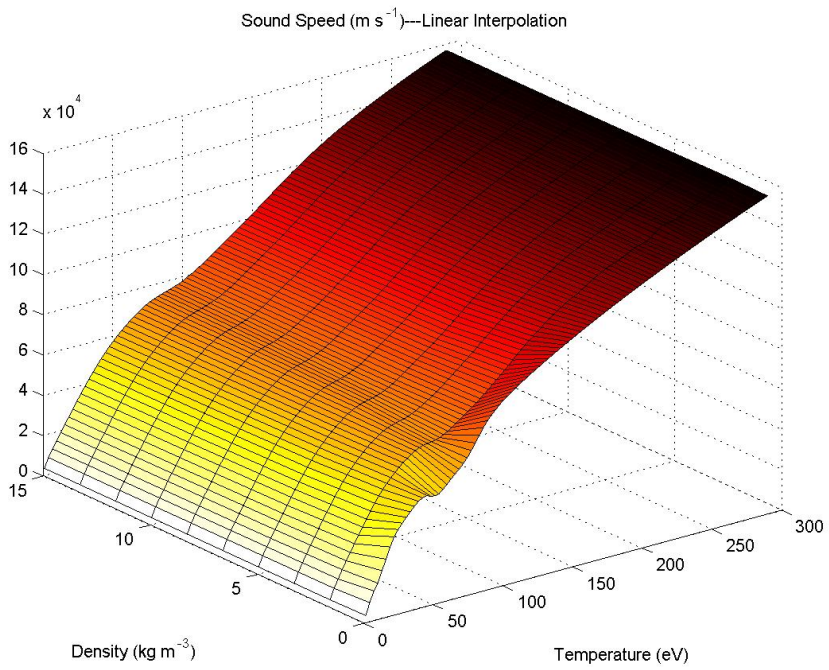

Figure A.3: Flibe sound speed as a function of density and temperature.

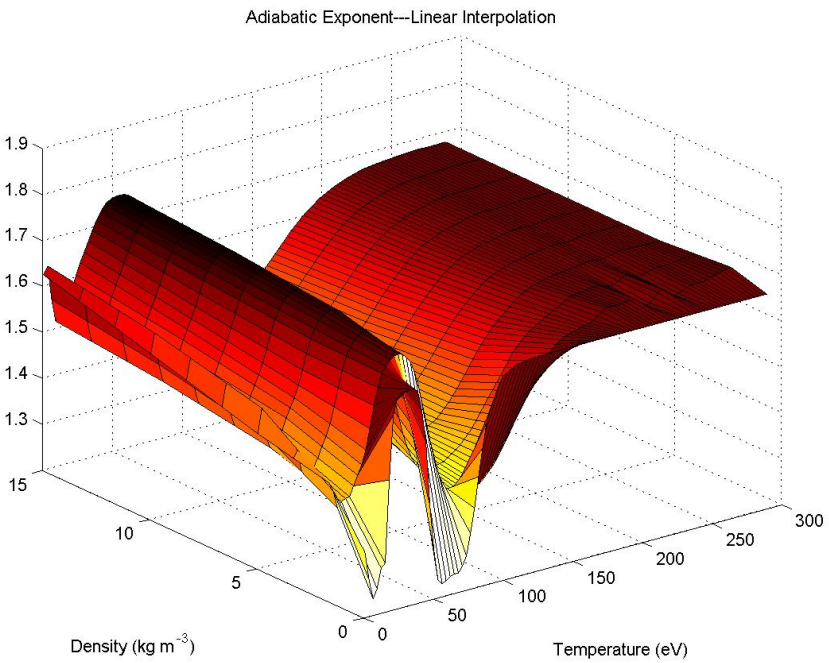

Figure A.4: Flibe adiabatic exponent as a function of density and temperature.

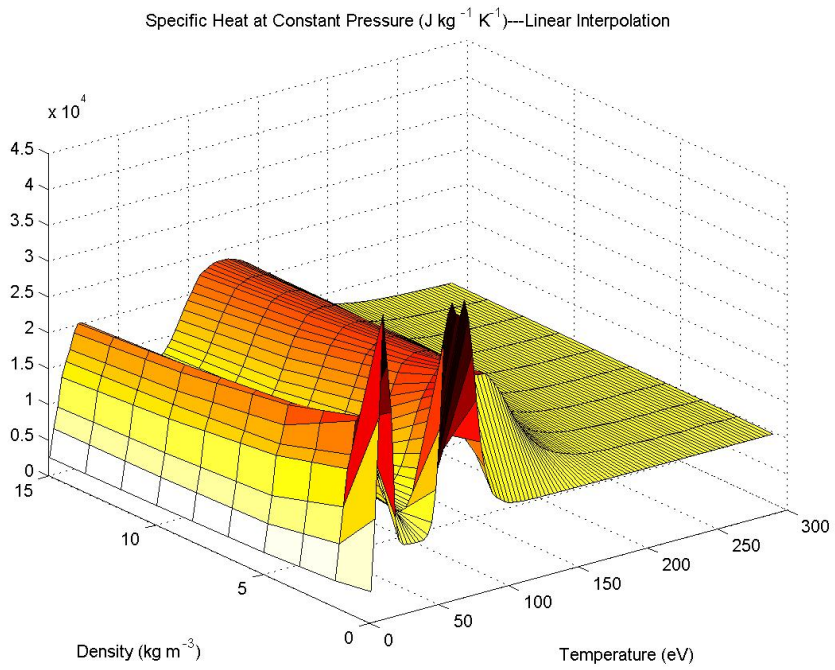

Figure A.5: Flibe specific heat at constant pressure as a function of density and temperature.

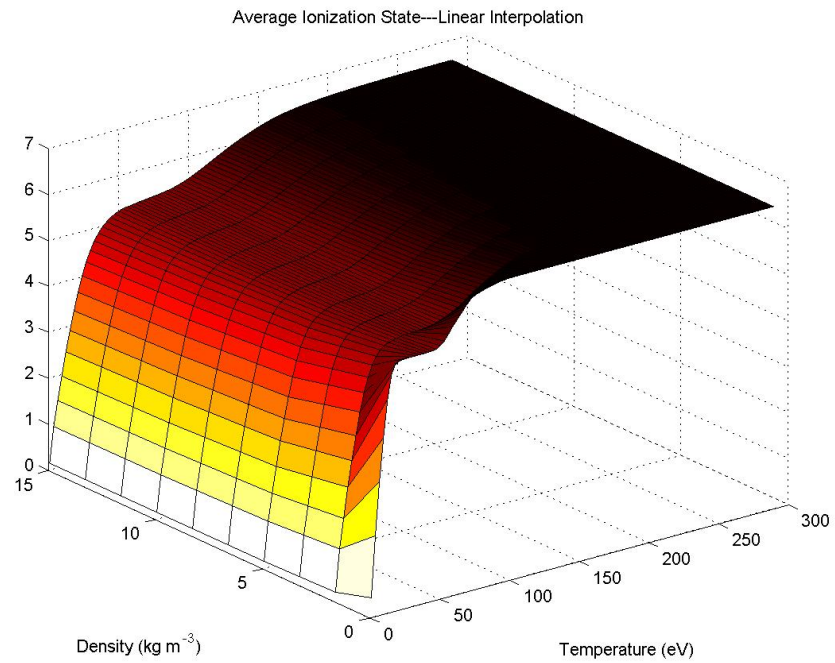

Figure A.6: Flibe ionization state as a function of density and temperature.

A.2.4 The Chen-Zaghloul Equations of State

Chen's equations of state restricted to the dissociation regime supplemented by Zaghloul's equations in the ionization regime ($T > 1$ eV) is referred to as the Chen-Zaghloul equations of state for flibe gas and is believed to constitute the most accurate flibe equations of state.

A.3 Opacities

A.3.1 Cold Opacities

Cold opacities were extracted from the EPDL97 library [22] through the Lawrence Livermore National Laboratory code EPICSHOW [21].

A.3.2 Hot Opacities

Hot opacities were obtained through the code TOPS [35], which was developed at Los Alamos National Laboratory.